



Tanja Grönlund

**DEVELOPMENT OF ADVANCED SILICON RADIATION
DETECTORS FOR HARSH RADIATION ENVIRONMENT**

Thesis for the degree of Doctor of Science (Technology) to be presented with due permission for public examination and criticism in the Auditorium 1382 at Lappeenranta University of Technology, Lappeenranta, Finland on the 9th of January, 2008, at noon.

Supervisor	Professor Tuure Tuuva Department of Electrical Engineering Lappeenranta University of Technology Finland
Reviewers	Professor Pekka Kuivalainen Electron Physics Laboratory Helsinki University of Technology Finland PhD Risto Punkkinen Department of Information Technology University of Turku Finland
Opponent	Professor Pekka Kuivalainen Electron Physics Laboratory Helsinki University of Technology Finland

ISBN 978-952-214-518-5
ISBN 978-952-214-519-2 (PDF)
ISSN 1456-4491

Lappeenrannan teknillinen yliopisto
Digipaino 2007

Abstract

Tanja Grönlund

Development of advanced silicon radiation detectors for harsh radiation environment

Lappeenranta 2007

80 p.

Acta Universitatis Lappeenrantaensis 297

Diss. Lappeenranta University of Technology

ISBN 978-952-214-518-5, ISBN 978-952-214-519-2 (PDF), ISSN 1456-4491

This thesis describes the development of advanced silicon radiation detectors and their characterization by simulations, used in the work for searching elementary particles in the European Organization for Nuclear Research, CERN. Silicon particle detectors will face extremely harsh radiation in the proposed upgrade of the Large Hadron Collider, the future high-energy physics experiment Super-LHC. The increase in the maximal fluence and the beam luminosity up to 10^{16} n_{eq} / cm² and 10^{35} cm⁻²s⁻¹ will require detectors with a dramatic improvement in radiation hardness, when such a fluence will be far beyond the operational limits of the present silicon detectors. The main goals of detector development concentrate on minimizing the radiation degradation. This study contributes mainly to the device engineering technology for developing more radiation hard particle detectors with better characteristics. Also the defect engineering technology is discussed.

In the nearest region of the beam in Super-LHC, the only detector choice is 3D detectors, or alternatively replacing other types of detectors every two years. The interest in the 3D silicon detectors is continuously growing because of their many advantages as compared to conventional planar detectors: the devices can be fully depleted at low bias voltages, the speed of the charge collection is high, and the collection distances are about one order of magnitude less than those of planar technology strip and pixel detectors with electrodes limited to the detector surface. Also the 3D detectors exhibit high radiation tolerance, and thus the ability of the silicon detectors to operate after irradiation is increased.

Two parameters, full depletion voltage and electric field distribution, is discussed in more detail in this study. The full depletion of the detector is important because the only depleted area in the detector is active for the particle tracking. Similarly, the high electric field in the detector makes the detector volume sensitive, while low-field areas are non-sensitive to particles. This study shows the simulation results of full depletion voltage and the electric field distribution for the various types of 3D detectors. First, the 3D detector with the n-type substrate and partial-penetrating p-type electrodes are researched. A detector of this type has a low electric field on the pixel side and it suffers from type inversion. Next, the substrate is changed to p-type and the detectors having electrodes with one doping type and the dual doping type are examined. The electric field profile in a dual-column 3D Si detector is more uniform than that in the single-type column 3D detector. The dual-column detectors are the best in radiation hardness because of their low depletion voltages and short drift distances.

Keywords: *high-energy physics, silicon radiation detector, 3D detector, TCAD simulation, characterization, electric field distribution*

UDC 539.1.074 : 546.28 : 621.382 : 539.1.076

Acknowledgements

The research work for this thesis was carried out at Lappeenranta University of Technology in the Laboratory of Microelectronics during the years 2003–2007. I would like to express my gratitude to my supervisor, Professor Tuure Tuuva who suggested this idea for a thesis and introduced an exciting world of the radiation detectors and high-energy physics. I thank the reviewers, Professor Pekka Kuivalainen and PhD Risto Punkkinen for a number of important comments and corrections, which significantly helped me to improve the thesis.

A great number of researchers were involved in this work. I would like to thank Helsinki Institute of Physics group, Dr. Jaakko Härkönen, Dr. Eija Tuominen, Dr. Panja Luukka and M.Sc. Esa Tuovinen for collaboration during these years. Especially, I would like to express my appreciation to Dr. Zheng Li from Brookhaven National Laboratory in New York, where I worked as a visitor researcher for two months in the spring 2007. His precious advices and the great experience from the field helped me in an invaluable way to finish this project. Also I would like thank Dr. Li's group members at BNL, Dr. Gabriella Carini and Dr. Wei Chen for helping me blend in the local life. I wish to thank Dr. Simo Eränen from VTT Technical Research Center of Finland for providing the samples of n-type 3D detectors.

I express my thanks to the microelectronics group at LUT. Dr. Kari Leinonen taught me the measurement techniques of the detectors. He was also the one who introduced the scanning electrode microscopy method to measure the electric field distribution inside the detector. At this point, I would also like to thank M.Sc. Jyri Roihuvuo from North Karelia Polytechnic for providing the facilities of the SEM.

M.Sc. Miia Koski was the bubbliest colleague I have ever had. No wonder, we were called “the giggling assistants”. I would like to thank her for help at the beginning of this project. I warmly thank M.Sc. Arja Korpela for sharing the challenges that were brought to us as employees of the microelectronics laboratory.

There are plenty of people to thank who have supported my work somehow. I would like to thank M.Sc. Antti Puisto for maintaining the simulation software. Many thanks belong to Ph.D. Hanna Niemelä for carefully reviewing the language of this manuscript. Especially I am grateful to our department's marvelous secretaries, Piipa Virkki and Tarja Sipiläinen, for helping me out to solve many practical problems and making the traveling around the world such a joy.

The financial support by the Research Foundation of Lappeenranta University of Technology (Lappeenrannan teknillisen yliopiston tukisäätiö), the Foundation of Technology (Tekniikan edistämissäätiö), the Finnish Cultural Foundation (Suomen Kulttuurirahasto), Walter Ahlström Foundation and Magnus Ehrnrooth Foundation is greatly appreciated.

For my family, I want to express my deepest thanks; I also owe my thanks to my friends, who have been spurred me along the way. I warmly wish to thank my husband Joonas for his support during this process.

Lappeenranta, December 2007

Tanja Grönlund

List of Publications

- Publication I* S. Eränen, T. Virolainen, I. Luusua, J. Kalliopuska, K. Kurvinen, M. Eräluoto, J. Härkönen, K. Leinonen, T. Palviainen and M. Koski, Silicon Semi 3D Radiation Detectors, *Nuclear Science Symposium Conference Record 2004, IEEE*, Volume 2, 16–22 Oct. 2004, pp. 1231–1235 (CD-ROM).
- Publication II* T. Palviainen, K. Leinonen, T. Tuuva, S. Eränen, J. Härkönen, P. Luukka, E. Tuovinen, Investigation of voltages and electric fields in silicon semi 3D radiation detectors using Silvaco / ATLAS simulation tool and a scanning electron microscope, *Nuclear Science Symposium Conference Record 2005, IEEE*, 23–29 Oct. 2005, pp. 1379–1382, ISBN 0-7803-9222-1 (CD-ROM).
- Publication III* K. Leinonen, T. Palviainen, T. Tuuva, E. Tuovinen, J. Härkönen and P. Luukka, Investigation of type inversion of n-bulk in 10 MeV proton-irradiated FZ silicon detectors using a scanning electron microscope, *Nuclear Instruments and Methods in Physics Research A* 552 (2005) 357–363.
- Publication IV* T. Palviainen, T. Tuuva, K. Leinonen, Minimizing guard ring dead space in the Si detector with n-guard ring at the edge of the detector, *Nuclear Instruments and Methods in Physics Research A* 573 (2007) 277–279.
- Publication V* T. Grönlund, Z. Li, G. Carini, M. Li, Full 3D simulations of BNL one-sided silicon 3D detectors and comparisons with other types of 3D detectors, *accepted for publication: Nuclear Instruments and Methods in Physics Research A* (2007), doi:10.1016/j.nima.2007.12.005.
- Publication VI* Z. Li, T. Grönlund, 3D Simulation Studies of Irradiated BNL One-Sided Dual-column 3D Silicon Detector up to $1E16 \text{ n}_{\text{eq}}/\text{cm}^2$, *will be submitted for publication: Nuclear Instruments and Methods in Physics Research A* (2008).

Author's Contribution

The research has been carried out at Lappeenranta University of Technology within the Department of Electrical Engineering, the Laboratory of Microelectronics group and in the framework of CERN RD50 collaboration during the years 2003–2007. A part of the research work was performed at the Brookhaven National Laboratory in the USA in the spring 2007, where the author worked as a visitor researcher. The author has participated actively in the modeling and the electrical characterization of radiation silicon detectors presented in this thesis. The publications in this thesis are a result of group effort. The author is the main writer in Publications II, IV and V and has contributed to the publications I, III, VI. The results have also been presented at international conferences. In this dissertation, these publications are referred to as *Publication I*, *Publication II*, *Publication III*, *Publication IV*, *Publication V* and *Publication VI*.

Summary of Publications

Publication I presents the proposed new structure, a silicon semi 3D detector, developed by VTT Technical Research Center of Finland. In this case, only the vertical p-type doping pillars are employed for the n-type substrate. The vertical depth of the doping profiles is left as a variable. The paper describes the fabrication and the first results on the behavior of the semi 3D silicon radiation detector structure. The semi 3D detectors are processed on both Float Zone (FZ) and Czochralski (Cz) material. The measured electrical characteristics include leakage current and capacitance-voltage measurement. These were measured by a CV-IV measurement setup. The results show that the semi 3D pixel structures have low leakage currents and low pixel capacitances. On the FZ silicon, the leakage current is smaller than on the Cz silicon and the breakdown occurs at higher voltages.

Publication II continues the work done for *Publication I*. In this paper, the simulation method and measurements using a scanning electron microscope are added to the study of the silicon semi 3D radiation detector structure in order to investigate the potential distribution inside the detector. There is a correspondence between the simulation results and SEM measurements, in other words, they show the same phenomenon: the semi 3D detector structure is fully depleted at low voltages, and with the high bias, the electric field is mainly formed between the end of the pillars and the backside.

In *Publication III*, the voltage measurement system with a scanning electron microscope was applied to 10 MeV proton irradiated Float Zone silicon radiation pad detectors. The results were compared with those acquired with other methods. The same semiconductor type inversion of n-bulk and a double-junction behavior were observed in this study with a better accuracy.

Publication IV describes the proposed $p^+/n/n^+$ pad detector structure with n^+ guard ring placed at the edge of the detector. In this structure, the guard ring has the same doping type as the substrate and the n^+ electrode at the bottom of the structure. Now, a full depletion region (active region) can be extended also sideways, when it is normally formed vertically from anode to cathode. This guard ring technique has evolved to minimize the dead space at the edge of the detectors and thereby to enhance the efficiency of the detector.

In *Publication V*, the simulation results of two single-sided 3D detector designs, one with single-type (n-type) columns and the other with dual-type columns (n- and p-type) on the p-type substrates are presented. The detectors are developed by Brookhaven National Laboratory (BNL). The full 3D simulations of different detector types show that it is possible to achieve similar electric field profile between a BNL dual-column 3D detector and other dual-column 3D detectors developed by other institutes with the benefit of the true one-sided process. In the case of the BNL single-type column detector, the simulations show that the high electric field is on the pixel side, which is the sensing area. Also the 3D simulations of weighting field profiles for different 3D detector structures were reported in this publication.

Publication VI presents the results of the 3D simulations that have been performed to study the effect of the irradiation on the dual-column 3D Si detectors. BNL dual-column 3D detectors have been simulated in detail with a variety of fluences. First, the full depletion voltage and then the electric field for a dual-column 3D detector are studied by simulations under the irradiations. Also it has been suggested that for future development, to achieve full depletion in a dual-column 3D detector at $1E16$ n_{eq}/cm^2 with a reasonable bias (≤ 200 V), the column spacing should be reduced.

Contents

Abstract	
Acknowledgements	
List of Publications	
Author's Contribution	
Summary of Publications	
Contents	
Symbols and Abbreviations	
1 Introduction	13
1.1 Scientific aspects of the semiconductor radiation-hard detectors	13
1.2 CERN RD50 collaboration	19
2 Radiation silicon detector properties	21
2.1 PN junction	21
2.2 Thermal equilibrium	22
2.3 Full depletion	24
2.4 Effective doping concentration N_{eff}	25
2.5 Radiation	29
2.6 Operation of a silicon radiation detector	31
2.7 Advantages of radiation silicon detectors	33
3 Characterization of advanced radiation detectors by simulations	34
3.1 Simulation program	34
3.2 Silicon 3D radiation detector	36
3.3 The operation of standard 3D detectors	37
3.4 Semi 3D detector structure on the n-type material	37
3.5 3D detectors for p-type material	42
3.6 Irradiated 3D detectors	53
3.7 Comparison of n- and p-type 3D detectors	56
3.8 Active edge of the detector	56
4 Discussion	59
5 Conclusions	62
Appendix A	64
Appendix B	71
References	76
Appended publications I-VI	

Symbols and Abbreviations

b	bottom quark
b	acceptor introduction rate
c	charm quark
c	donor removal coefficient
D_n	diffusion coefficient for electrons
D_p	diffusion coefficient for holes
d	down quark
d	thickness
d_{tr}	trapping distance
E, \mathbf{E}	electric field
$E(x)$	electric field distribution
E_0	weighting field
E_C	conduction band
E_c	activation energy on conduction band
E_F	Fermi level
E_{F0}^n	Fermi level on n-side
E_{F0}^p	Fermi level on p-side
E_i	intrinsic level
E_m	maximum electric field
E_V	valence band
E_v	activation energy on valence band
e^+	positron
e^-	electron
g_a	average introduction rate
G_n	electron generation rate
G_p	hole generation rate
G_{th}	thermal equilibrium generation rate
h^+	hole
I_{leak}	leakage current
i	current
J_n	electron current density
J_p	hole current density
k	Boltzmann constant, $1.38 \cdot 10^{-23}$ J / K
kT	thermal energy
L_p	column spacing
N_A	acceptor impurity density or short-term annealing component
N_B	acceptor or donor impurity density
N_C	stable damage part
N_D	donor impurity density
$N_{D,0}$	donor concentration before irradiation
N_{eff}	effective carrier / doping concentration
N_Y	reverse annealing component
n	neutron
n	n-type semiconductor material
n	electron concentration
n_0	equilibrium electron concentration
n_i	intrinsic carrier density, $1.45 \cdot 10^{10}$ cm ⁻³ (Si, 300K)
n^+	heavily doped n-type material
n^-	low-doped n-type material

P	pitch width
p	proton
p	p-type semiconductor material
p	hole concentration
p_0	equilibrium hole concentration
p^+	heavily doped p-type material
q	elementary charge, $1.6021 \cdot 10^{-19}$ As
R	recombination rate
R_n	electron recombination rate
R_p	hole recombination rate
R_{th}	thermal equilibrium recombination rate
s	strange quark
T	temperature
t	top quark
t	time
t	electrode length
U	excess recombination rate
U_{dep}	depletion voltage
V	potential, external voltage
V_{bi}	built-in potential
V_{dep}	depletion voltage
V_{fd}	full depletion voltage
V_{SEI}	voltage applied to a secondary electron detector of SEM
v	up quark
v_d	drift velocity
W	diode thickness
W_N	device depth
W	boson
x	x-direction
x_d	depletion region length
x_n	depletion region length on n-side
x_p	depletion region length on p-side
Z	boson

Greek letters

β	recombination factor
ϵ_0	permittivity of vacuum, $8.854 \cdot 10^{-12}$ F / m
ϵ_{Si}	permittivity of silicon, $11.7 \cdot \epsilon_0$
μ	muon
μ_n	electron mobility
μ_p	hole mobility
ν_e	electron-neutrino
ν_μ	muon-neutrino
ν_τ	tau-neutrino
π^\pm	pion
ρ	charge density
τ	tau (lepton)
τ	lifetime
τ_g	generation lifetime
τ_r	recombination lifetime

τ_{n}	recombination lifetime for n-type semiconductor
τ_{p}	recombination lifetime for p-type semiconductor
τ_{trap}	trapping time
$\Phi_{\text{eq}}, \phi, \phi_{\text{eq}}$	radiation fluence

Acronyms

AC	Alternating current
ADC	Analog to digital converter
ALICE	A Large Ion Collider Experiment
ATLAS	A Toroidal Lhc ApparatuS
BNL	Brookhaven National Laboratory
CCE	Charge collection efficiency
CERN	Centre Européen pour la Recherche Nucléaire European Organization for Nuclear Research
CMS	Compact Muon Solenoid
C_iO_i	Donor defect complex
CV	Capacitance (C) vs. Voltage (V)
Cz	Czochralski silicon
DA	Deep acceptor
DC	Direct current
DD	Deep donor
DOFZ	Diffusion Oxygenated Float Zone
DP	Double peak
FZ	Float Zone
IV	Current (I) vs. Voltage (V)
LCR	Inductance, capacitance, resistance
LEP	Large Electron Positron Collider
LHC	Large Hadron Collider
LHCb	B mesons experiment in LHC
LUT	Lappeenranta University of Technology
MCz	Magnetic Czochralski silicon
MIP	Minimum ionizing particle
OBIC	Optical beam induced current
PC	Personal computer
RD	Research and development
RF	Radio-frequency
SCSI	Space charge sign inversion
SEI	Secondary electron image
SEM	Scanning electron microscope
SLHC	Super Large Hadron Collider
SMU	Source measure unit
SPS	Super Proton Synchotron
STC	Single type of column
TCAD	Technology Computer Aided Design
TCT	Transient current technique
TOTEM	TOTAL cross-section and Elastic scattering Measurement experiment
V2	Di-vacancy defect
V3	Tri-vacancy complex defect
VO	Vacancy-oxygen
VTT	Technical Research Center of Finland

Chapter 1

Introduction

Silicon detectors have been chosen as central tracking detectors for the next generation of high-energy physics experiments such as the Large Hadron Collider (LHC) at CERN¹. For this purpose, silicon detectors, both pixel and strip, are the most precise electronic tracking detectors for charged particles. In high-energy physics experimental stations at the LHC, the silicon detectors are located as close as a couple of centimeters from the beam line, meaning operation in a very harsh radiation environment.

In the proposed upgrade of the LHC (Super-LHC, SLHC), the increase in the maximal fluence and the beam luminosity up to 10^{16} n_{eq}/cm² and 10^{35} cm⁻²s⁻¹ will require detectors with a dramatic improvement in radiation hardness. Therefore, the main goals of detector development for the SLHC concentrate on the technologies that minimize the radiation degradation. Several technologies have been extensively studied by CERN RD² collaborations during the last ten years:

- defect and material engineering (RD48, RD50)
- device engineering (RD50)
- operational mode engineering (RD39)
- applications of materials other than silicon (Si), such as diamond (RD42)

This work contributes to the first and the second topic. The goal of this work is to research and develop new detector structures such as 3D detectors and study the radiation damage effects inside the detector. The main emphasis is on the simulation methods, which can be used to simulate the processing and the electrical characteristics of the device. This work is part of the CERN RD50 research activity.

This dissertation is composed of the summarizing part and the appended original publications. The content of the summarizing part is organized in five chapters. In the following chapter, an overview of radiation silicon detector properties will be given. The basic radiation damage mechanisms and the radiation-induced defects in silicon bulk are reviewed. Chapter 3 describes the simulation methods of detectors and shows the results of characterization of various detector structures. Chapter 4 presents the discussion on the raised matters while completing this study. Finally, conclusions with suggestions for future research are given in Chapter 5.

1.1 Scientific aspects of the semiconductor radiation-hard detectors

In general, there are numerous fields of industry where radiation-hard detectors are used. Radiation-hard detectors are needed for example in medical, telecommunication, security and high-energy physics applications. This thesis concentrates on one detector type, semiconductor detectors. The main objective is the research of semiconductor detectors processed on the silicon (Si) and their use in a harsh radiation environment. The silicon detectors are particularly suitable for the detection of ionizing radiation such as protons, neutrons, pions and heavy ions.

In 1949, Louis de Broglie proposed setting up The European Organization for Nuclear Research (CERN). It was founded in 1954 in Geneva, Switzerland to research the basic structure of matter, particles. We know today that all matter in the Universe is built from nearly a hundred different types

¹ CERN - The European Organization for Nuclear Research, Geneva, Switzerland

² Research and Development

of atoms, each one made up of electrons with negative electric charge circulating a positively charged nucleus. The nucleus itself further consists of nucleons: positive protons and neutral neutrons. The electron seems to have no internal structure. Protons and neutrons are composite particles, each containing three quarks. Similarly as the electron, the quarks appear to have no structure. Only two types of quark, called "up" and "down", are needed to build the proton and neutron (Fig.1.1).

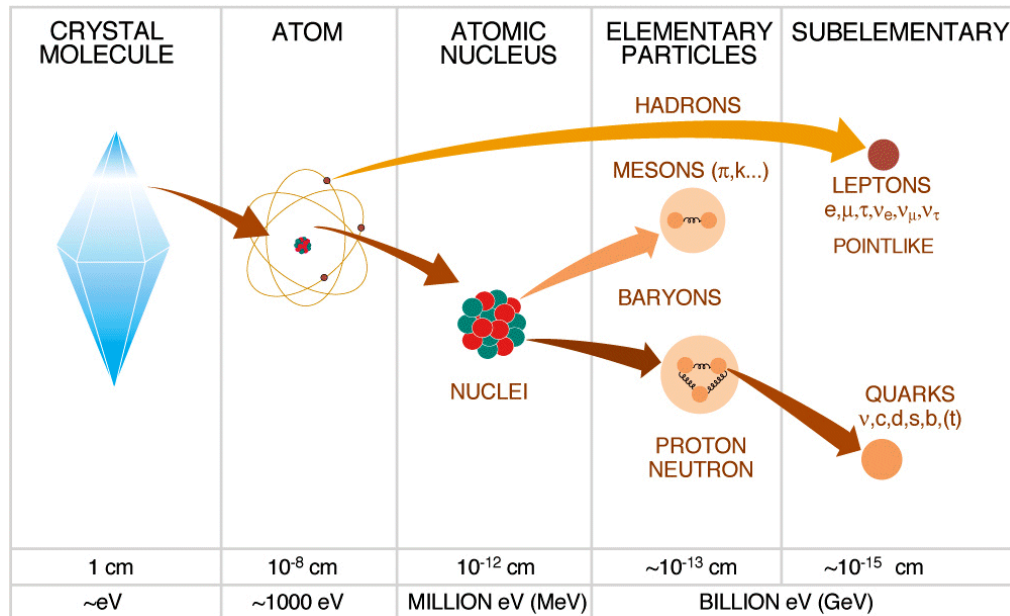


Figure 1.1: Structure of matter and its different scalings (CERN Document Server Copyright used with permission <http://cdsweb.cern.ch/record/841445>).

The generic names for particles in Figure 1.1 are often defined as follows (Coughlan 2006)

- nucleons: neutrons and protons
- hadrons: all particles affected by the strong nuclear force
- baryons: hadrons, which are fermions (half-integral spin particles) such as the nucleons
- mesons: hadrons, which are bosons (integral spin particles) such as the pion
- leptons: all particles not affected by the strong nuclear force, such as the electron and the muon.

In fact, there are less "ordinary" forms of matter that exist which we cannot see: cosmic matter coming from the space, high-energy collision matter and the "mirror image" of all of it, antimatter. To include them in the picture, we need a more general description and more particles. Based on the theories and discoveries in the physics research, the Standard Model of Particles and Forces has been created. The achievement is comparable to the unification of the electric and the magnetic forces into a single electromagnetic theory by J.C. Maxwell in the 19th century (CERN website – Particle Physics Today: The Standard Model).

Next, the theory behind the Standard Model of Particle Physics is described in brief. For further information, the reader is referred to textbooks (Coughlan 2006, Cottingham 2001). The Standard Model requires 12 matter particles and 4 force carrier particles to summarize all that we currently know about the most fundamental constituents of matter and their interactions. Figure 1.1 shows two matter particle "families" – the quarks and the leptons – both point-like and without internal structure. There are six quarks, which are usually grouped in three pairs based on their mass and charge properties: up/down (u and d), charm/strange (c and s), and top/bottom (t and b).

Further, there are six leptons, three with a charge and a mass – electron (e), muon (μ) and tau (τ) – and three neutral and with very little mass – electron-neutrino (ν_e), muon-neutrino (ν_μ) and tau-neutrino (ν_τ). Again, as their name openly implies, they are grouped to form three pairs (because of some distinctive behavior during the creation or decay processes). The (e^-/ν_e) and (up/down) have the lightest mass and are all that is needed to build up the stable matter and what is called the first generation of matter. However, high-energy processes produce a large variety of short-lived particles, which require the existence of "heavier" pairs, or heavier "generations" of matter. We have then (μ/ν_μ) and (charm/strange), which make up the second generation, while (τ/ν_τ) and (top/bottom) constitute the third generation. All second- and third-generation particles are unstable and quickly decay into stable first-generation particles; the second- and third-generation quarks can only be observed in high-energy physics experiments.

The standard model includes three types of forces acting among particles: strong, weak and electromagnetic. Gravity is not yet part of the framework. Forces are communicated between particles by the exchange of special "force-carrying particles" called bosons, which carry discrete amounts of energy from one particle to another. Each force has its own characteristic bosons: the gluon (strong force), the photon (electromagnetic force), the W and Z bosons (weak force).

Particles have a wide range of masses. Photons and gluons are completely massless, while the W and Z particles each weigh as much as 80 to 90 protons or as much as a reasonably sized nucleus. The most massive fundamental particle found so far, the top quark, is twice as heavy as the W and Z particles, and weighs about as much as a nucleus of gold. Why there is such a range of masses is one of the remaining questions of particle physics. Indeed, how particles get a mass at all is not yet properly understood (CERN website – Particle Physics Today: The Standard Model).

In the Standard Model, particles gain a mass through the Higgs mechanism (named after theorist Peter Higgs). According to this theory, both matter particles and force carriers interact with a new particle, the Higgs boson. It is the strength of this interaction that gives rise to what we call mass: the stronger the interaction, the greater the mass. Experiments have yet to show whether this theory is correct. The search for the Higgs boson has already begun at the LEP collider at CERN, and this work will continue with CERN's next machine, the Large Hadron Collider. In the LHC, very high-energy protons will collide against protons, and heavy ions such as the nuclei of lead will be smashed against heavy ions. The LHC experiment is used to find a proof of the existence of the Higgs boson (Fig. 1.2).

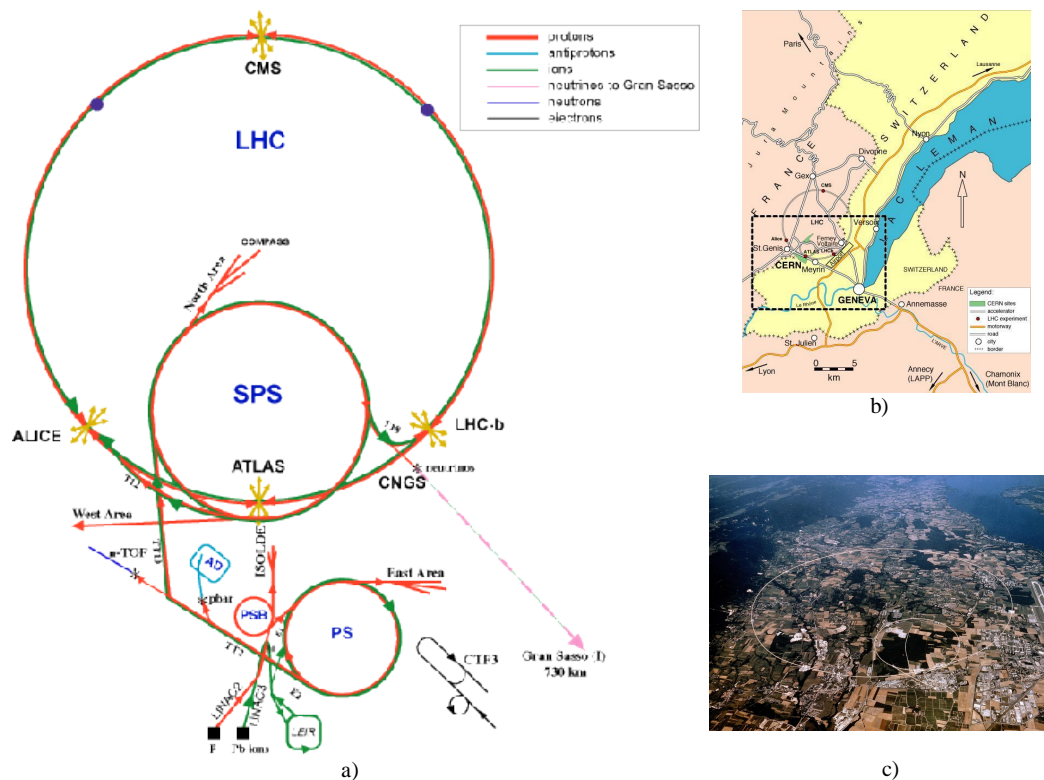


Figure 1.2: a) CERN accelerator complex. The LHC ring is 27 km long (CERN website). b) The map of the accelerator area (CERN – Web Communications Copyright used with permission). c) In the photo of the CERN site, the LHC and SPS rings are presented as visible structures, but actually the accelerator is placed under the ground (CERN website).

The LHC is a particle accelerator, which will collide beams of protons at an energy of 14 TeV. In the accelerator, the beam travels inside a chamber, which is a metal pipe, where air is permanently pumped out to make sure that the residual pressure is as low as possible. Inside the pipe, particles are accelerated by electric fields. Powerful amplifiers provide intense radio waves that are fed into resonating structures, the radio-frequency (RF) cavities. Each time the particles traverse an RF cavity, some of the energy of the radio wave is transferred to them and the particles are accelerated. To make a more effective use of the limited number of RF cavities, the particle beam can be forced to go through them many times, by curving its trajectory into a closed loop (CERN website – How does an accelerator work?).

Curving the beam's path is usually achieved by the magnetic field of dipole magnets. This is because the magnetic force exerted on charged particles is always perpendicular to their velocity. The higher the energy of a particle, the stronger is the field that is needed to bend it. In addition to just curving the beam, it is also necessary to focus it. Focusing the beam allows its width and height to be constrained so that it stays inside the vacuum chamber. This is achieved by quadrupole magnets, which act on the beam of charged particles. The maximum magnetic field is limited to some 2 Tesla for conventional magnets and some 10 Tesla for superconducting ones. This explains why the machines used in this kind of research are so large. The more powerful a machine is, the larger it needs to be. The whole accelerator system requires also several more objects such as: other magnets to perform "fine tuning" of the trajectory or the focusing, injection/ejection elements to put the beam into the accelerator or to take it out, measurement devices to give the operators information on the behavior of the beam, and of course, the safety elements (CERN website – How does an accelerator work?).

If we look, for example, the CMS experiment in more detail, we can see that the detector actually consists of many different pieces of equipment and detector types, each one able to recognize and measure a special set of particle properties such as charge, mass and energy.

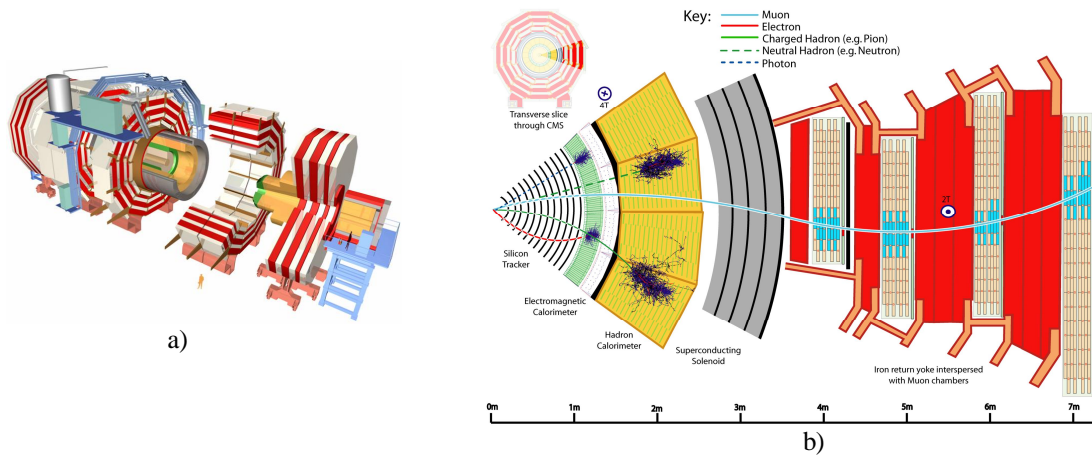


Figure 1.4: a) CMS experiment and b) particle interactions in detectors (CERN website).

Figure 1.4 shows that the CMS detector is divided into the silicon tracker, electromagnetic and hadron calorimeters, and muon chambers. The reason why detectors are divided into so many components is that each component tests for a special set of particle properties. These components are stacked so that all particles will go through the different layers sequentially. The tracking chambers make the path of the particle visible. It is not possible to see the particle itself, but the track of the particle can give a lot of useful information. A particle will not be evident until it either interacts with the detector in a measurable fashion, or decays into detectable particles.

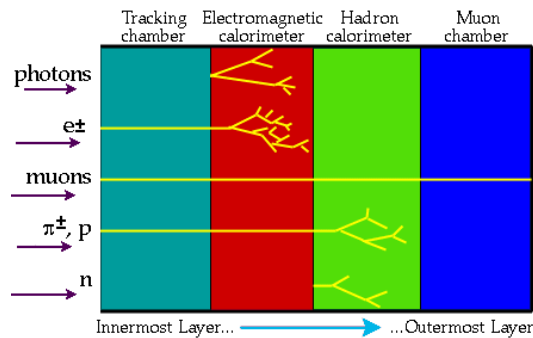


Figure 1.5: Interaction of various particles with the different components of a detector (http://atlas.ch/etours_exper/etours_exper07.html).

Charged particles, such as electrons (e^-), positrons (e^+), protons (p) and charged mesons (pions π^\pm) are detected both in the tracking chamber and the electromagnetic calorimeter, protons and pions also in the hadron calorimeter. Neutral particles, such as neutrons (n) and photons, are not detectable in the tracking chamber; they are only evident when they interact with the detector. Photons are detected by the electromagnetic calorimeter, while neutrons are evidenced by the energy they deposit in the hadron calorimeter. If a particle is only detected in the electromagnetic calorimeter, then it is fairly certainly a photon. Muons and neutrinos are often the only particles capable of escaping the calorimeter. Muons can hardly be stopped, but they leave a track and can be identified. Muon chambers are located outside

the calorimeter, and only muons can emerge and leave a track there. Neutrinos are not shown in Figure 1.5 because they rarely interact with matter, and can only be detected by missing matter and energy.

Silicon detectors are the major type of particle detectors in inner tracks of high-energy physics experiments. The objective of these semiconductor detectors is to make the particle track visible for other detector components. Silicon detectors can be used either in the pixel or the strip tracker. The sensors closest to the collision point are the pixel trackers. These devices consist of thin layers of silicon subdivided into tiny rectangular regions, pixels. Each time a charged particle traverses such a layer, a signal is produced that identifies which pixel has been traversed, and thereby gives a precise measure of the particle position. Indeed, this position is precise enough to determine whether the particle originated at the proton-proton collision point, or a few millimeters from it as a decay product of another particle. To provide additional position measurements somewhat further from the collision point, in the silicon strip tracker, layers of silicon subdivided into narrow strips are used to provide accurate information of the particle position. When a charged particle passes through the strip detector, signals identify which strip has been traversed. These strips provide precise 3-dimensional position measurement of particle trajectories. Strip detectors are used because the pixel detectors are too expensive for larger areas.

1.2 CERN RD50 collaboration

The CERN Research & Development RD50 collaboration “Development of Radiation Hard Semiconductor Devices for Very High Luminosity Colliders” has started in 2002 an R&D program for the development of detector technologies that will fulfill the requirements of the future high-energy physics colliders such as the possible upgrade of the LHC at CERN towards the Super-LHC. CERN RD50 collaboration offers an excellent forum to work with international partners. It consists of 51 institutes and 262 scientists (June 2007). Its objective is to support the activity in basic silicon research and to develop feasible detector solutions for the future high-energy physics experiments, where the irradiation field will be an order of magnitude higher than in the actual experiments. RD50 is a relatively large consortium, and therefore, it is organizationally divided into six research lines; the participating institutes concentrate on the research topics that best correspond to their expertise.

The main research objective of the RD50 collaboration is to develop radiation hard semiconductor detectors that can operate beyond the limits of present devices (R&D Prop. 2002). These devices should withstand fast hadron fluences as expected for example for a luminosity upgrade of the LHC. For the Super-LHC experiments, the luminosity is upgraded to $10^{35} \text{ cm}^{-2}\text{s}^{-1}$ and the innermost tracking detectors have to face fluencies above 10^{16} cm^{-2} of fast hadrons after five years operation accumulating an integrated luminosity of 2500 fb^{-1} (Fretwurst 2005). This is a ten times higher radiation level than expected for the tracking detectors of the LHC experiments. Under these conditions, detector performance may be limited by a large number of defects introduced into the device.

A luminosity upgrade is intended to improve the accuracy of the Standard Model and the new parameters, which are predicted to be discovered at the initial phase of the LHC experiments. Super-LHC experiment is predicted to run in 2017. Comparing the LHC environment to the assumed Super-LHC conditions, the intensity of the spectra increases one order of magnitude corresponding to the order of magnitude increase of luminosity. The beam energy is increased with a factor of two, and the average energy of the spectra is shifted to higher energy with 50 MeV (RD50 2004).

The presently available silicon detector technology cannot match the extreme requirements with respect to the necessary radiation tolerance. Several different research fields are under development and investigation to overcome problems of detectors caused by a super harsh radiation environment. Semiconductor sensors can be further developed for this purpose either by developing a more

radiation-tolerant detector material such as high-resistivity Czochralski (Cz) silicon both n- and p-type (material engineering) or investigating new device concepts such as 3D and edgeless detectors (device engineering). These advancements among others can set scene for radiation-tolerant cost-effective devices. Developing the suitable device for detecting the particles requires very cost-effective technologies and the optimum material, device structure and operational conditions for detectors.

At the fluencies up to 10^{15} cm^{-2} (outer layers of a Super-LHC detector), the change of the depletion voltage and the large area to be covered by the detectors are the major problems. At the fluencies of 10^{16} cm^{-2} (the innermost layer of a Super-LHC detector), the active thickness of any silicon material is significantly reduced because of trapping.

Table 1.1: Detector requirements for regions close to the beam in Super-LHC (Li 2007).

Region (cm)	25-50	15-25	7-15
Radiation level ($n_{\text{eq}} / \text{cm}^2$)	$10^{14} - 10^{15}$	$\sim 10^{15}$	$\sim 10^{16}$
Occupancy requirement	$80 \mu\text{m} \times 2 - 3 \text{ cm}$	$50 \mu\text{m} \times 400 \mu\text{m}$	$50 \mu\text{m} \times 300 \mu\text{m}$
Detector type	Strip	Pixel	Pixel
Radiation hardness requirement	Strip	Pixel	3D pixel or replacing every 2 years
Overall detector type	Strip	Pixel	3D pixel or replacing every 2 years

Table 1.1 lists the requirements for silicon detectors to be used in various regions in Super-LHC at or near room temperature. Due to the combined requirement of occupancy and radiation hardness, the only options for the most inner region (7–15 cm) seem to be the 3D pixel detectors or replacing the detectors every two years. For the outer regions, however, more detector choices can be made.

Chapter 2

Radiation silicon detector properties

In silicon detectors, the basic structure to make a particle track visible is based on a pn diode junction working under reverse bias. Next, the basic operation of the radiation silicon detector is described.

2.1 PN junction

In order to explain the operation of a pn diode junction, one may first imagine the opposite sides of the junction originally isolated (Fig. 2.1a). Then, these extrinsic semiconductors of an opposite doping type are brought together and a pn junction is formed. Actually, a single crystal of the semiconductor is doped with acceptors on one side and with donors on the other side. The structure is originally electrically neutral, that is, the number of holes is the same as the number of acceptor ions, and the number of free electrons is the same as the number of donor ions. Once the regions are brought into contact, the electrons originating from the donor atoms will diffuse into the p region and the holes from the acceptor atoms into the n region. An electron and a hole that meet at the junction will recombine, and thus they both will disappear. This will lead the acceptors and the donors in the neighborhood of the junction to lose their mobile electrons and holes. Since this region is depleted from mobile charges, it is called the depletion region (Fig. 2.1b).

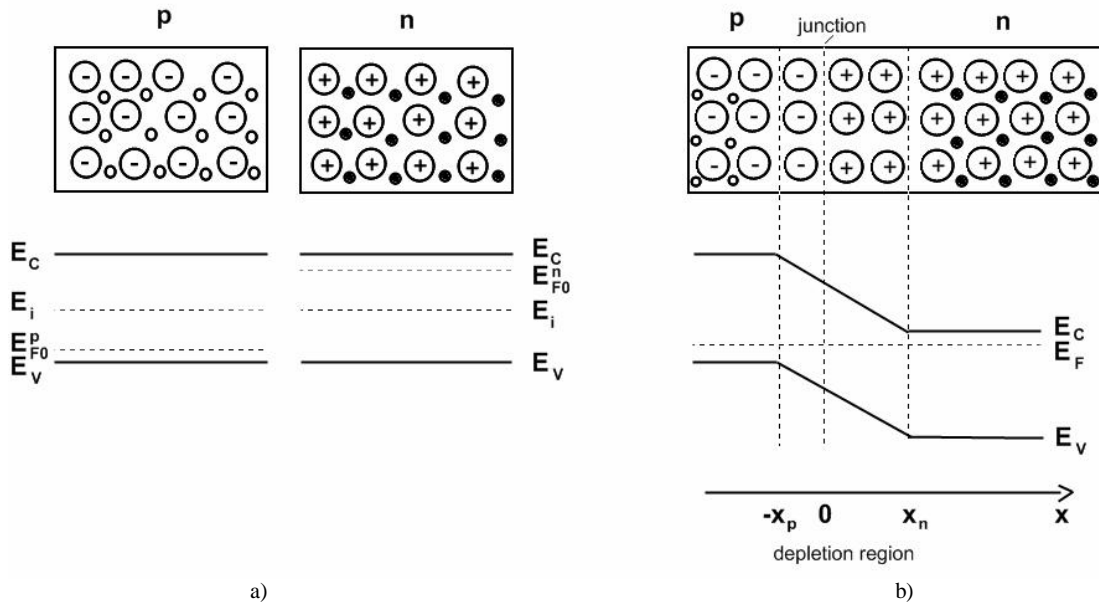


Figure 2.1: Schematic representation of a pn junction in thermal equilibrium a) with its parts separated and b) with its parts brought together. The negative acceptor ions are indicated by minus signs and the positive donor ions by plus signs. The free electrons are indicated by small filled circles and the holes by small unfilled circles. Fermi level E_F in the p-type region is shifted towards the valence band E_V and in the n-type region towards the conduction band E_C . When the regions are brought into contact, diffusion of electrons and holes results a static negative and positive electric charge in the p and n regions respectively. The conduction band energy and the valence band energy are continuous, and in thermal equilibrium the Fermi level is the same throughout the whole pn junction.

Considering this kind of an abrupt junction in thermal equilibrium conditions, where there is no applied voltage or current flow, a charge distribution is formed over the depletion region because of the uncovered fixed donor and acceptor ions. The depletion region is hence also called the space charge region. The thickness of the depletion region depends on the doping of the two sides of the junction. If both sides are heavily doped, then only a very thin depletion region needs to be uncovered to produce the necessary charges. If both sides are lightly doped, a significant depletion region needs to be uncovered to support the built-in potential. If one side of the junction is more lightly doped than the other one, the depletion region will extend further into the lightly doped side.

2.2 Thermal equilibrium

The electrically unneutralized ions in the neighborhood of the junction result in a space charge density ρ (Fig. 2.2a). The charge density is expressed by acceptor and donor concentrations. In thermal equilibrium, the total negative charge per unit area in the p-side must be equal to the total positive charge per unit area in the n-side

$$N_A x_p = N_D x_n \quad (2.1)$$

where N_A and N_D are the acceptor and donor impurity densities and x_p and x_n are the depletion region length on the p-side and n-side of the junction.

Because the n-side of the depletion region is positive and the p-side negative, there is an electric field across the depletion region (Fig. 2.2b). The electric field E is determined by the charge distribution through Poisson's equation

$$-\frac{\partial^2 V}{\partial x^2} = \frac{\partial E}{\partial x} = \frac{\rho}{\epsilon_{Si} \epsilon_0} \quad (2.2)$$

where V is the potential, E is the electric field, x is the x-direction, ρ is the charge density, ϵ_{Si} is the dielectric constant of silicon (11.7) and ϵ_0 is the permittivity of vacuum ($8.85 \cdot 10^{-14}$ F/cm).

Because of the electric field, a potential difference or a voltage is developed across the depletion region without any external voltage connected to the structure (Fig. 2.2c). This voltage across the depletion region is known as the built-in potential V_{bi} . It can be calculated from

$$V_{bi} = \frac{kT}{q} \ln \left(\frac{N_A N_D}{n_i^2} \right) \quad (2.3)$$

where N_A and N_D are the acceptor and donor impurity densities, n_i the intrinsic carrier density (for silicon $n_i = 1.45 \cdot 10^{10}$ cm⁻³ at 300 K), k is the Boltzmann constant ($1.38 \cdot 10^{-23}$ J/K), T is the temperature (together, kT is the thermal energy [eV]) and q is the charge ($1.60 \cdot 10^{-19}$ C).

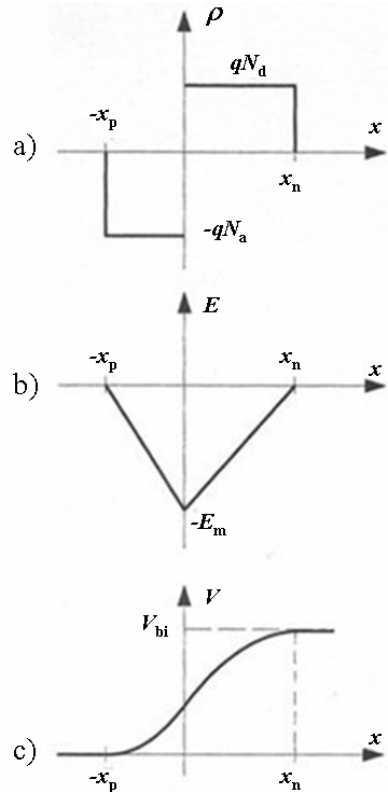


Figure 2.2: Abrupt pn junction in thermal equilibrium. a) Space-charge distribution. b) Electric field distribution. c) Potential variation (Sze 1981, Sinkkonen 1996).

The length in the x -direction of the depletion region can be calculated using Poisson's equation together with the value of the built-in potential. The built-in potential makes the pn junction reverse biased, which means that the depletion region exists. The total depletion region width is calculated from

$$x_d = x_p + x_n = \sqrt{\frac{2\epsilon_{si}\epsilon_0}{q} \left(\frac{N_A + N_D}{N_A N_D} \right) V_{bi}} \quad (2.4)$$

and the depletion region widths on the p- and n-sides are calculated from the total depletion region width

$$x_p = \frac{N_D}{N_A + N_D} x_d \quad (2.5)$$

$$x_n = \frac{N_A}{N_A + N_D} x_d. \quad (2.6)$$

2.3 Full depletion

The proper operation of silicon detectors is strongly limited by the requirement for the detectors to be fully depleted. The full depletion of the detector is necessary for a maximum detector signal and detector resolution. Only that part of the detector is active, which is fully depleted. In particle detector applications, an external reverse bias is added to this built-in potential causing the depletion region to become longer. Now, the total depletion region width is

$$x_d = \sqrt{\frac{2\epsilon_{Si}\epsilon_0}{q} \left(\frac{N_A + N_D}{N_A N_D} \right) (V_{bi} - V)} \quad (2.7)$$

where V is the external voltage applied. Equation 2.7 is for a two-sided abrupt junction; for a one-sided abrupt junction, the equation reduces to

$$x_d = \sqrt{\frac{2\epsilon_{Si}\epsilon_0}{qN_B} (V_{bi} - V)} \quad (2.8)$$

where $N_B = N_D$ or N_A depending on whether $N_A \gg N_D$ or vice versa.

It is easier to achieve full depletion for the non-irradiated detectors processed on high-resistivity silicon than it is for irradiated detectors. This is because the full depletion bias voltage changes with the irradiation fluence due to a change in the effective doping concentration N_{eff} . For a planar detector, the depletion voltage V_{fd} needed to fully deplete the detector varies with the doping concentration and the substrate thickness by (Sze 1981)

$$V_{fd} = \frac{|N_{eff}|d^2q}{2\epsilon_{Si}\epsilon_0} - V_{bi}. \quad (2.9)$$

The built-in voltage V_{bi} is often neglected since in most cases the depletion voltage is more than one order of magnitude higher. In Equation 2.9, d is the diode thickness.

For example, a diode made of the n-type material ($N_D = 10^{13} \text{ cm}^{-3}$), which has the p-contact on the upper surface of the detector, is fully depleted by applying a high enough negative potential to the p-contact (Fig. 2.3). The n-type back contact is connected to the ground (0 V potential).

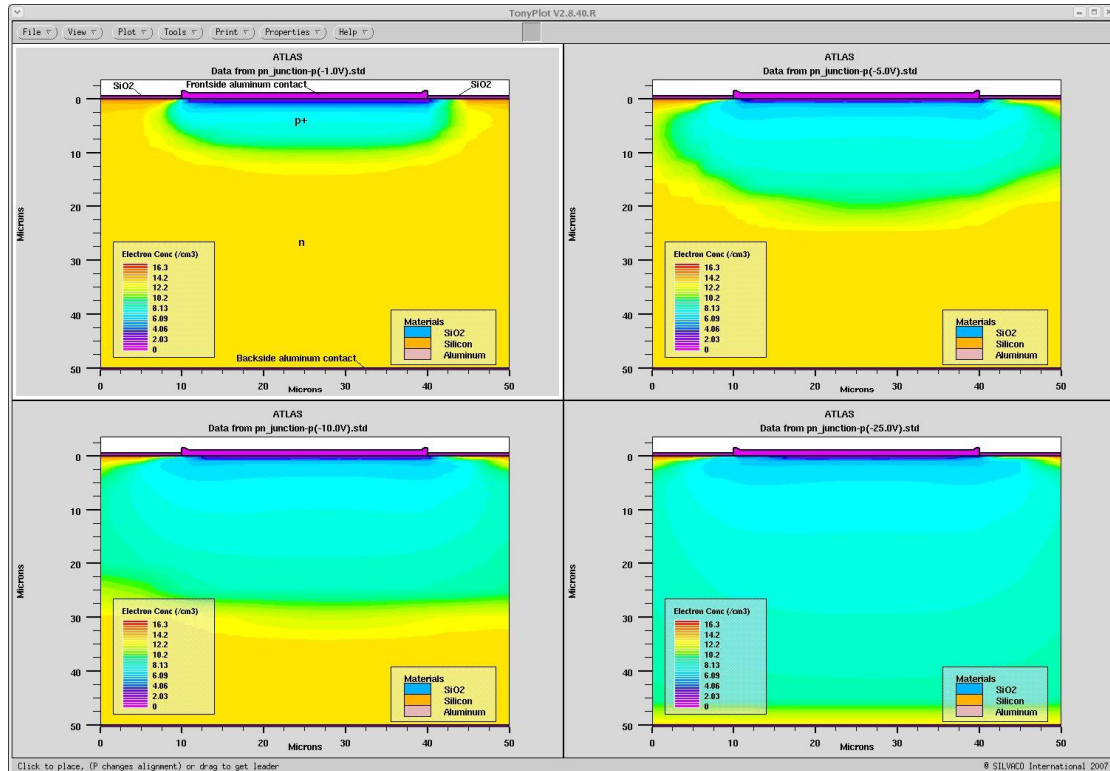


Figure 2.3: Spreading of the depletion region due to an external reverse bias. In the first quarter, the -1 V is applied; next, -5 V, -10 V and finally -25 V are applied. The last quarter shows that the structure is basically fully depleted. The electron concentration is presented in logarithm scale in legends. The source code of this simulation run is found in Appendix A.6.

In the simulations, the depleted area in the n-type bulk can be seen from the electron concentration, and in the p-type bulk from the hole concentration. The original doping concentration (10^{13} cm^{-3}) is indicated in Figure 2.3 with yellow color. The electron concentration values under the original concentration value are depleted (blue). The calculated full depletion voltage from Equation 2.9 for these impurities and for a 50 μm distance was -19 V. The simulated value (Fig. 2.3, the last quarter) is -25 V.

2.4 Effective doping concentration N_{eff}

As shown above in Equation 2.9, the depletion voltage is proportional to the absolute value of the effective doping concentration N_{eff} . An increase in the doping concentration leads to higher negative voltage values needed to deplete the valid distance. Because the reach of the full depletion is very crucial parameter in radiation detector applications, to ensure that the whole volume of the detector is active, the silicon is originally lightly doped (high resistivity). The detector material should have a high resistivity to facilitate the depletion of a deep volume with a reasonable voltage, and also because a shallow pn junction then has a higher breakdown voltage.

However, the irradiation causes an increase in the effective doping concentration. The change in the effective doping concentration is caused by the defects generated by radiation in the substrate. The depletion voltage as a function of absorbed fluence of silicon detectors is shown in Fig. 2.4.

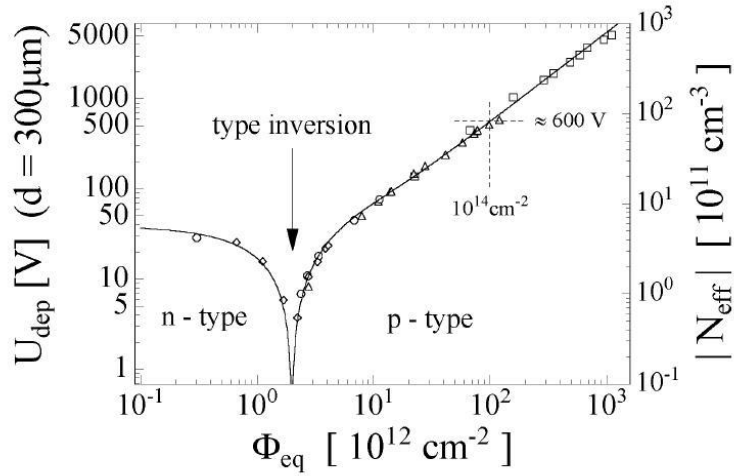


Figure 2.4: Change in the depletion voltage with respect to the absolute effective doping concentration measured right after the irradiation (Wunstorf 1992).

Type inversion. The effective doping concentration N_{eff} undergoes further changes at the end of the irradiation, because the defects in the bulk can also migrate and combine among themselves. The effect of negative fraction of N_{eff} that increases with the fluence is related to two factors: the first mechanism is the shallow donor removal and the second is the increase in deep acceptor generation (Eremin 2002a). The first period, which the devices experience and where N_{eff} is reduced, is called annealing. For the starting n-type material at lower fluences, the N_{eff} is reduced by a donor removal. Also acceptor-like states are generated leading finally to the inversion of the sign of the space charge from positive to negative. This leads to the inversion of the type of the material. In irradiation, by increasing the particle fluence, the initially positive substrate doping concentration decreases up to the type inversion of the semiconductor bulk and becomes negative. The negative N_{eff} means that the high-resistivity n-type bulk material inverts to p-type. For standard planar detectors with p-type electrodes on the n-type substrate, after high irradiation, the region with a high electric field moves towards the backplane of the detector, to the ohmic n^+ contact, and the device, which was originally $p^+ - n - n^+$ will turn to a $p^+ - p - n^+$ structure. After the type inversion, a further increase of N_{eff} is called reverse annealing, and it can cause a very high bias needed to fully deplete highly irradiated silicon detectors.

Publication III shows the capacitance-voltage (CV) and the scanning electron microscope measurement (SEM) results of proton-irradiated n-type FZ silicon detectors. Both measurement setups are presented in Appendix B. The n-bulk detector samples were irradiated with 10 MeV protons in the Accelerator Laboratory at the University of Jyväskylä. After the irradiations, the full depletion voltages V_{fd} and the effective doping concentrations N_{eff} were resolved by CV measurements at 10 kHz in parallel mode. The results are presented in Figure 2.5.

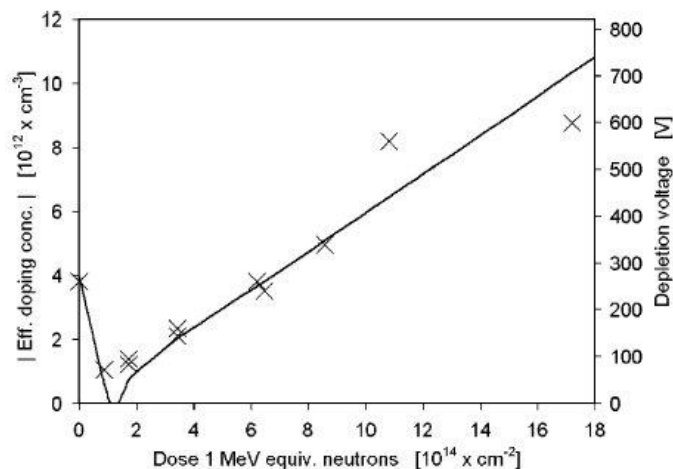


Figure 2.5: Evolution of N_{eff} in FZ-Si pad detectors irradiated with 10 MeV protons (Leinonen 2005a). Depletion voltage values have been normalized to 300 μm bulk thickness.

In Figure 2.5 we can see that increasing the amount of radiation fluence leads to the decreasing N_{eff} values towards the kink of the solid curve. It is assumed that at the kink the n-type bulk is fully compensated, and after the deep acceptor generation turns the bulk into p-type.

Double-peak electric field distribution. Defects generated by radiation in the substrate cause the variation of N_{eff} , which leads to two effects in silicon detectors: an increase in the full depletion voltage V_{fd} and the space charge sign inversion (SCSI). Due to the space charge sign inversion, heavily irradiated detectors stay on both sides sensitive to the short-range particles causing a double-peak (DP) effect in the electric field distribution (Eremin 2002b), which is also called a double-junction effect.

In the study in *Publication III*, three different n-type detectors were selected for further investigation of electric field distribution; one with no irradiation, the second one with a radiation fluence of $2.53 \times 10^{13} \text{ p/cm}^2$ and the third one with a radiation fluence of $1.50 \times 10^{14} \text{ p/cm}^2$. The latter two samples correspond to 1 MeV equivalent neutron fluence of 1.09×10^{14} and $6.45 \times 10^{14} \text{ cm}^{-2}$. These samples were cut and the cross-sections of the detectors were investigated with a SEM to study the electric field distribution inside the detector from the front surface to the back.

In the first detector, which has not been irradiated, it is expected to find a normal pn junction near the front surface and then near the p^+ pad of the detector. Figure 2.6 shows the SEM measurement results of the non-irradiated detector sample. The electric field distribution is shown along the detector thickness. The peak in the electric field and the place of the junction is found near the front surface of the detector as expected with all eight bias voltage values.

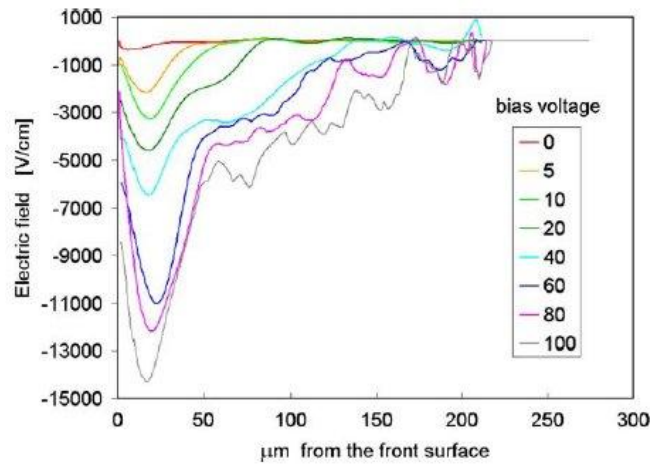


Figure 2.6: Electric field in the non-irradiated sample (Leinonen 2005a).

The second detector with intermediate fluence has the N_{eff} value close to the kink in Figure 2.5. With low bias voltages under 60 V, the electric field distribution behaves similarly as in the non-irradiated sample in Figure 2.6, whereas with higher bias voltages, another peak can be seen in the electric field distribution close to the backside of the detector in Figure 2.7. This indicates a pn junction at this depth.

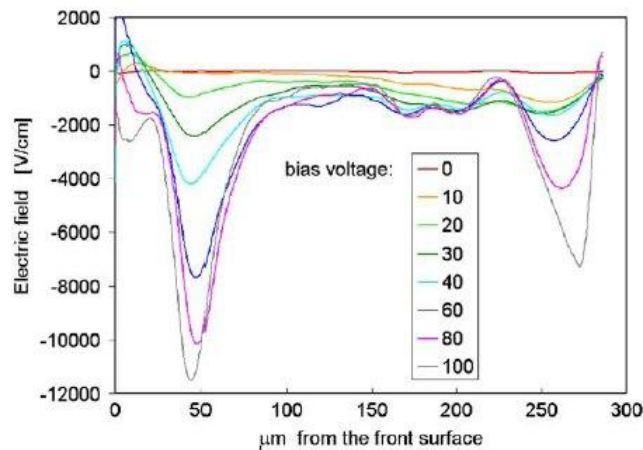


Figure 2.7: Electric field in the detector sample irradiated with 1 MeV neutron equivalent fluence of $1.09\text{E}14 \text{ cm}^{-2}$ (Leinonen 2005a).

The third detector with the highest fluence is supposed to have its pn junction near the n-type backside of the detector because the fluence is clearly above the kink of the solid curve in Figure 2.5. The n-type bulk is expected to be inverted to p-type, and the pn junction is expected to reside near the backside of the detector. Figure 2.8 shows that the largest electric field appears near the backside at a distance of 15–20 μm from the back surface indicating that the pn junction has moved to the backside of the detector, and the bulk has reversed its type from n to p.

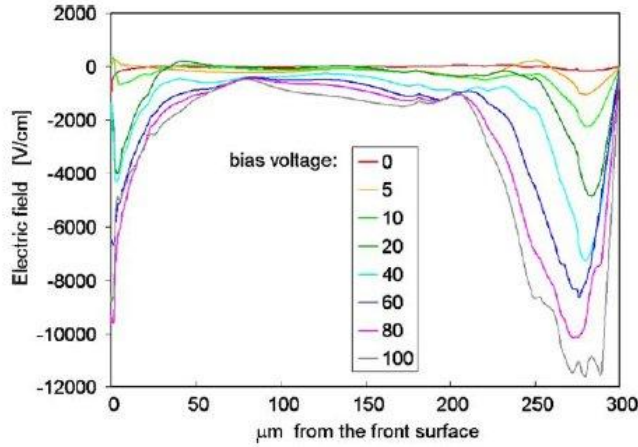


Figure 2.8: Electric field in the detector sample irradiated with 1 MeV neutron equivalent fluence of $6.45E14 \text{ cm}^{-2}$ (Leinonen 2005a).

However, there is a smaller peak of the electric field near the front surface in Figure 2.8. The field curves indicate that the bulk is not yet fully depleted at the highest measurement voltage 100 V and therefore there is also a pn junction near the front surface.

2.5 Radiation

The fluence dependence of the effective doping concentration assuming an absence of acceptor removal and donor creation is expressed as

$$N_{\text{eff}}(\phi) = N_{D,0}e^{-c\phi} - b\phi \quad (2.10)$$

where $N_{D,0}$ is the donor concentration before irradiation, c the donor removal coefficient and b the acceptor introduction rate.

The irradiation-induced change in the effective doping concentration ΔN_{eff} can be divided into three components, namely N_A , N_C and N_Y (Moll 1999). N_A is a short-term annealing component, whereas N_C does not depend on annealing and is therefore called the stable damage part, which consists of an incomplete donor removal; finally, N_Y is the reverse annealing component, as its behavior is opposite to the beneficial annealing.

After irradiation, for type-inverted detectors, the depletion voltage decreases (beneficial annealing), while for not-type-inverted detectors, the depletion voltage increases. In both cases, the N_{eff} is increasing, because for type-inverted detectors, N_{eff} is negative and becoming less negative, while for not-type-inverted detectors, N_{eff} is positive and becoming more positive. Usually, this behavior is attributed to the annealing of acceptors (Moll 1999). Because only the longest decay time constant is relevant to the operation of silicon detectors in high-energy physics experiments, the fluence dependence of N_A can be represented by

$$N_A = g_a \phi_{eq}. \quad (2.11)$$

The average introduction rate g_a is given by $g_a = (1.81 \pm 0.14) \times 10^{-2} \text{ cm}^{-1}$ (Moll 1999). The introduction rate for different types of silicon materials has been defined by measurements in Li (2004). There introduction rate for Czochralski and Float Zone silicon in neutron radiation is defined

as 0.017 and 0.022, respectively. Also for proton radiation, the introduction rate for Czochralski silicon is defined as 0.0045. This relation between the fluence and N_{eff} is used in the simulations presented later in this study. The value 0.02 for introduction rate has been used.

With radiation detectors, it is the radiation itself that is desired to be detected; its drawback is however that it may also cause damage to the detectors. Electrically active defects are responsible for changes in the main macroscopic properties of the particle detector.

The radiation-induced damage can be classified in two categories of bulk and surface defects. The most fundamental type of bulk radiation damage is a defect, produced by the displacement of an atom of the semiconductor material from its normal lattice. Defects are formed in the silicon lattice owing to the radiation damage, and several macroscopic effects occur including increase in the leakage current and the depletion voltage. The defects affect the detector properties such as carrier densities, mobility, generation lifetime, recombination lifetime and trapping probability. All defects will decrease the mobility. The generation and recombination lifetime will most strongly be reduced by the defects with energy levels close to the band gap center. For trapping, the capture and delayed release of charge carriers by the defects with medium-depth energy levels are dominant (Lutz 1999).

The radiation-generated defect complexes have complicated electrical properties: they act both as recombination-generation centers and as trapping centers, and they can also change the charge density in the space-charge region. The defect as a recombination-generation center is able to capture and emit electrons and holes, which leads to an increase in the reverse-bias current. In trapping centers, electrons and holes are captured and re-emitted with some time delay. This may lead to the reduction of the signal. When defects change the charge density, the increased bias voltage is needed to make the detector fully sensitive (fully depleted).

The vacancy left behind, together with the original atom at an interstitial position, constitutes a trapping site for normal charge carriers. The traps, which can be deep impurities, can capture a hole or an electron and keep it immobilized for a relatively long period of time. Two dominant trapping centers are the vacancy-oxygen (VO) and di-vacancy (V₂) defects (Da Via 2003a). Although the trapping center ultimately may release the carrier back to the band from which it came, the time delay is often sufficiently long to prevent that carrier from contributing to the measured pulse. After an irradiation up to 10^{16} cm⁻² fast hadrons, the trapping drastically reduces the effective drift length of charge carriers and, therefore, the produced signal does no longer depend linearly on the detector thickness or the electrode distance.

The radiation effects in silicon detectors are: first, the change in the effective doping concentration of the space charge region (N_{eff}) alters the operating voltage needed for full depletion; second, the fluence-proportional increase in the leakage current is caused by the creation of generation/recombination centers, and third, the deterioration of charge collection efficiency is due to the charge carrier trapping and incomplete depletion leading to a reduction of the effective drift length for both electrons and holes. These effects also influence the electronic noise (signal-to-noise ratio S/N), they increase the power dissipation and deteriorate the spatial resolution (R&D Prop. 2002). As a conclusion, the main effects of radiation damage on macroscopic silicon sensor properties are (Wunstorf 1997):

1. An increase in the leakage current I_{leak} ; can be reduced by cooling.
2. An increase in the effective doping concentration N_{eff} in depleted silicon; may lead to the type-inversion.
3. An increase in N_{eff} increases the bias voltage needed to achieve a given active thickness.
4. A decrease in the charge drift lifetime τ , which reduces the charge collection efficiency (CCE) from the depleted region.

The effects caused by N_{eff} can be moderated by using silicon growth techniques other than the commonly known Float Zone (FZ) and Czochralski (Cz) silicon methods such as oxygen-rich silicon substrates like Diffusion Oxygenated Float Zone (DOFZ) or magnetic Czochralski (MCz) method. The resistance to radiation can be improved with a high oxygen concentration in the silicon. In the FZ wafers, the originally low oxygen concentration can be moderated higher with the crystal growth or thermal diffusion from SiO_2 layers on polished wafers. With MCz method, the concentration and distribution of the oxygen can be better controlled than in the standard Cz method. Also the device engineering, together with material engineering, can lead to a better radiation hardness. The reduction of depletion voltage will increase the ability of silicon detectors to operate in the presence of a severe bulk radiation damage expected at high-intensity colliders. This is the case with the 3D detectors discussed later in this study. The voltage required to maintain a full depletion remains lower because of the shorter electrode distance.

2.6 Operation of a silicon radiation detector

Detecting particles is possible only when they interact with matter. In the case of silicon detectors, this happens when a charged particle travels through the silicon and generates electron-hole pairs, which are then separated by the electric field and drawn to opposite electrodes. The result of the radiation interaction in the semiconductor detectors is the appearance of a given amount of electric charge within the detector active volume. This charge must be collected to form a basic electrical signal. When a charged particle hits a semiconductor, an electron-hole pairs are created in the semiconductor. The collection of charge is accomplished through the imposition of an electric field within the detector, which causes the positive and negative charges (holes and electrons) created by the radiation to flow in opposite directions (Fig. 2.9). These are collected at the electrodes, which gives a measurable signal. The electrodes are DC or AC coupled to the readout electronics. In DC coupling, the signal readout electronics are connected directly to the electrodes. A problem in DC coupling is that also the leakage current is connected to the readout. In AC-coupled detectors, this is prevented by using a simple high-pass filter, where the resistor conduct the leakage current to the common bias line and the signal current is measured through the capacitor. Sometimes, the term *detector* is used to define the sensor and its readout electronics. From here onwards, the term refers to the sensor itself.

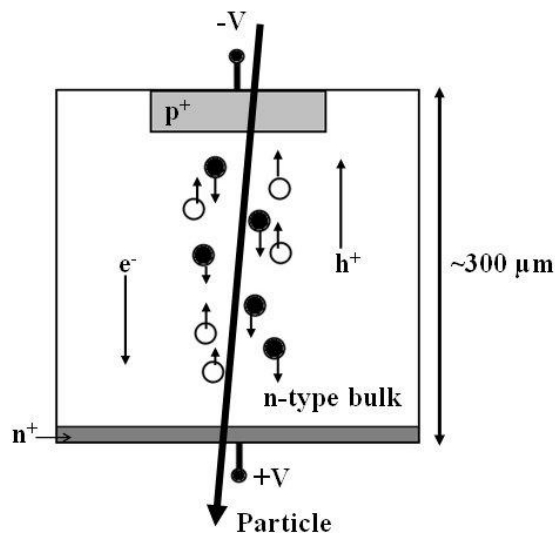


Figure 2.9: Schematic diagram of the operation of an n-type planar (2D) pad silicon detector. p^+ electrode at the top collects the positive charges (holes, which are indicated by small unfilled circles) and n^+ electrode at the bottom of the structure collects the negative charges (electrons, which are indicated by small filled circles).

The single-pad detector is a simple planar pn junction structure. The junction consists of a highly doped shallow p^+ region on a very low-doped n substrate and a backside of a highly doped shallow n^+ layer. The p^+ pad is directly connected to its metallic contact, aluminum on top of the pad, and to the readout electronics. Typical dimensions of the pad detector surface are $1 \times 1 \text{ cm}^2$ and the thickness is a few hundreds of micrometers.

The pad detector is not very suitable for tracking the precise particle position. For that purpose microstrip detectors were developed. In microstrip detector geometry, the planar p^+ implantation of a pad detector is subdivided into a number of independent narrow parallel strips. The strips widths are typically of the order of a few tens of micrometers. The pitch is defined as the distance between the center of two adjacent strips, which typically varies from a couple of tens micrometers to less than one hundred micrometers. For position sensing, each of these strips is connected to the signal readout electronics. However, the position sensitivity is only in one dimension in this kind of structure. For a second dimension, the n-strips perpendicular to the p-strips are added on the detector backside, thereby forming the double-sided microstrip detector structure. This is very effective on position resolution, because both electrons and holes are included in the signal; yet a drawback is very difficult processing. The fabrication of a large-area double-sided wafer is extremely challenging. That is the reason why planar silicon detectors are usually designed such that only one side is patterned.

Usually, the detector has a sensitive area and a cut edges feature one or more guard rings. In the case of traditional planar silicon detectors, the depleted (operational) region when reverse biased, must be kept away from the physical edge since the dangling bonds there and on the chips and cracks can short the electrodes (Kok 2006). Allowing extra dead space between the active electrode and the physical edge solves this problem but a portion of the detector volume is lost to be dedicated generally to protective structures, which control the stability of the working performance. Also the area at the detector edges must be allocated for guard ring electrodes that control the voltage drop and sinks the surface leakage current generated at the edge of the device. The methods of reducing the leakage current are an important consideration in the design of semiconductor detectors, because otherwise the leakage current obscures the small signal current and is a significant source of noise in many situations. The thermal generation of electrons and holes in the bulk gives rise to the leakage current. The leakage current decreases exponentially with inverse temperature and increases proportional to the number of active defects in the bulk. Some configurations use guard rings to help suppress surface leakage current. Guard rings minimize the surface leakage current by confining the electric field on the surface. The corner of RD50 pad detector with the protective guard ring structures surrounding the detector active area is shown in Figure 2.10 (RD50 2003).

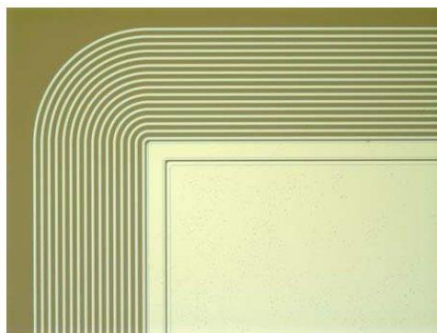


Figure 2.10: Top view of a corner of RD50 pad detector with multi-guard ring structure. Sixteen narrow $16 \mu\text{m}$ width guard rings and one $100 \mu\text{m}$ wide guard ring surrounds the active area of the detector. The distance between the active area implant and the first guard ring is $10 \mu\text{m}$ (RD50 2003).

A drawback of a standard planar silicon detector is the typical dead border surrounding the sensor's active area. This insensitive area is required because of the need for guard rings required to control the surface leakage current by keeping the electric field uniform and intercepting the current before the first signal electrode (Kok 2006). This dead area leaves behind important information. The dead space reduces the efficiency and the tracking accuracy of a detector. This is because the charge signal gets lower when the track is moved from the sensitive area towards the cut edge, becoming practically zero at the first guard ring. Minimizing the dead space or even totally edgeless detectors are discussed in the next chapter.

For a semiconductor diode detector, the collection time of charges is in the range of a few nanoseconds (Knoll 2000). These times reflect both the mobility of the charge carriers within the detector active volume and the average distance that must be traveled before arrival at the collection electrodes. When the bias voltage exceeds the full depletion voltage, the thicker sensor collects a larger signal, but the advantage of the additional active thickness is limited by charge trapping.

2.7 Advantages of radiation silicon detectors

Advantages of silicon detectors can be described by comparing them with the most widely used radiation detectors that are based on ionization in gas (Lutz 1999). The most common advantages are a compact size, relatively fast timing characteristics (due to the mobility of electrons and holes) and an effective thickness that can be varied to match the requirements of a certain application. The small band gap of the silicon (1.12 eV) leads to a large number of charges per energy loss unit to be detected, meaning excellent energy resolution. Furthermore, in silicon the average energy for creating an electron-hole pair is 3.6 eV, which is an order of magnitude smaller than the ionization energy of gases (approximately 30 eV). The high density of silicon compared with gas counters leads to a high efficiency and makes it possible to build thin detectors. One of the main advantages with semiconductor detectors compared with other types of detectors is the possibility of creating fixed space charges by doping. This allows creating different field configurations and detector structures with new properties. Also the integration of the detector and electronics into a single device is possible if they are built out of silicon. On the other hand, disadvantages of semiconductor detectors are their limitation to small sizes, sensitivity to radiation and expensive manufacturing. Further, the development of more radiation-hard silicon detectors is discussed.

Chapter 3

Characterization of advanced radiation detectors by simulations

Standard planar silicon detectors have been considered for high-energy physics applications, but they suffer from limitations of speed, sensitivity, linearity and large-area coverage at a limited cost. To solve these problems, a 3D detector structure has been developed. Using p-type material instead of n-type gives a benefit to avoid type inversion and makes detectors more radiation hard. To improve the efficiency of the detector, the active area of the detector has to be maximized. This can be achieved by designs known as active-edge detectors or edgeless detectors. In these structures, the non-sensitive area is minimized. These applications are studied in this chapter, and the characterization of more advanced radiation detector structures has been made using a semiconductor simulation program by Silvaco Data Systems Inc. With this Silvaco program, the device characterization can be made.

3.1 Simulation program

Computer simulations of detectors are important to find understanding on the device physics and to predict the detector performance in the actual applications such as in the collider physics experiments. The simulation results achieved with commercial software packages help understanding the limitation of irradiated silicon devices. At their best, the computer simulations can cover the whole process of radiation damage in semiconductor detectors. The primary interactions of the damaging particles with the semiconductor lattice, the formation of defects, the structural and electrical properties of these defects, the impact of these defects on the macroscopic detector properties, and finally, the macroscopic device in the presence of defects can be simulated. In this chapter, the main interest is in the impact of the defects on detector performance by investigating electrical properties of the detector. Device simulations on a variety of radiation detector structures are presented later in this chapter.

For TCAD simulations in this study, the software package ATLAS by Silvaco is used as a device simulation tool. ATLAS can be used on its own by defining the structure under the investigation or with the ATHENA process simulator. ATHENA predicts the physical structures that result from the processing steps. The resulting physical structures are used as an input by ATLAS, which then predicts the electrical characteristics associated with the specified bias conditions. The combination of ATHENA and ATLAS makes it possible to determine the impact of process parameters on device characteristics. Besides simulators, there are other interactive tools in Silvaco Virtual Wafer Fab framework needed for producing the simulation results: DeckBuild provides an interactive run-time environment, TonyPlot supplies data visualization capabilities and DevEdit is an interactive tool for structure and mesh specification and refinement. A brief description of the Silvaco and its parts is given in Appendix A.

ATLAS is a physically based device simulator, which predicts the electrical characteristics associated with specified physical structures and bias conditions by using the basic equations for semiconductor-device operation. These equations describe the static and dynamic behaviour of carriers in semiconductors under the influence of external fields that cause deviation from the thermal-equilibrium conditions. The basic equations can be classified in three groups: Maxwell's equations, current-density equations and continuity equations (Sze 1981).

In Atlas, first, the structure to be simulated has to be defined including a two- or three-dimensional grid consisting of a number of grid points. By applying a set of differential equations, derived from Maxwell's laws and consisting of Poisson's Equation 2.2, the continuity equation and the current-density equations to the defined grid, the electrical performance of a device can be modelled. The

continuity and the current-density equations describe the way that the electron and hole densities evolve as a result of transport processes, generation processes, and recombination processes.

Current-density equations. The electron current density J_n and the hole current density J_p consist of the drift component caused by the field and the diffusion component caused by the carrier concentration gradient. The current-density equations are the base for analyzing the current-voltage curves in the semiconductor.

$$\mathbf{J}_n = q\mu_n n\mathbf{E} + qD_n \nabla n \quad (3.1)$$

$$\mathbf{J}_p = q\mu_p p\mathbf{E} - qD_p \nabla p \quad (3.2)$$

where μ_n and μ_p are the electron and hole mobilities. The carrier diffusion constant D_n and D_p and the mobilities are related by the Einstein relationship $D = (kT/q)\mu$.

Continuity equations. In the above current-density equations, the charge generation and recombination has been treated separately from the charge transfer phenomena, that is drift and diffusion. The continuity equation states that the increase in the number of charge carriers per time of a given type in an arbitrary part of the semiconductor is given by the difference of generation and recombination in the volume and the inward flux through the surface.

$$\frac{\partial n}{\partial t} = \frac{1}{q} \nabla \cdot \mathbf{J}_n + G_n - R_n \quad (3.3)$$

$$\frac{\partial p}{\partial t} = -\frac{1}{q} \nabla \cdot \mathbf{J}_p + G_p - R_p \quad (3.4)$$

where G_n and G_p are the electron and hole generation rate and R_n and R_p the electron and hole recombination rate. Electron-hole pair generation occurs by emission of an electron and a hole in sequence, whereas recombination is an inverse process, in other words, an electron and a hole are captured in sequence.

A very important parameter of a detector material is the charge-carrier lifetime, and there needs to be a distinction between the recombination and generation lifetimes, τ_r and τ_g respectively. These terms describe the transient behavior from a nonequilibrium charge distribution obtained either by injection of additional carriers or by their removal. Knowing electron and hole capture cross-sections, emission probabilities and the initial value of the electron and hole densities, one can find the time development of the charge-carrier densities and thus their lifetime (Lutz 1999). In thermal equilibrium, the rates of capture and emission have to be equal, separately for both electrons and for holes. In the stationary nonequilibrium case, the net recombination rate can be calculated either for electrons or for holes by taking the difference between capture and emission rates. One expects the same answer for electrons and holes because the average occupation rate of the defects has to be constant. The excess recombination rate U is defined with the recombination rate R and the same rate in thermal equilibrium R_{th} (Lutz 1999).

$$U = R - R_{th} = \beta(np - n_i^2) \quad (3.5)$$

From this the carrier concentration dependent recombination factor β , the recombination lifetime and the generation lifetime can be derived. Lifetimes τ_r and τ_g are inversely proportional to the net rate U .

$$\tau_{r,n} = \frac{1}{\beta n_0} \quad (3.6)$$

$$\tau_{r,p} = \frac{1}{\beta p_0} \quad (3.7)$$

$$\tau_g = \frac{n_i}{G_{th}} = \frac{1}{\beta n_i} \quad (3.8)$$

In thermal equilibrium, the generation rate G_{th} equals the recombination rate R_{th} . The generation lifetime τ_g is closely related to the current generated in space-charge region of the detector.

The radiation fluence causes the increase in the leakage current resulting from the creation of generation/recombination centers. The leakage current associated with a reverse-biased semiconductor junction has three components: diffusion, thermal generation and surface leakage. For silicon detectors operated at room temperature (300 K) and below, the diffusion component is so small that it can be ignored. The surface leakage current depends strongly on the fabrication process and often a guard ring structure is used to reduce the surface leakage current. The main contribution to the leakage current in a good silicon detector should come from thermal generation in the depleted silicon volume. To minimize the leakage current, the generation lifetime must be maximized.

For modelling carrier generation-recombination, ATLAS includes several different physical models (ATLAS 2007). Shockley-Read-Hall recombination model (Shockley 1952, Hall 1952) is one to be used for phonon transitions. Phonon transitions occur in the presence of a trap or a defect within the forbidden gap of the semiconductor. After defining the grid, device and the necessary mathematical methods and models, finally, the bias conditions are defined.

3.2 Silicon 3D radiation detector

When the detector suffers high radiation damage, full depletion cannot be achieved anymore and charge trapping reduces the amount of collected charge drifting for longer distances. A novel type of solid-state radiation detectors using a three-dimensional array of electrodes of both doping types penetrating into the detector bulk were proposed by Parker et al. in the mid 90s (Parker 1997). These 3D silicon detectors were introduced to reduce the electrode distance and therefore, to increase the amount of charge collected after heavy irradiation, while keeping the same detector thickness. The benefit of the 3D detectors is their capability to control the depletion mechanism by acting on the design of the electrodes rather than via material engineering.

Because of the geometry of the 3D detectors, the distances between the electrodes are small, which results in a very low full depletion voltage and very short collection time compared with the conventional single-sided planar detector. Advantageous with the 3D detectors are the collection distances, which are about one order of magnitude less than those of planar technology strip and pixel detectors with electrodes limited to the detector surface. The 3D detector devices exhibit high radiation tolerance, because the needed full depletion bias is smaller than in planar detectors and the drift distance is also reduced resulting in a fast signal, thereby increasing the ability of the silicon detectors to operate after irradiation.

3.3 The operation of standard 3D detectors

The standard design of 3D detectors presents the columnar electrodes of both doping types arranged in an adjacent cell and penetrated through the silicon substrate. The charge collection distance is notably shorter in 3D detectors than it is in planar detectors because of the columnar electrodes and their placement distance.

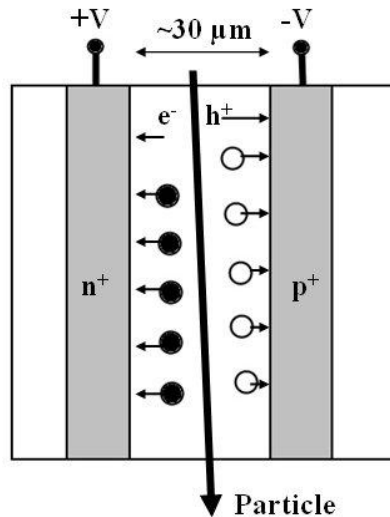


Figure 3.1: Schematic diagram of the operation of a standard 3D silicon detector. p^+ electrode collects the positive charges (holes, which are indicated by small unfilled circles) and n^+ electrode collects the negative charges (electrons, which are indicated by small filled circles).

The manufacturing process of the standard 3D detector is rather complicated because the columnar electrodes penetrate through the whole wafer. To make 3D detectors easier to process, a transitional form between the standard 3D and planar detector technology has been developed, called a semi 3D detector. Because of single-sided processing, the semi 3D detectors are easier to process than standard 3D detectors. In these designs, the columnar electrodes do not extend all the way through the wafer.

3.4 Semi 3D detector structure on the n-type material

Semi 3D or partially penetrating 3D electrode devices have been proposed (Li 2002) as a means to maximize signal response to incident radiation, to minimize sensitivity to defects arising from radiation damage and to reduce the V_{fd} value after irradiation. Silicon semi 3D detectors have vertical columnar electrodes, where the depth of the doping profiles is left as a variable. This makes the manufacturing process of the semi 3D detectors simpler than the manufacturing process of the standard 3D detectors because the column etching and the doping has to be performed only once (Fretwurst 2005). Semi 3D detector can have electrodes of both doping types, or just one, opposite to the bulk material.

Publication 1 presents the basic unit cell of the semi 3D detector shown in Figure 3.2. Semi 3D detectors are single-sided devices that have strips of one doping type on the front side while the backside has a uniform implant. In Figure 3.2 the unit cell has one p-type vertical columnar electrode on the n-type substrate. The depth of the p-type pillar depends on the diameter of the pillar. In addition to the p-type doping pillar, the front side of the detector has a p-type implantation around the pillar. There is also a square contact window in each pixel, the smallest unit cell of the detector. The pixels are connected as strips with the aluminium lines. The backside of the structure is a uniform

implantation similar to the planar detectors, and it is an n-type electrode. The semi 3D detector structure studied here is 300 μm thick.

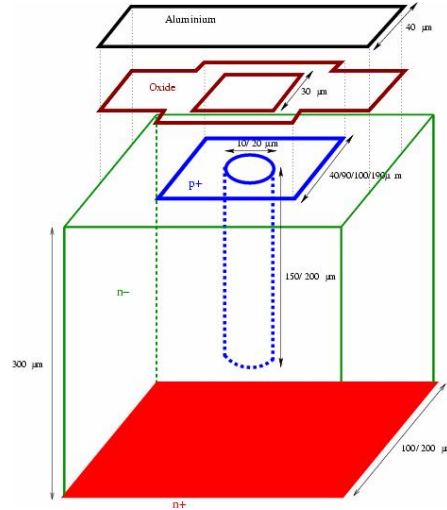


Figure 3.2: Unit cell of the semi 3D detector (Eränen 2004).

The full depletion of the detector volume has a high importance for the operation of the detector to be used in the high-energy physics experiments. To study the active area of the detector, the potential distribution inside the detector has to be investigated. In *Publication II*, the detector simulation results and also scanning electron microscope (SEM) measurement results have been presented. The SEM measurement setup is described in Appendix B.

First, the full depletion voltage of the semi 3D detector is studied by simulations. In the simulations, three p-type pillars penetrate 150 μm into the 300 μm deep detector bulk. The diameter of the p-type pillar is 10 μm . In addition to the p-type doping pillar, the front side of the detector has a p-type implantation around the pillar. For the 100 μm pitch, the width of this square implant is 90 μm , and from the edge of the pillar the width of which is then 40 μm towards the next pillar in the same contact line. P-type pillars constitute the anodes, and the cathode is placed on the backside of the detector as n^+ layer. The n-type substrate doping concentration was $1 \times 10^{12} \text{ cm}^{-3}$. The negative bias voltage is applied to the anode while the cathode remains at zero.

The simulations show that the semi 3D detector structure is fully depleted at low voltages. Figure 3.3 shows the electron concentration at 20 V bias.

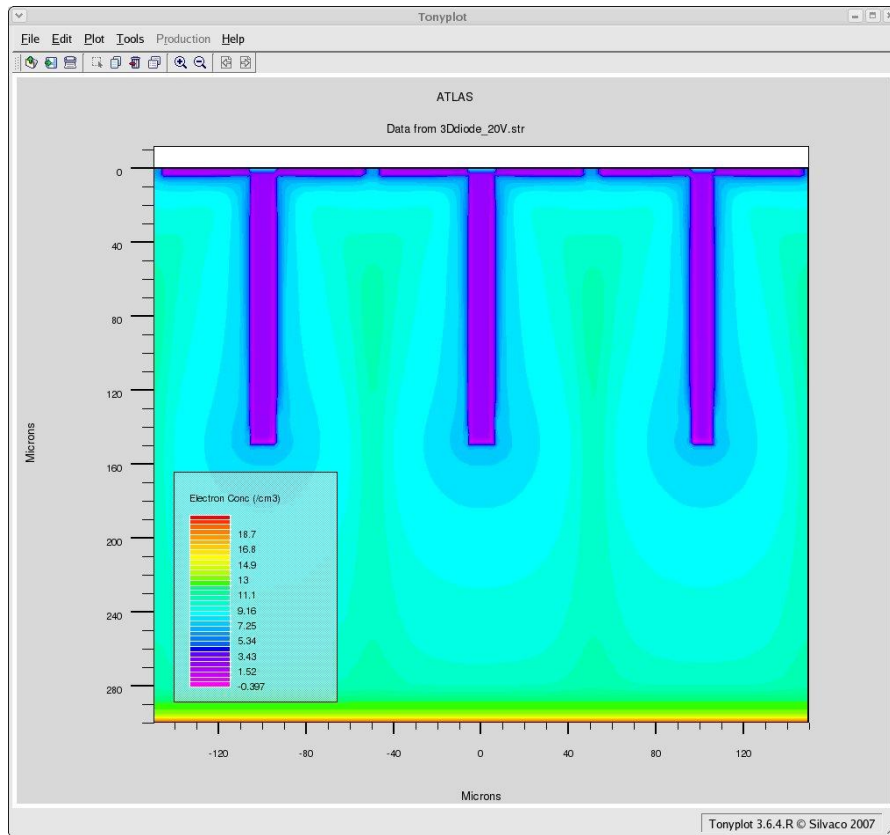


Figure 3.3: Electron concentration of the semi 3D detector structure at 20 V of bias. The original substrate doping concentration is $1 \times 10^{12} \text{ cm}^{-3}$ (light green color). Lower concentrations (light blue) are the depleted volume of the detector. It can be seen that at 20 V bias, the detector volume is already almost fully depleted. There are only shallow areas between the p-type pillars and at the bottom of the structure, which are not totally depleted.

The full depletion is not the only critical parameter for the proper operation of the detector. The detector volume should also have a high electric field. The low field area in the detector is non-sensitive to the particles and almost a dead space. Particles travelling through the low electric field area of the detector cannot be recognized. The potential and electric field distributions can be studied by simulations or SEM measurements. A benefit of SEM measurements is that they directly describe the potential distribution inside the detector.

The electric field can be modified higher by overdepleting the detector. That is the reason why simulations and SEM measurements were carried out with 0 V, 10 V, 40 V and 80 V bias voltages, where 40 V and 80 V bias are over the full depletion bias, which is approximately 20 V. Negative voltages were used because the p-type anodes were biased in the study.

The color scheme describes the potential distribution inside the detector structure. In the simulation figures, the color scheme is a rainbow spectrum divided into 30 colors, while the color scheme in the SEM measurements is a continuous rainbow spectrum. In the rainbow spectrum, the most positive voltage is presented as red and the most negative voltage is presented as bright magenta (voltage applied to the p-type anodes). There is a correspondence between the simulation results and the SEM measurements, in other words, they show the same phenomenon: with the high bias voltage the electric field is mainly formed between the end of the pillars and the backside. Because of the structure of the semi 3D detector, the charge-collecting field is only below the pillars where the electric field has formed. This can be seen from the potential figures with varied voltages of the silicon semi 3D

radiation detector structure (Fig. 3.4-3.7) generated in the simulations and the SEM measurements. The SEM photographs are taken from the cross-section of the split silicon semi 3D detector. The detector cross-section is in a slightly oblique angle compared with the array of the semi 3D detector. Therefore, four to five p-type pillars with varying lengths are shown in the photographs.

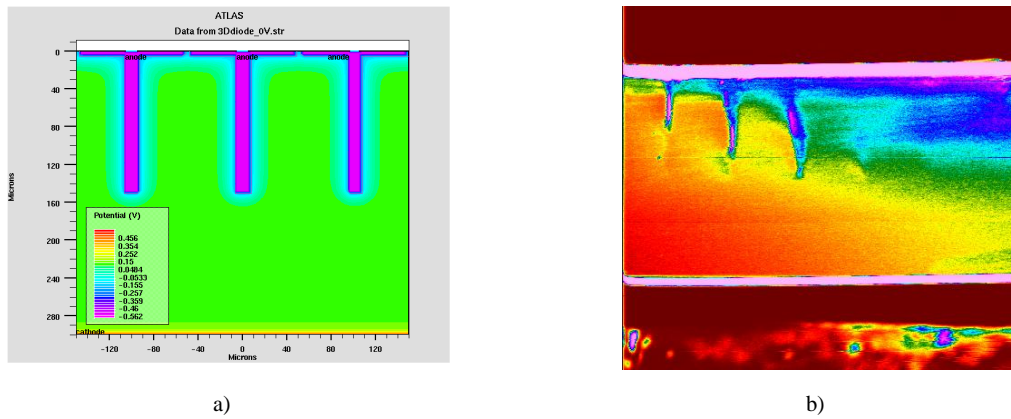


Figure 3.4: Potential distribution of the semi 3D detector structure at 0 V of bias a) simulation result and b) SEM measurement.

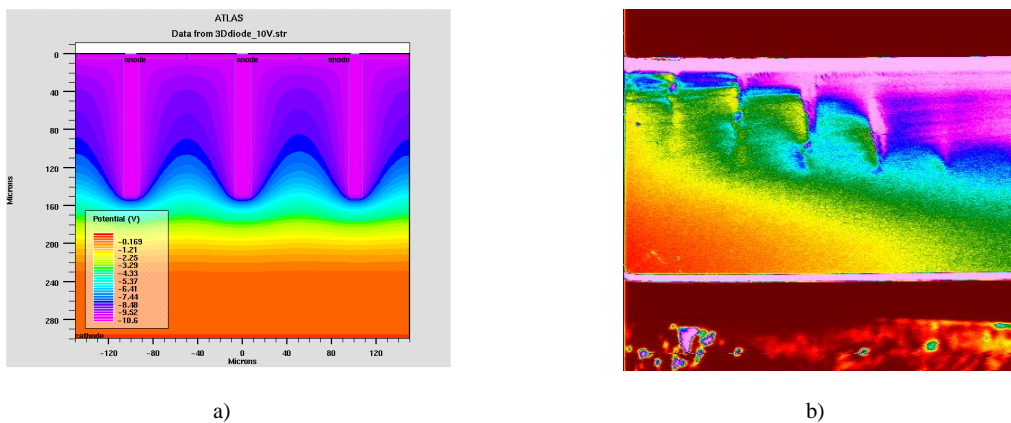
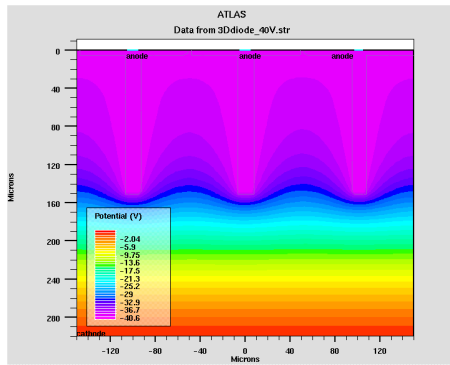
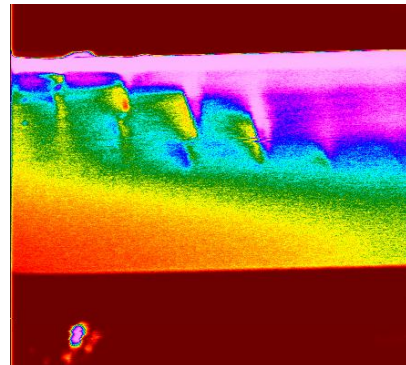


Figure 3.5: Potential distribution of the semi 3D detector structure at -10 V of bias a) simulation result and b) SEM measurement.

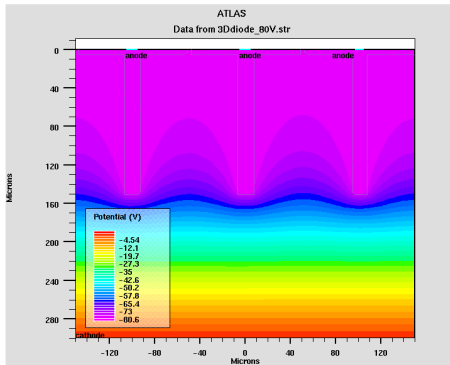


a)



b)

Figure 3.6: Potential distribution of the semi 3D detector structure at -40 V of bias a) simulation result and b) SEM measurement.



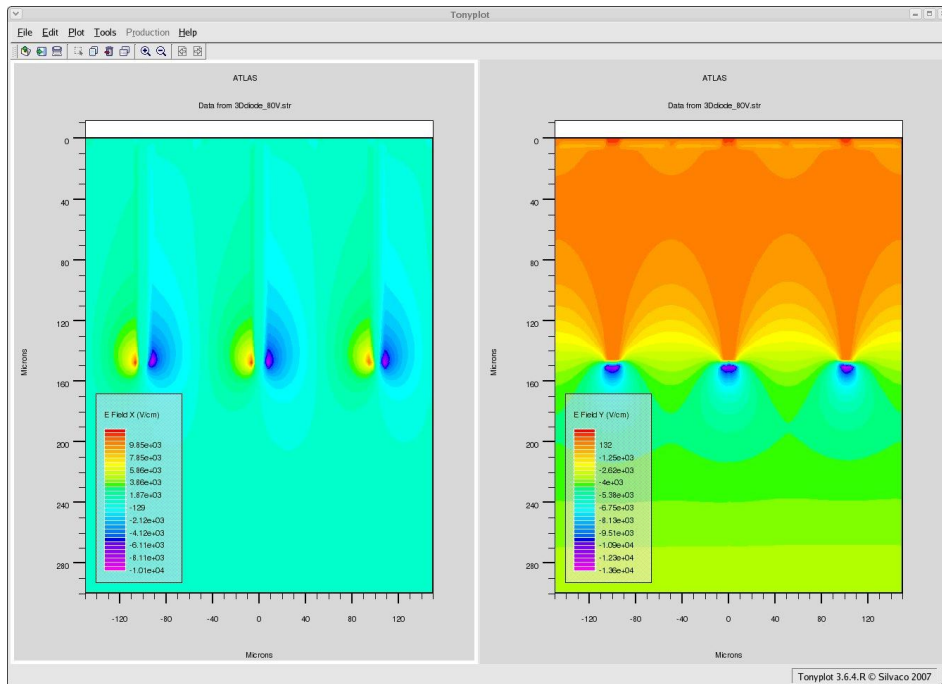


Figure 3.8: Simulated electric field of semi 3D detector structure at -80 V of bias a) electric field to the x-direction b) electric field to the y-direction.

There are also factors, which may cause differences between the simulation results and the SEM measurements. First of all, the simulation results are ideal and do not take into account the oxide charge or surface states, which affect the depleted region. However, the surface states do not have a significant influence when studying the depletion inside the detector bulk. Second, the SEM photographs differ from the simulation results because the relation between contrast and voltage is not linear. With small voltages below -20 V, the relation between contrast and voltage is close to linear, whereas with higher voltages, the change of the potential does not affect the change of the contrast linearly (Leinonen 2005b).

Drawbacks of this n-type semi 3D silicon radiation detector are its non-uniform electric field and the fact that it is formed on the backside of the detector. Moreover, it suffers from the type inversion of the bulk material. This can be reduced by changing the n-type substrate material to the p-type. The p-type material does not suffer from the type inversion, and the mobility of collected charges, now electrons, is higher than for the n-type material producing a larger signal.

3.5 3D detectors for p-type material

The most commonly used detector type is p-on-n, where the detector has an n-type bulk and a p-type structured front electrode. The bulk radiation damage results in a change in the doping concentration. A progressive irradiation of the initial n-type silicon leads to the inversion of its type of conductivity, turning into p-type silicon. The type inversion of a p-on-n detector poses a problem since the high electric field is switching from the structured readout side to the backside of the detector (RD50 2003). Further, if the detector is not operated with voltages well above the depletion voltage, the charge collection efficiency is reduced (Moll 2005).

The p-type silicon does not suffer from type inversion after irradiation. The n-on-p detectors do not type invert because their bulk is already of p-type, and the structured read-out side will be the one with the high electric field before and after irradiation. When the read-out side is in contact with a high electric field, the charge collection efficiency is improved because the n-side does not suffer from the space charge sign inversion (SCSI). Consequently, it presents higher charge collection efficiency (CCE) than p-on-n detectors beyond the SCSI point (Casse 2002). Moreover, n-on-p detectors collect electrons, which have three times higher mobility than that of holes, collected in p-on-n detectors. Therefore, the trapping of charge carriers is reduced (Bruzzi 2006). It is preferable to process n-type electrodes on the p-type substrate especially in the cases of close-to-beam applications, where highly non-uniform irradiation is present.

The n-on-p detectors are expected to be more radiation hard than standard p-on-n detectors. These detectors are more complex as they need an extra surface insulation. This insulation is achieved by a blank surface implant, named p-spray, or by p-type junctions, named p-stops. P-spray is a lightly doped layer over the wafer surface, and p-stops are heavily doped guard rings between the n-type guard rings in the case of a planar detector. In 3D detectors, p-stops can surround the n-type column electrodes at the front surface of the electrode.

In *Publication V*, the simulation results of two single-sided 3D detector designs, one with the single-type (n-type) of the columns (Fig. 3.9) and the other one with the dual-type of the columns (n- and p-type) (Fig. 3.10) on the p-type substrates are presented. Detectors were developed by Brookhaven National Laboratory (BNL) (Li 2007).

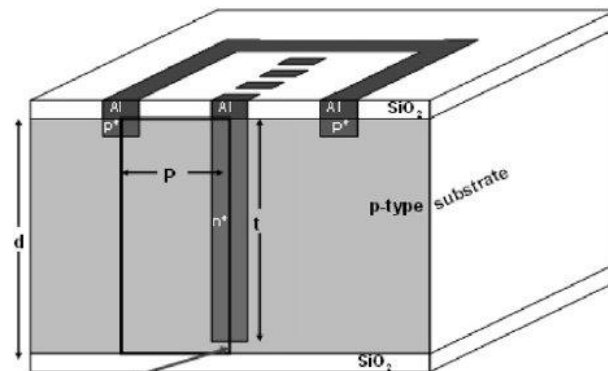


Figure 3.9: Schematic of the single-type of column (STC) 3D detector structure used in the device simulations. Device parameters in the simulations: $d = 300 \mu\text{m}$, $t = 270 \mu\text{m}$, $P = 60 \mu\text{m}$ (Li 2007).

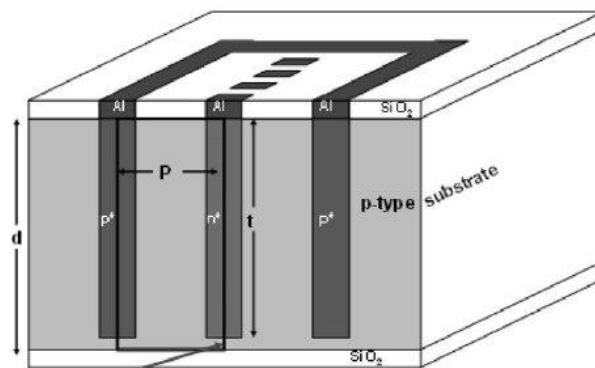


Figure 3.10: Schematic of the dual-type of column 3D detector structure used in the device simulations. Device parameters in the simulations: $d = 300 \mu\text{m}$, $t = 270 \mu\text{m}$, $P = 60 \mu\text{m}$ (Li 2007).

Single-type of column 3D detectors. A minimum cell of the BNL single-column detector used in simulations is shown in Figure 3.11. Here, the columnar electrodes are all of the same type, n-type, which are of the type opposite to the p-type substrate. They extend to 270 μm into the 300- μm -deep bulk. The ohmic contacts are achieved by placing two ion-implanted p-type electrodes on the front surface, in the other two corners in a simulation cell as shown in Fig. 3.11b. The backside is covered by a uniform silicon oxide layer and there is no implantation; thus the process is single-sided. The n⁺ column electrodes and p⁺ electrodes are covered with aluminum layers on the detector surface. The rest of the detector front side is covered with silicon oxide. The cell is simulated with two n-type columns on the opposite corners and two p-implants (0.5 μm deep) in the other corners. N-columns are surrounded by p-stops.

P-stops are used for surface insulation. The isolation is necessary since the positive charge in the SiO₂ induces the creation of an electron accumulation layer at the oxide-silicon interface. Otherwise, the interelectrode capacitance increases and shorts the electrodes together. The positive oxide charge increases with the irradiation, but it is present even in non-irradiated oxides and saturates when all traps are occupied by holes in the oxide layer.

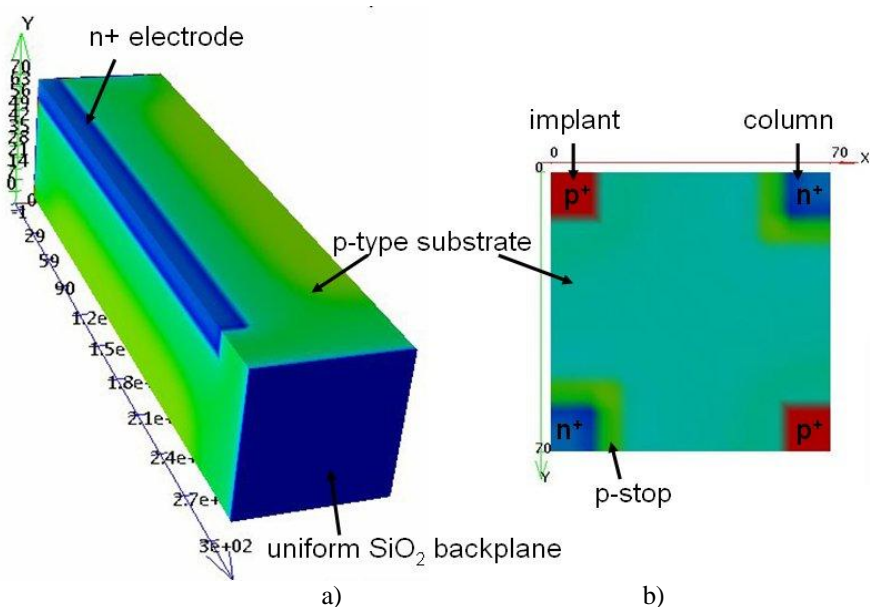


Figure 3.11: Simulated BNL 3D detector featuring columnar electrodes of one doping type, a) detector simulation cell and b) top view.

A sketch of the BNL dual-column detector used in the simulations is shown in Figure 3.12. In this structure, there are two n-type and two p-type doped columns on a p-type substrate. Same types of doped columns are placed to the opposite corners in the simulation cell. All the columns are placed on the front side of the detector, and they extend 270 μm into the 300- μm -thick p-type bulk. N-type columns are surrounded by p-stops. The backside is covered by a uniform silicon oxide layer and is never processed; hence, the process is again single-sided.

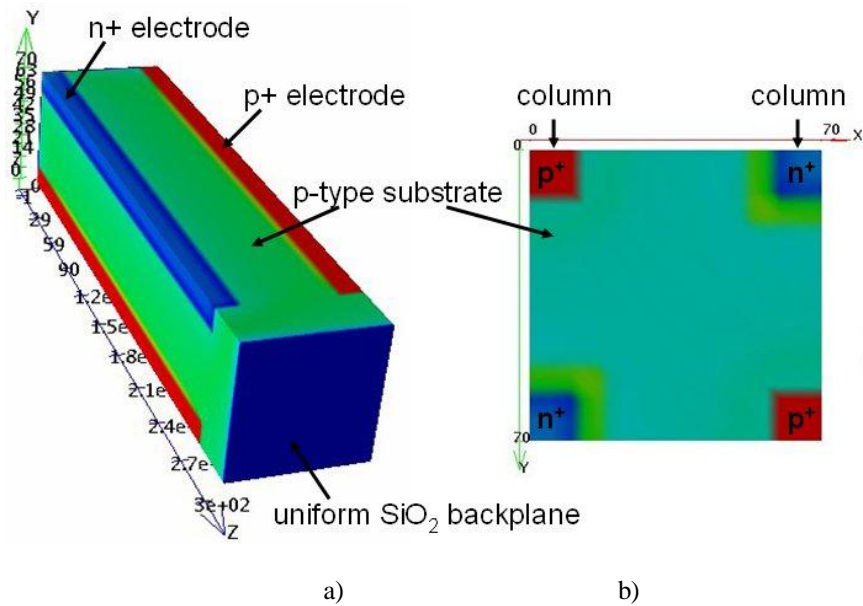


Figure 3.12: Simulated BNL 3D detector featuring columnar electrodes of n- and p- doping type, a) detector simulation cell and b) top view.

The full 3D simulations on 3D Si detectors were performed using the DEVICE3D package of ATLAS by Silvaco (ATLAS 2007). The aim of the numerical simulations was to investigate the electric field profiles in various 3D detectors. The strength of the electric field with the applied voltage, when the full depletion is reached, expresses the high- and low-field areas in the detector and its sensitivity to particles. The full 3D simulations of different detector types show that one can achieve a similar electric field profile between a BNL dual-column 3D detector and other dual-column 3D detectors developed by other institutes with the benefit of the true one-sided process. In the case of the BNL single-type column detector, the simulations show that the high electric field is on the pixel side. It is an advantage that the particle sensitive area is on the front side of the detector.

The sensitive region of a detector can be seen from the simulated electric field profile in the detector. BNL single-column detectors have the high electric field region on the pixel side (front side) of the detector and along the n-type columns, as shown in Figure 3.13 for single cell, similarly as in Figure 3.11. The bias voltage here is 100 volts on the n-type electrodes with respect to 0 volts on the p-type electrodes. It is clear that the electric field is highly non-uniform, and is the lowest in the volume directly under the p-type electrodes, which are only implants on the front surface.

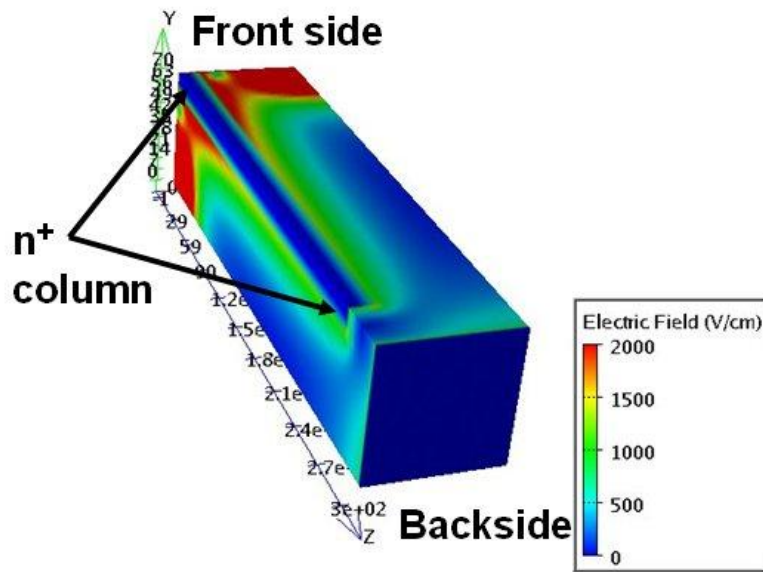


Figure 3.13: Simulated 3D electric field profile in a BNL single-type of column 3D detector at 100 V bias.

To see the electric field inside the detector in more detail, a 2D cut plane is plotted along the two n-type columns in Figure 3.14. We may observe that for the BNL single-type of column 3D detectors biased at 100 volts 1) the front side (or pixel side) is with the highest field, and it extends about 30 μm into the detector; 2) there is a high field along the n^+ columns all the way through the detector with a volume of about 2/5 of that between the n^+ columns; 3) the medium field between the n^+ columns also occupies about 2/5 of the volume; 4) the lowest field is near the middle of the two n^+ columns, which occupies about 1/5 of the volume; and 5) there are some medium to low fields in the volume under the n^+ columns, which also make this volume with some sensitivity to particles – it may not be entirely dead. Point 5) also raises the possibility that the volumes directly under the n^+ columns may serve as a way to recover some sensitivities from the supposed dead volumes of the n^+ columns themselves.

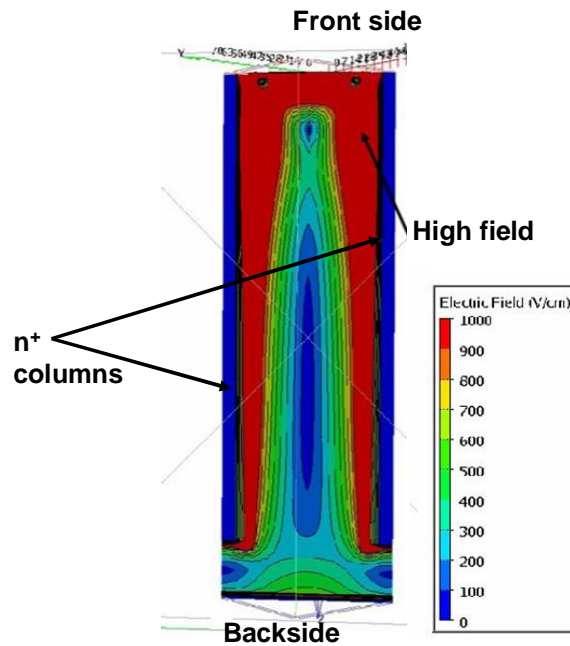


Figure 3.14: 2D cut plane of the simulated electric field in a BNL single-type of column 3D detector at 100 V bias.

It is interesting to note here that the simulated full depletion voltage for the BNL single-type of column 3D detectors is far smaller (5-10 volts) than that of planar detectors (80 volts) with the same thickness and resistivity. In this aspect, this type of 3D Si detector may be more radiation tolerant than the 2D planar Si detectors, especially after modest fluence ($>1 \times 10^{14}$ n_{eq}/cm^2) when the N_{eff} becomes higher and the electric field becomes better. This latter point was first systematically simulated at Trento for their single doping type column 3D Si detector (Piemonte 2005), where detectors built on a lower initial resistivity material have shown better electric field profiles. However, a voltage higher than the full depletion voltage should be used to obtain a high field near the back of the detector. Also, the longest drift length for a particle-generated free carrier (holes here) is still the whole detector thickness that can be notably larger than the column spacing, one may lose the contribution to CCE of one type of carrier (holes here) at very high radiation fluences ($>2 \times 10^{15}$ n_{eq}/cm^2).

To see the bias voltage effect on this type of 3D detectors, we plot a 2D cut plane for the same detector as shown in Figures 3.13 and 3.14; this time the bias is increased to 200 volts (Fig. 3.15). As we can see, the main change here is in point 1) listed above: the high field region near the front surface is extended to about 80 μm into the detector bulk as compared to 30 μm in the case of 100 volts. Points 2–5 are almost the same as those for the 100 volts case.

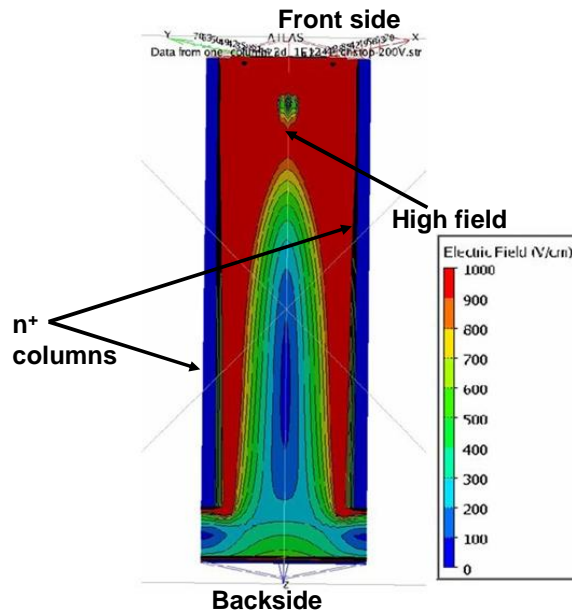


Figure 3.15: 2D cut plane of the simulated electric field in a BNL single-type of column 3D detector at 200 V bias.

It is interesting to compare the field profiles between the BNL single-column 3D detector and the Trento one proposed early by ITC-irst in Trento (Piemonte 2005, Fleta 2007). In a Trento single-type of column 3D detector, n-type columns are placed in every corner in one unit cell (Fig. 3.16), that is, n^+ columns in places where p^+ implants are located (Fig. 3.11) for the BNL single-type of column 3D detector. The p^+ ohmic contact is a uniform p^+ ion implant on the backside.

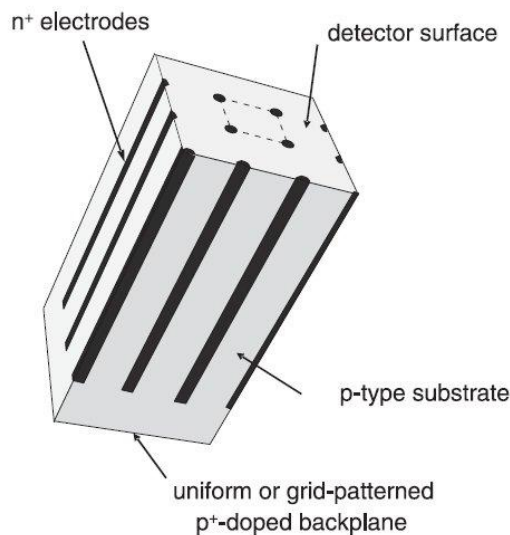


Figure 3.16: Sketch of a 3D detector featuring columnar electrodes of one doping type proposed by ITC-irst (Piemonte 2005).

Figure 3.17 shows the 2D electric field profiles of the two types of single type of column (STC) 3D detectors at 100 volts along a cut plane between the two n^+ columns. Field profile differences are clearly shown: 1) instead of a high field on the pixel side (BNL), the high field in a Trento detector is near the backside; 2) instead of some high field developed along the n^+ columns all through the

column length (BNL), half of the n^+ columns length near the pixel side has a low field in a Trento detector; and 3) in fact, most of the volume under the pixel (about 40% of the detector volume) has a low field in a Trento detector. The BNL single-type of column 3D detector provides better field distribution, and may therefore give better charge collection performance.

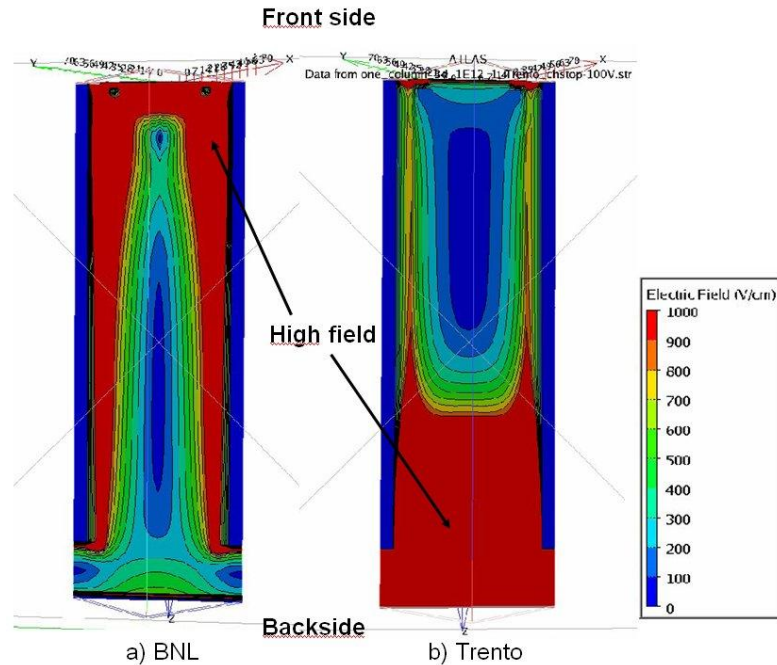


Figure 3.17: Comparison of electric field profiles between two types of single-column 3D detectors operated at 100 V bias. The 2D cut plane is along the two n^+ columns.

Dual-column 3D detectors. The 3D electric field profile of a BNL dual-column 3D detector operated at 40 volts is shown in Figure 3.18. It is clear that a high field is distributed all along the n^+ and p^+ columns, and throughout the detector. Again, similar to the BNL single-column 3D detector, there is a field developed under the columns near the backside, which could provide an extra sensitive region for the detector. The electric field profile in a dual-column 3D Si detector is more uniform than that in a single-type column 3D Si detector: the non-uniformity is minimum along the detector thickness, especially 20–30 μm away from either surfaces. The dual-column 3D Si detector is easier to deplete at lower bias voltages than the single-column 3D detector.

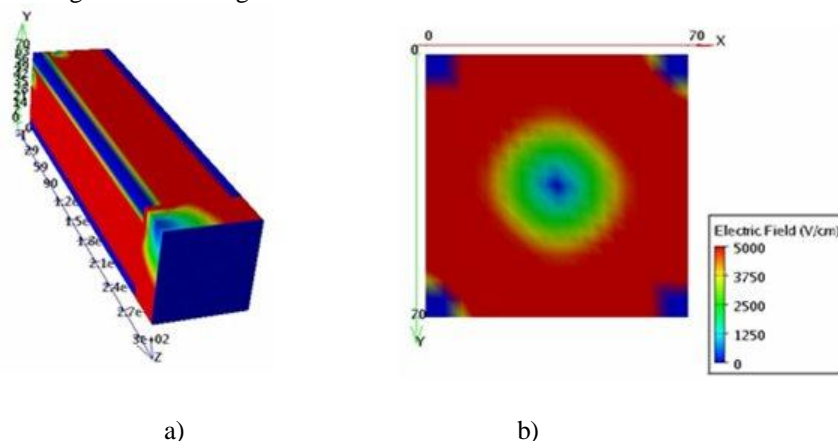


Figure 3.18: Electric field profiles of a BNL dual-column 3D detector operated at 40 V bias: a) 3D profile; b) 2D profile in a cut plane in the middle.

However, the field profile is still highly non-uniform as shown in a 2D cut plane in the middle of the detector at half of the detector thickness, $150\ \mu\text{m}$. The low field is near the center between the four electrode columns in a simulation cell, and the field is zero right at the center point (saddle point). This low-field region is common for all dual-column 3D detectors as we will show next, which is due to the symmetry in the detector unit cell.

The BNL dual-column 3D detector is compared with other dual-column 3D detectors: the standard one developed by Parker (Parker 1997), and the one developed by IMB-CNM (Barcelona), where p-type and n-type columns are placed to the opposite surfaces as shown in Figure 3.19 (Fleta 2007).

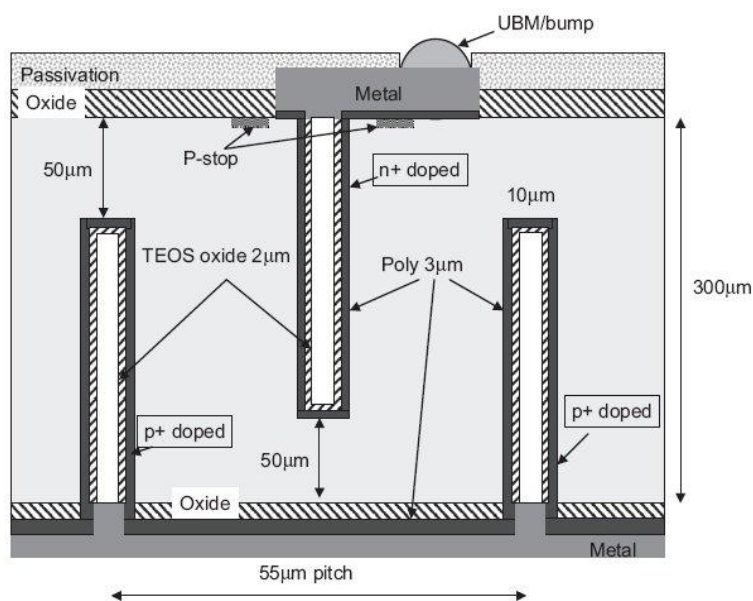


Figure 3.19: Sketch of a 3D detector featuring columnar electrodes of n- and p-doping type proposed by IMB-CNM (Fleta 2007). In this structure the columnar electrodes are etched from opposite sides of the wafer.

Comparing different dual-column 3D detector structures, the electric field profiles are extremely similar in the vast bulk of the detectors; only minor differences are found on the surface of the detector at 100 V bias, as shown in Figure 3.20.

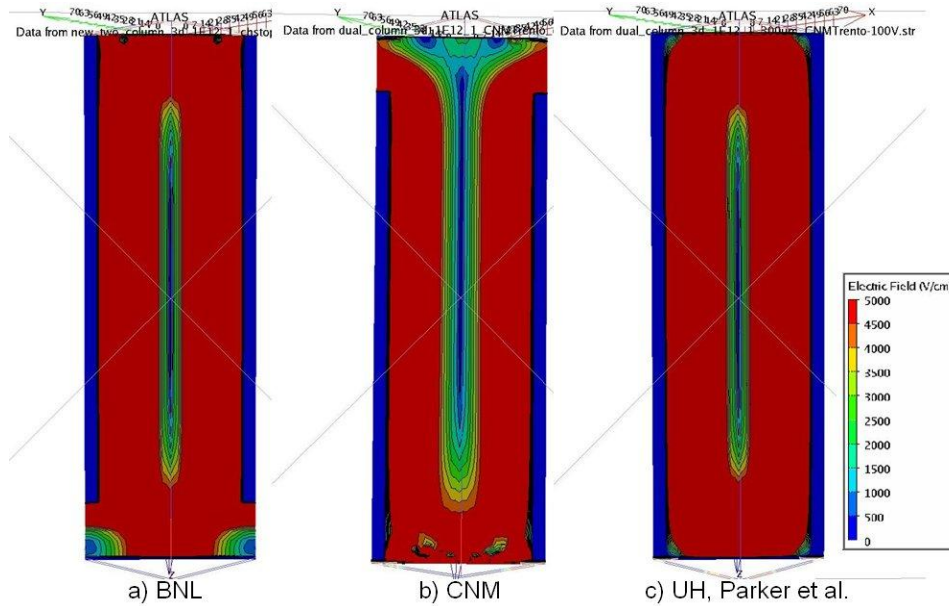


Figure 3.20: Comparison of the electric field profiles between three types of dual-column 3D detectors operated at 100 V bias. The 2D cut plane is along the two n^+ columns.

In fact, one of the main differences among various types of dual-column 3D detectors is the processing. The processing of a BNL dual-column 3D detector is true one-sided process, both in terms of detector processing and detector access. It is clear that one-sided processing is far simpler and cheaper than double-sided one. Single-side access can also be simple, but in some cases, double-sided access may be desirable due to the fact that different voltage levels may be separated by the entire thickness of the detector. In the case of one-sided processing, the electrodes do not go all the way through the wafer, which makes these devices mechanically stronger than standard 3D detectors – no support wafer and therefore wafer bonding is necessary.

The main advantages for dual-column 3D Si detectors as compared to 2D planar detectors are: 1) much smaller full depletion bias (depletion between the columns, which can be made in the order of $<70 \mu\text{m}$, and is independent of detector thickness); 2) the drift distance is also significantly reduced in this way, which results in a fast signal, and much improved radiation hardness in terms of CCE if the column spacing is made in the same order of magnitude of that of the trapping distance d_{tr} at the SLHC fluence, and d_{tr} can be in the order of 10's of μm . These are in fact the main reasons that 3D Si detector is one of the detector options for SLHC. The main disadvantages of dual-column 3D detectors as compared to 2D planar ones are the non-uniform electric field profiles including low fields and difficulties in detector processing.

Weighting field. The 3D simulations of weighting field profiles for different 3D detector structures were reported in *Publication V*. The induction of signals in the electrodes of the detectors is generally based on the Shockley-Ramo theorem (Shockley 1938, Ramo 1939, Cavalleri 1971). The theorem states that the instantaneous current induced on a given electrode is equal to the products of the charge of the carrier, its drift velocity v_d (which is proportional to the electric field as simulated before) and the weighting field E_0 (Knoll 2000):

$$i = qv_d \cdot E_0 \quad (3.9)$$

For efficient charge collection, it is required that the maximum electric field arisen from the applied bias should be located in the position of the weighting field maximum. The weighting field is

simulated with the following boundary conditions: potential 1 V to the electrode of interest and 0 V to all others. Figure 3.21 illustrates the simulated weighting field for the BNL single-column detector, whilst Figure 3.22 presents the weighting fields for BNL dual-column detector and another dual-column detector by CNM.

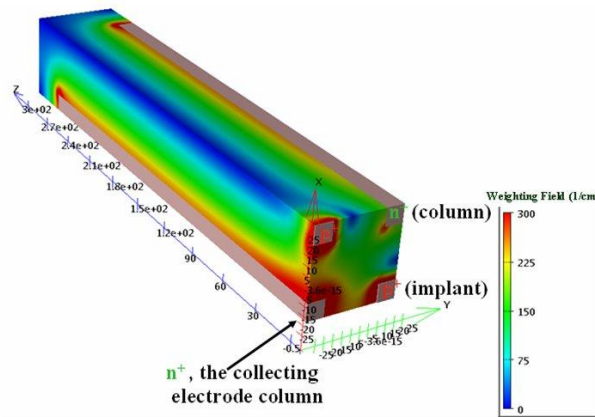


Figure 3.21: Weighting field of the BNL single-column detector.

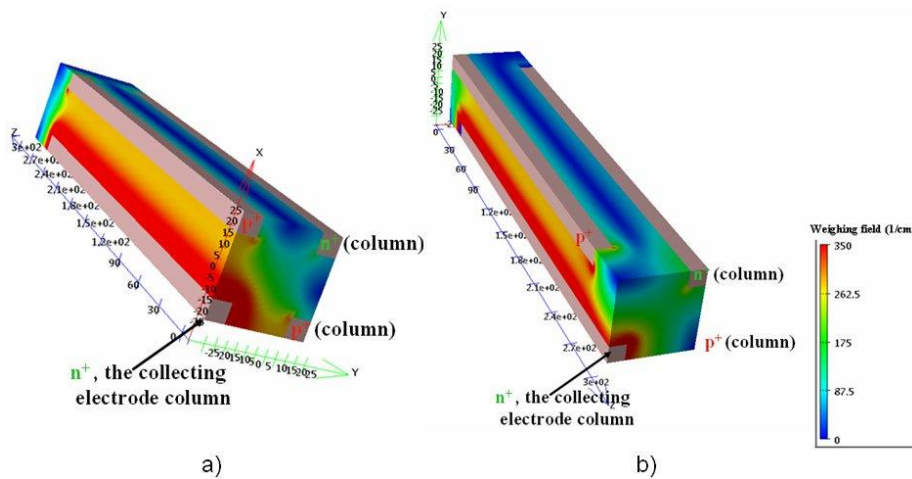


Figure 3.22: Weighting fields of the dual-column detectors a) the BNL dual-column detector and b) the dual-column detector developed by CNM.

It is clear that the high-weighting field region is mainly concentrated along the collecting n^+ column, here on the bottom left corner, extending across the simulation cell. The details of the weighting field distribution are more clearly indicated in the 2D cut plane of the detector. In Figure 3.23, the BNL single- and dual-column detectors have been cut at $150\ \mu\text{m}$ in the middle of the detector thickness. As shown in Figure 3.23b for a BNL dual-column 3D Si detector, the high-weighting field exists within $30\ \mu\text{m}$ from the collecting column, which is more than 60% of the cell length. Two low-weighting field regions are present between the opposite n^+ column and the p^+ columns. This weighting field profile is similar for other types of dual-column 3D Si detectors except near the surfaces.

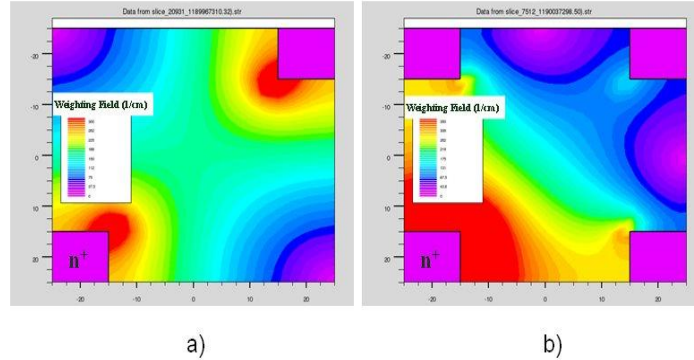


Figure 3.23: Weighting field cuts at 150 μm for a) BNL single-column detector and b) BNL dual-column detector.

As for the BNL single-column 3D Si detector, the high-weighting fields are concentrated near the two n^+ columns, extending 25 μm away from the columns. Two low-weighting field regions exist directly under the p^+ implants.

3.6 Irradiated 3D detectors

As shown in section 2.4, there is a relation between the effective doping concentration and the fluence. The challenge of simulating the radiation damage is the generation of electrically active defects and the donor removal within the device simulator. The effect of bulk damage caused by hadron environment in the Si detectors can be simplified simply by simulating the effect on the doping concentration and varying it. This simulation method gives an insight into the device behavior after radiation damage.

The simulations for dual-column 3D detectors were carried out with a variety of fluences. The simulated full depletion voltage V_{fd} for a dual-column 3D detector shows to be about 1.4 times higher than that of for calculated full depletion voltage of a 2D pad detector with a thickness d , which is the same as the column spacing L_p in the 3D detector. The results are shown in Table 3.1.

Table 3.1: Full depletion voltage, calculated for a 2D detector and simulated for the 3D detector with a thickness d , which is the same as the column spacing L_p in the 3D detector.

Fluence Φ_{eq} [n/cm^2]	Doping concentration N_{eff} [cm^{-3}]	2d pad detector ($d=50\mu\text{m}$) Calculated V_{fd} [V]	Dual-column 3D detectors ($L_p=50\mu\text{m}$) Simulated V_{fd} [V]
5.00×10^{14}	1.00×10^{13}	19	30
1.00×10^{15}	2.00×10^{13}	38	60
2.00×10^{15}	4.00×10^{13}	76	110
3.00×10^{15}	6.00×10^{13}	114	160
4.00×10^{15}	8.00×10^{13}	152	210
5.00×10^{15}	1.00×10^{14}	190	250
6.00×10^{15}	1.20×10^{14}	228	300
7.00×10^{15}	1.40×10^{14}	266	350
8.00×10^{15}	1.60×10^{14}	304	400
9.00×10^{15}	1.80×10^{14}	342	450
1.00×10^{16}	2.00×10^{14}	380	500

Compared with thin planar detectors, 3D detectors need a higher full depletion voltage. Usually the planar detectors used in high-energy physics experiments are 300 μm thick. In that case, the full depletion voltage of 3D detectors is lower with 50 μm column spacing, which is an advantage against planar detectors.

Simulations show that the highest E-field is near the n+ column in dual-column 3D detector (Figure 3.24). The high E-field mainly distributes between the n+ and p+ columns. The low E-field is between the two p+ columns (Figure 3.25a), and the lowest E-field is in the center of the simulation cell with two p+ columns and two n+ columns (Figure 3.25b).

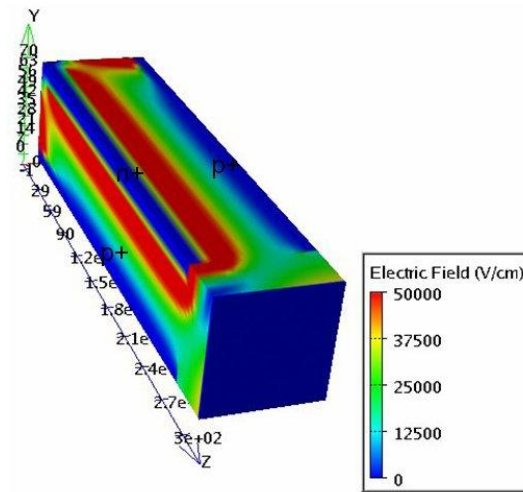


Figure 3.24: Electric field, $\phi_{eq} = 4 \times 10^{15} \text{ n}_{eq} / \text{cm}^2$, $V = 200 \text{ V}$.

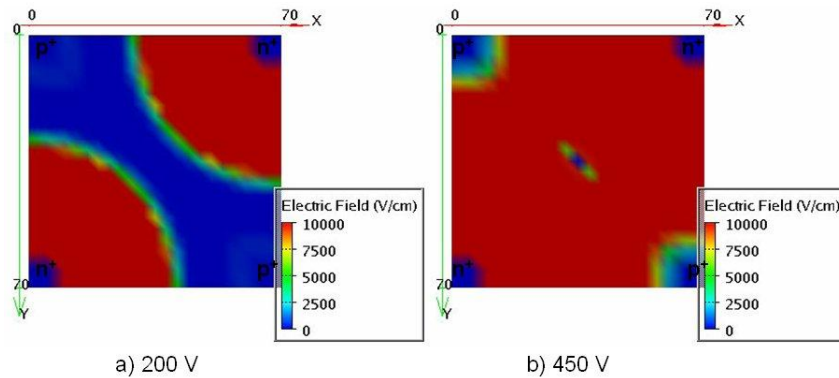


Figure 3.25: Electric field. Fluence $\phi_{eq} = 9 \times 10^{15} \text{ n}_{eq} / \text{cm}^2$ and the applied voltage is a) $V = 200 \text{ V}$ and b) 450 V .

Figure 3.25a shows that when detector is under the full depletion voltage (200 V), the low-electric-field area is between p-type electrodes. When reaching full depletion in Figure 3.25b, almost the all detector space has a high electric field, only in the middle of the structure is a spot of low-electric-field area.

In the future, high-energy physics experiments require very high fluences up to $1 \times 10^{16} \text{ n}_{eq} / \text{cm}^2$. In order to fully deplete a dual-column 3D detector at $1 \times 10^{16} \text{ n}_{eq} / \text{cm}^2$ with a reasonable bias ($\leq 200 \text{ V}$), the column spacing L_p should be reduced to 30 μm (Fig. 3.26).

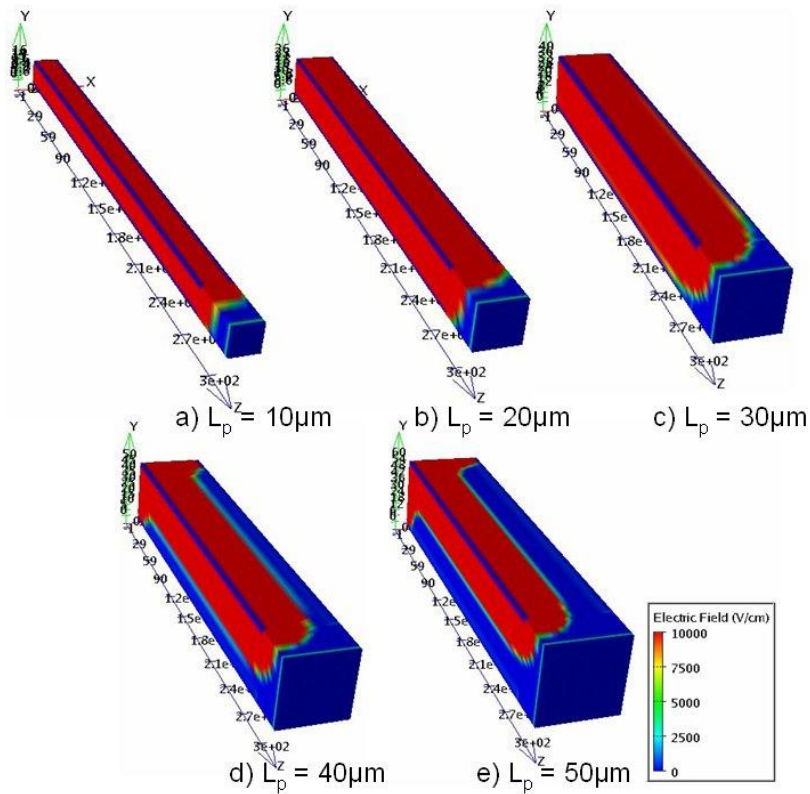


Figure 3.26: Electric field, $\phi_{eq} = 1 \times 10^{16} \text{ n}_{eq} / \text{cm}^2$, $V = 200 \text{ V}$, L_p varies from $10 \mu\text{m}$ to $50 \mu\text{m}$.

The volume under the columns (10% of the total volume) can be depleted with a modest bias ($\leq 200 \text{ V}$), and this volume under the columns is not dead volume (Fig.3.27).

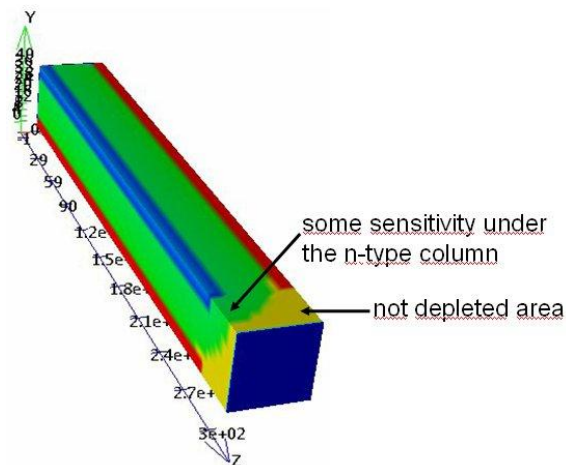


Figure 3.27: Depletion in 3D detector with $L_p = 30 \mu\text{m}$ at 200 V and $\phi_{eq} = 1 \times 10^{16} \text{ n}_{eq} / \text{cm}^2$.

In Figure 3.27, the depletion volume can provide some detection sensitivity directly under the columns, which may reduce the effective dead volume in 3D detectors.

3.7 Comparison of n- and p-type 3D detectors

Comparing various 3D detector structures, simulation results show that the dual-column detectors are at best in the radiation-hard environments, but single-column detectors are easier to process. The electric field profile (active area of the detector) is the best in the dual-column detectors including the standard 3D detector. The single-column detectors suffer from the non-uniform electric field, although in BNL single-column 3D detectors, some high field can be developed along the junction column. The n-type 3D detectors are not very suitable for high-energy physics experiments because of the large low-field area and the type inversion of the detector type. The advantages and disadvantages are summarized in Table 3.2.

Table 3.2: Summarizing comparison of the properties of different 3D detector structures.

Structure	E-field profile	Rad-hard	Mechanical integrity	Processing	Accessibility	Sensitivity under the column
P-TYPE						
Std 3D (UH)	Good	Super	Good with supporting wafer	Difficult, wafer bonding needed	One-side	Some reported (Da Via 2006)
BNL dual-C	Good	Super	Good	True one-sided	One-side	Some
CNM dual-C	Good	Super	Good	Double-sided	Two-side	Some
BNL single-C	Low field on the back side	Good	Good	True one-sided	One-side	Some
Trento single-C	Low field on the front and center	Good	Good	One-sided (backside uniform ion implant and metallization)	Two-side	Some
N-TYPE						
Semi 3D	Low field on the front	Suffers from SCSi	Good	One-sided	Two-side	Some

Also the 3D simulations of weighting field profiles for different p-type 3D detector structures verify that the high-weighting field has been found to exist in more than half of the volume in the detector unit cells, which should be a significant advantage for 3D detectors.

3.8 Active edge of the detector

In general, planar silicon detectors have a wide insensitive border region around the sensitive area. This insensitive area is occupied by a sequence of guard rings, which control the potential distribution between the sensitive area of the detectors and the die cut to minimize the electric field and the surface leakage current (Fig. 3.28). The need for this area can be avoided if the detector is designed to be edgeless or a trench around the detector bulk is made into an active-edge electrode. In this way, the electric field can extend to within a few microns of the physical edge of the detector when a bias voltage is applied.

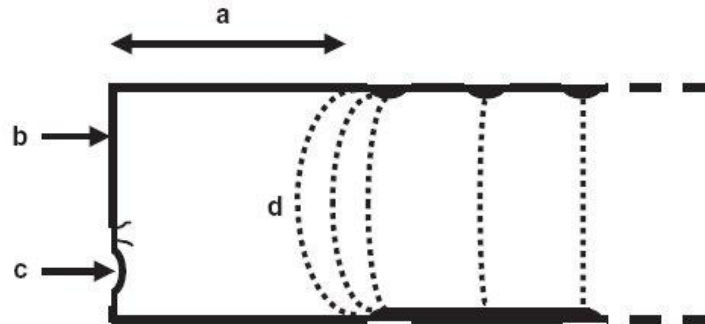


Figure 3.28: Schematic cross-section view of a standard detector edge showing some reasons for an insensitive region there: a) space is needed for guard rings, b) the saw-cut edges are conducting, and c) chips or small cracks must remain clear of d) the bulge of the electric field in the depleted region (Kenney 1999).

Edgeless position sensitive detectors are of interest in imaging applications using non-penetrating radiation such as soft X-rays or vacuum ultraviolet, and in applications where the sensor must be positioned as close as possible to a beam or to a wall. In the first case, the edge sensitivity permits contiguous imaging with overlapped sensors, while in the latter category, particles can be tracked very close to a high-intensity beam (Perea Solano 2006).

Minimizing the dead space is an additional advantage as it enhances the efficiency of a detector (Ranjan 2004). The guard ring technique has evolved to minimize the dead space at the edge of detectors. Also the guard ring structure is used to improve the breakdown performance of silicon detectors. Detectors collect charge from the depletion region. It is therefore important to minimize the dead space, from where it is not possible to collect charge. Usually, depletion is formed vertically from anode to cathode, but *Publication IV* describes a proposed new $p^+/n/n^+$ pad detector structure with n^+ guard ring placed at the edge of the detector (Fig. 3.29), where the depletion region also extends sideways. This phenomenon is due to the cathode and the guard ring being of the same doping type. The remaining dead space is only directly under the guard ring.

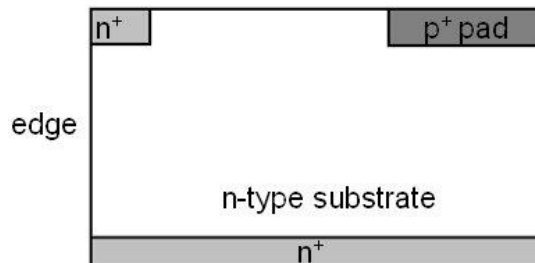


Figure 3.29: Schematic cross-section view of a detector edge with n^+ guard ring placed at the edge of the detector (*Publication IV*).

The same processing procedure performed to fabricate the electrodes in standard 3D detectors can be used to create a trench all around the detector bulk, making it into an active-edge electrode (Kenney 2001). Figure 3.30 shows a sketch of a 3D detector, where the p^+ and n^+ electrodes are processed inside the silicon bulk. The edge is a trench electrode making the active volume sensitive to a few μm from the physical edge when a bias voltage is applied.

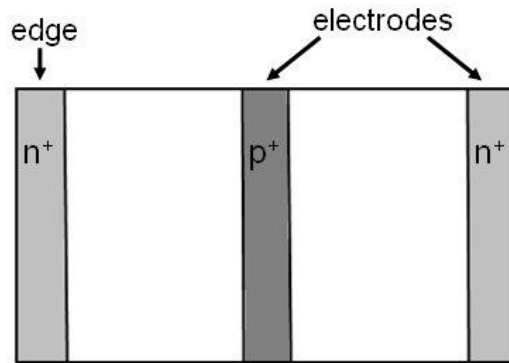


Figure 3.30: Schematic cross-section view of a full 3D-active edge.

Kenney (2006) gives the basic architecture of active-edge planar radiation sensors. Planar/3D-active edge devices have planar microstrips and a three-dimensional edge (Fig. 3.31). The diode junction can be formed either at the edges and bottom or at the top-side electrodes by interchanging n and p. When the diode junction appears at the top-side electrodes, a drawback of the planar/3D design is that the bottom edge corner is very difficult to fully deplete with similarly low bias voltages. Also the disadvantages compared with pure 3D devices are the loss of speed and radiation tolerance.

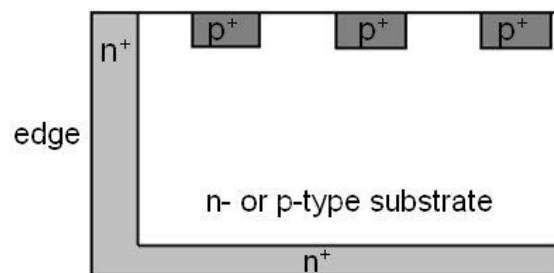


Figure 3.31: Schematic cross-section view of a planar/3D detector edge.

Other methods to reduce the dead edge volume of planar detectors are a cut-through edge operated at cryogenic temperature and a current terminating structure. The latter case is investigated by the TOTEM experiment group, motivated mainly by the need for the measurement of very forward elastic scattering at the CERN LHC near room temperature and preferring production based on the standard planar fabrication technology. These kinds of edgeless detectors are explained in more detail in Ruggiero (2005), Noschis (2006) and Pellegrini (2006).

Chapter 4

Discussion

The interest in the 3D silicon detectors is continuously growing because of their many advantages as compared to conventional planar detectors: the devices can be fully depleted at low bias voltages, the speed of the charge collection is high, and the collection distances are about one order of magnitude less than those of planar technology strip and pixel detectors with electrodes limited to the detector surface. Also the 3D detectors exhibit high radiation tolerance, and hence the ability of the silicon detectors to operate after irradiation is increased. The properties of 3D and planar detectors are compared in Table 4.1.

Table 4.1: 3D versus planar detector design parameters for a 300 μm thick silicon substrate. The depletion voltage quoted is for a detector prior to irradiation (Da Via 2003b).

Parameter	3D	Planar
Depletion voltage	$< 10 \text{ V}$	70 V
Collection length	$\sim 50 \mu\text{m}$	300 μm
Charge collection time	1-2 ns	10-20 ns
Edge sensitivity	$< 10 \mu\text{m}$	$\sim 300 \mu\text{m}$

To achieve some of the prime goals of high-energy physics experiments – for example the discovery and possible study of Higgs particles – the silicon detectors have to operate in an extreme harsh radiation environment. To achieve the properties of silicon detectors needed for such applications, the radiation degradation has to be minimized. This is done by device and defect engineering. Defect analysis and 3D detectors are the hottest topics in the future in the area of detecting particles in high-energy physics experiments.

In this study, the radiation detectors have been researched. The effect of radiation to the detectors has been characterized by simulations. The simulations on the radiation damage are done by varying the effective carrier concentration N_{eff} . This simulation method gives an insight into the device behavior after radiation damage. It is clear that radiation will cause irreversible damage in the detector bulk material. The radiation-induced changes in the macroscopic silicon detector properties such as leakage current, depletion voltage and charge collection efficiency are caused by radiation-induced electrically active microscopic defects. The challenge of simulating the radiation damage is the generation of electrically active defects and the donor removal within the device simulator.

Highly energetic ionizing particles, while crossing the detector, interact with the silicon layer resulting in the generation of electron-hole pairs along their path. Electron-hole pairs can be collected at the electrodes of an inversely biased junctions, but if the energy of the highly energetic ionizing particles is high enough, a lattice atom can be displaced from its original position and two defects are generated in the silicon lattice (Passeri 2001, Petasecca 2005a), namely an interstitial atom and a vacancy. Most of the generated interstitials and vacancies quickly recombine because of their very high mobility, but a significant proportion of them can interact with impurities to produce electrically active defects, whose energy is located within the forbidden band. These defects behave as recombination-generation centers in the band gap and act as traps for carriers (Petasecca 2005a, Petasecca 2005b).

It has been shown elsewhere (Passeri 2001, Petasecca 2005a, Petasecca 2005b, Petasecca 2006) that the radiation damage effects can be described with a three-level radiation damage model (known as the Perugia trap model) to be used in simulations. The model is based on the progressive introduction of radiation-induced defects. Two main defects in the silicon bulk are related to the divacancy and to

the carbon-oxygen complex. The presence of these defects causes the radiation-induced changes in the electrical properties of the detector. For n-type silicon, the three-level model is defined with two acceptor levels located at $E_c - 0.42$ eV (V_2) and $E_c - 0.55$ eV (V_2O), and a donor level located at $E_v + 0.36$ eV (C_iO_i) (Ahmed 2001, Petasecca 2005b). In proportion, the three-level model for p-type silicon has a divacancy defect level located at $E_c - 0.42$ eV (V_2), a tri-vacancy complex defect (Ahmed 2001) located at $E_c - 0.46$ eV (V_3) and a donor defect C_iO_i complex located at $E_v + 0.36$ eV (Petasecca 2006).

There is only incomplete knowledge on the defect properties, and therefore, it is very difficult to determine the concentrations of impurities. The damage modeling in Silvaco simulation program also require information about activation energies, the cross sections for majority and minority carriers and the trap concentrations of main defects. All this information is difficult to find for the specific defect level. Moreover, it has been shown that trapping times of the Perugia model do not match with the experimental trapping times (Pennicard 2007).

In Silvaco, the command *trap* activates bulk traps at discrete energy levels within the bandgap of the semiconductor and sets their parameter values. For example, the three-level radiation damage model can be defined in the Silvaco program as follows:

```
#... Three-level damage model for p-type
trap acceptor e.level=0.42 sigp=2e-6 sign=5.4e-9 density=7.5e11 degen=1
trap acceptor e.level=0.46 sigp=7e-15 sign=3.2e-12 density=5e11 degen=1
trap donor e.level=0.36 sigp=1.2e-10 sign=5.1e-23 density=1e12 degen=1
```

The type of the trap level is defined as *acceptor* or *donor*. *E.level* sets the energy of the discrete trap level. For acceptors, it is relative to the conduction band edge. For donors, it depends on the valence band edge. *Sigp* and *sign* specifies the capture cross section of the trap for holes and for electrons. The average capture time increases exponentially with depth and is inversely proportional to the capture cross-section (Lutz 2001). Instead of capture cross-sections, the electron and hole lifetimes can be specified. *Density* sets the maximum density of states of the trap level and *degen* specifies the degeneracy factor of the trap level used to calculate the density (ATLAS 2007).

Some values for the capture cross-section of the trap for holes and for electrons and also for the density of traps are reported in the literature (Hallen 1996, Bleichner 1996). The problem is that all the necessary information is not very well known for specific traps, and more information is needed to complete radiation-induced defect simulations with the Silvaco program.

Also it has been reported that the concept of double-peak electric field distribution in irradiated Si detectors can be expressed with a trap model (Verbitskaya 2007). The model of this DP electric field profile $E(x)$ distribution is based on trapping of equilibrium carriers to the midgap energy levels of radiation-induced defects that leads to a non-uniform distribution of space charge concentration with positively and negatively charged regions adjacent to the p^+ and n^+ contacts, respectively. The model takes into account the trapping of free carriers from the bulk generation current to the midgap energy levels of radiation-induced defects: a deep donor (DD) and a deep acceptor (DA) with the activation energies of $E_v + 0.48$ eV and $E_c - 0.52$ eV, respectively. From this point of view, when the traps are known better, the simulation of the double-peak electric field profile distribution is possible in the future.

The signal formation in 3D detectors is very important research field for understanding the properties of 3D detectors in terms of speed and charge collection efficiency. One way to study the signal is the calculation of electric and weighting fields as shown earlier. The second method is to simulate a certain amount of charge injected along a straight line or locally in the detector and analyze the time domain response. This kind of simulation can be done in Silvaco with *single-event upset* command. It enables to specify the radial, length, and time dependence of the generated charge along tracks. There

can be a single particle strike or multiple strikes. Figure 4.1 shows the first result of the transient simulations of the BNL dual-column detector. The charge collection was studied by introducing a minimum ionizing particle (MIP) that penetrates through the whole detector in the middle of the structure with the bias of 50 V. The voltage has been chosen to be higher than full depletion voltage, because it increases the electric field and thereby speeds up the charge collection. About 24 000 electron-hole pairs is created uniformly along the path in the silicon.

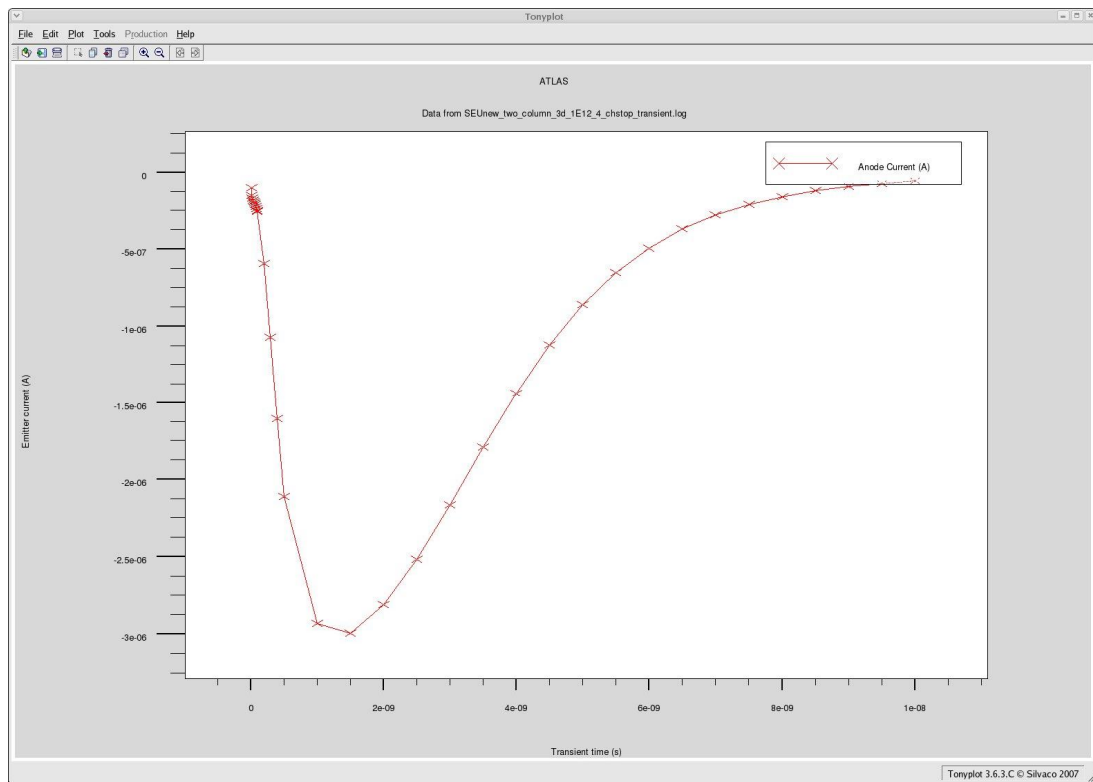


Figure 4.1: Charge collection time dependence of the BNL dual-column detector at 50 V bias and the charge traveling through the whole detector in the middle of the structure.

Figure 4.1 shows the dual-column 3D detector current response pulse from the center of the simulation cell shown in Figure 3.12. It can be seen that there is a delay, when a current pulse is returning back to the zero level causing a pulse tail. This is caused by the uniform surface charge at the silicon/oxide interface. The surface recombination causes some of the charge carriers to recombine, and thus, diffusion is caused toward the oxide, and the charge collection time increases. More research is needed to study the charge collection properties of 3D detectors in the future.

Chapter 5

Conclusions

In this study, the various radiation detector structures were simulated and characterized to find an applicable silicon detector, which can operate in extremely harsh radiation environments such as in the experiments of the future Super-LHC. In the nearest region of the beam in Super-LHC, 3D-detectors are almost the only detector choice because of their radiation hardness. The full depletion voltage and the electric field distribution of 3D detectors were under investigation in this study. As expected, the full depletion voltage is lower in 3D detectors than in common planar detectors, because the charge collection distance is notably shorter, consisting only of the distance between the columnar electrodes. The drawback in 3D detectors is the non-uniform electric field, which reduces the sensitivity volume of the detector. That is why electric field distributions in various detector structures were studied. The optimization of the electric field distribution can ensure fast and efficient detector operation. Therefore, the knowledge of the electric field distribution is important for the prediction of detector operation in harsh radiation environments.

The key contributions of this study include the following:

- This study shows that the main reasons why 3D Si detector is one of the detector options for SLHC are: 1) far smaller full depletion bias voltage, because the needed depletion volume is between the columns, which can be made in the order of $<70\ \mu\text{m}$, and is independent of the detector thickness; 2) this way the drift distance is also notably reduced, which results in a fast signal, and substantially improved radiation hardness in terms of CCE if the column spacing is made in the same order of magnitude of that of the trapping distance d_{tr} . At SLHC fluence, d_{tr} can be in the order of 10^3 s of μm .
- The study of the electric field distribution in n-type 3D detectors with partial-penetrating electrodes. Both the simulation results and the SEM measurement results show that the charge-collecting field (electric field) is formed only below the electrode pillars. With the high bias voltage, the electric field is mainly formed between the end of the pillars and the backside. The front side of the detector suffers from the low electric field, and consequently, the charge collection efficiency is reduced.
- The simulation study of the electric field distribution in p-type 3D detectors with single-type of the columns. The electric field distribution in the studied single-column p-type 3D detector structure shows to have many advantages compared with other types of single-column 3D detectors: 1) the high electric field shows to be on the sensing electrode side; and 2) some high electric field can be developed along the junction column as the bias voltage increases. However, the single-column detectors suffer from a more complicated, non-uniform electric field profile than dual-column detectors as shown in the simulation results. Single-column p-type 3D detectors are more radiation hard than the planar detectors because of their lower depletion voltages.
- The simulation study of the electric field distribution in p-type 3D detectors with dual-type of the columns. The electric field profile in a dual-column 3D Si detector is more uniform than that in the single-type column 3D Si detector: the non-uniformity is minimal along the detector thickness. The field profiles for all types of the studied dual-column 3D detectors are similar with just some minor differences on the front and back surfaces. The dual-column detectors are the best in radiation hardness because of their low depletion voltages and short drift distances.
- The simulations show that the volume under the columns where it is supposed to constitute the dead space (about 10%) can be depleted at high biases with a modest electric field, leading to the possibility of recovering some sensitivity from this region. This region can also provide some sensitivity to particle tracks directly through the columns.

- Dual-column p-type substrate 3D detectors were simulated with a variety of fluences to study the effect of the irradiation on the detector performance. The simulated full depletion voltage V_{fd} for a dual-column 3D detector shows to be about 1.4 time higher than that of for the calculated full depletion voltage of a 2D pad detector with a thickness d , which is the same as the column spacing L_p in the 3D detector. Simulations also show that in order to fully deplete a dual-column 3D detector at $1 \times 10^{16} \text{ n}_{eq}/\text{cm}^2$ with a reasonable bias ($\leq 200 \text{ V}$), the column spacing L_p should be reduced to $30 \mu\text{m}$.

Suggestions for future work. The study shows that in the future, defects and charge collection in the detectors studied here should be taken under further investigation as suggested in Discussion. More information is needed about the charge trapping: what are the effective traps and their parameters in the radiated silicon detector? *Ab initio* calculations can provide reliable estimates for the defect electrical levels, together with information about the defect concentrations and the migration energies. These data can then be used as input for the Silvaco program, thereby connecting the nanoscale with device-scale engineering.

Electrically active defects are responsible for the changes in the operation of the particle detectors. This causes the degradation of the overall charge collection efficiency. The deterioration of CCE caused by the trapping of charge carriers will be the most severe obstacle for the use of silicon detectors in the future very high-luminosity colliders with extremely harsh radiation environments. The main effect of the radiation damage on the macroscopic silicon detector properties is the decrease in the charge drift lifetime, which reduces the CCE from the depleted region. In addition to the trapping of free carriers causing the reduction in the CCE amplitude, the detector has to be fully depleted for achieving the maximal signal amplitude. Also, the high concentration of the radiation-induced deep traps leads to the electric field distortion, where there is the double-peak electric field distribution. The CCE depends on both the charge trapping and the electric field, and it is the most crucial parameter in the radiation detector research. It can be studied with the following methods listed in Table 5.1, which also shows the quantities that can be defined.

Table 5.1: Characterization methods and the desired quantities to be studied. In this study, the TCAD simulation tool was used to analyze the full depletion voltage V_{fd} and the electric field distribution $E(x)$. In the future research including TCAD simulations, the charge trapping and the charge collection efficiency CCE should be investigated further.

Measurement setup	$E(x)$	τ_{trap}	V_{fd}	CCE
CV			x	
TCT	x	x	x	
SEM	x			
CCE			x	x
TCAD simulation	x	x	x	x

Charge collection can be simulated introducing a certain amount of charge traveling through the detector. The first results were presented in Figure 4.1; however, it is necessary to study the charge collection in various detector structures further. Also for future studies and simulations, the integration of the electric field and the weighting field is highly important; one can calculate the actual induced current in 3D Si detectors under various radiation fluences, and then analyze the CCE of the detector.

Appendix A

Silvaco TCAD software

Silvaco TCAD software allows the creation, fabrication and simulation of semiconductor devices and their electrical performances. In this study Silvaco TCAD was run under the Linux environment, yet it also can be run under Windows. The software is divided into several different programs, which all have a purpose of their own in the whole simulation chain (Fig. A.1). DeckBuild is the program, which runs the files under the simulation. With the ATHENA program, the semiconductor manufacturing process can be simulated and the semiconductor device can be created. The semiconductor device can also be described by the DevEdit/DevEdit3D program, but mostly it is used to edit the mesh or grid of the device to optimize it for the simulation run and the most interesting points of the device. With DevEdit3D, the three-dimensional structures can be created. ATLAS is the device simulation program, which is needed in every case for simulation of the electrical characteristics of the semiconductor devices. Also this program can be used to describe semiconductor devices by inserting the doping profiles. Finally, after the simulation run, the TonyPlot or TonyPlot3D is used to visualize the semiconductor device and its electrical characteristics.

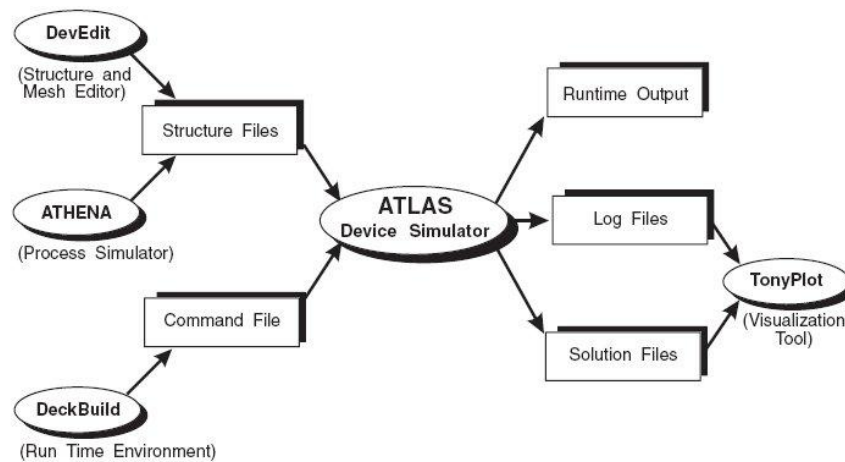


Figure A.1: Programs and information flow in Silvaco TCAD (ATLAS 2007). DevEdit, DeckBuild and TonyPlot form a Silvaco Virtual Wafer Fab (VWF) environment. ATHENA and ATLAS are the process and device simulation softwares. The input files of ATLAS are the command file from DeckBuild, which performs the simulation run and the structure file from either DevEdit or ATHENA or from both. In this file, the studied device structure is defined.

A.1 DeckBuild

DeckBuild is the surface between different simulation programs. In DeckBuild, the code for simulation is run; there it is possible to move freely from one simulation program to other, for example from ATHENA to DevEdit and finally to ATLAS. It provides an interactive run-time environment. DeckBuild can be used to create or edit input decks, or just load the ready input deck for the simulation run. Instead of using DeckBuild, the input code can be built in any text editor program and saved as an input file type. After that, these files can be loaded in DeckBuild and run.

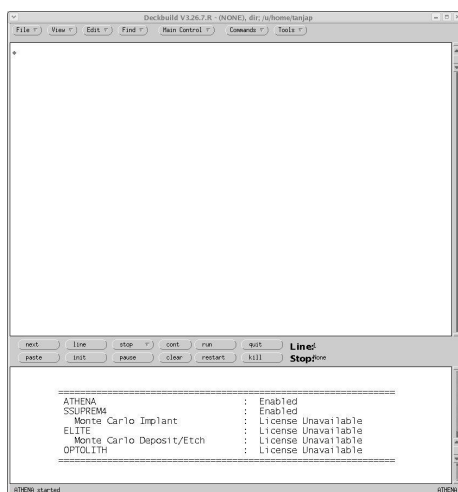


Figure A.2: DeckBuild base window.

The DeckBuild base window consists of two subwindows; an upper one for building, editing and showing the input decks and a lower one for running the simulation (Fig. A.2). This window shows the simulation steps and possible error messages. ATHENA is the default simulation program, when starting DeckBuild.

A.2 ATHENA

ATHENA is a simulator that provides general capabilities for numerical, physically based, two-dimensional simulation of semiconductor processing. Physically based process simulators predict the structures that result from specified process sequences. This is done by solving systems of equations that describe the physics and chemistry of semiconductor processes. A detailed analysis of various aspects of process simulation can be found in Plummer (2000).

An ATHENA simulation program has a modular architecture and several different tools. The ATHENA tool performs structure initialization and manipulation and also provides basic deposition and etch facilities. The SSUPREM4 tool is used in the design, analysis, and optimization of silicon semiconductor structures. It simulates silicon processing steps such as ion implantation, diffusion and oxidation. The simulation is done by first defining the problem. In ATHENA, the problem is specified by defining the initial geometry of the structure and the sequence of process steps (e.g. oxidation, implantation, etching, diffusion) that are to be simulated. The example of an ATHENA simulation is given in Appendix A.6.

ATHENA predicts the physical structures that result from processing. These physical structures are used as input by ATLAS, which then predicts the electrical characteristics associated with specified bias conditions. Using ATHENA and ATLAS makes it possible to determine the impact of process parameters on device characteristics.

A.3 ATLAS

ATLAS is a physically based two- and three-dimensional device simulator, which predicts the electrical characteristics that are associated with specified physical structures and bias conditions. This is achieved by approximating the operation of a device onto a two- or three-dimensional grid,

consisting of a number of grid points called nodes. By applying a set of differential equations, derived from Maxwell's laws, onto this grid the transport of carriers through a structure can be simulated. The electrical performance of a device can be modeled in DC, AC or transient modes of operation.

In ATLAS, the problem to be simulated is specified by defining the physical structure, the physical models and the bias conditions for which electrical characteristics are to be simulated. The order in which statements occur in an ATLAS input file is important. There are five groups of statements (Table A.1) that must occur in correct order. The order of statements within the mesh definition, structural definition, and solution groups is also of importance. Otherwise, it may cause incorrect operation or termination of the program. For further information of statements, the reader is referred to ATLAS 2007 manual. The example of an ATLAS simulation code is given in Appendix A.6.

Table A.1: The Atlas commands.

<i>Group</i>	<i>Statements</i>
Structure specification	mesh region electrode doping
Material models specification	material interface model contact
Numerical method selection	method
Solution specification	log solve save load
Result analysis	extract tonyplot

S-PISCES is a two-dimensional device modeling program that simulates the electrical characteristics of silicon-based semiconductor devices. It calculates the internal distributions of physical parameters and predicts the electrical behavior of devices under either steady-state, transient, or small signal AC conditions. This is performed by solving Poisson's equation and the electron and hole carrier continuity equations in two dimensions. S-PISCES solves basic semiconductor equations on non-uniform triangular grids. Doping profiles and the structure of the device may be obtained from analytical functions, experimentally measured data, or from process modeling programs SSUPREM4 and ATHENA. DEVICE3D provides the semiconductor device in three-dimensional mode. It uses the same analog as the S-PISCES in the two-dimensional simulations.

A.4 DevEdit

DevEdit is a device structure editor (Fig. A.3). It can be used to generate a new mesh on an existing structure or to create or modify a device. These devices can then be used by Silvaco 2-D and 3-D simulators. DevEdit can perform the following operations: definition of a device for subsequent device simulations, and remeshing a device structure between or during a process and device test simulations, when the process simulator does not create a good grid for the device simulator or when the mesh is no longer adequate for the next simulation step.

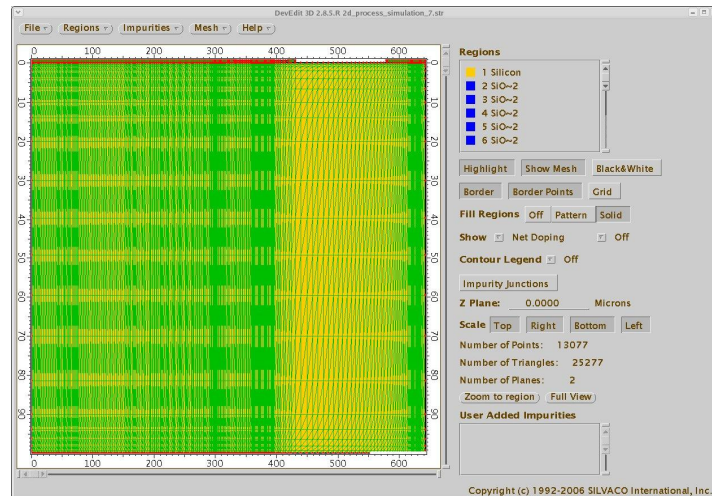


Figure A.3: DevEdit base window.

Defining the mesh is very critical in Silvaco simulations. First, the number of nodes in two-dimensional simulations is limited to 20 000, which is not much considering wide and high-radiation detector structure simulations. Because quite high voltages are applied in these applications, placing the nodes to the right places is also very important. Otherwise, the convergence problem during simulation run is reported and simulation is not finished correctly.

A.5 TonyPlot

TonyPlot is a graphical post processing tool for use with all Silvaco simulators, and it is an integral part of the Virtual Wafer Fab. Similarly, TonyPlot3D is a three-dimensional graphics viewer, capable of displaying data generated from the 3D process and device simulators (Fig. A.4).

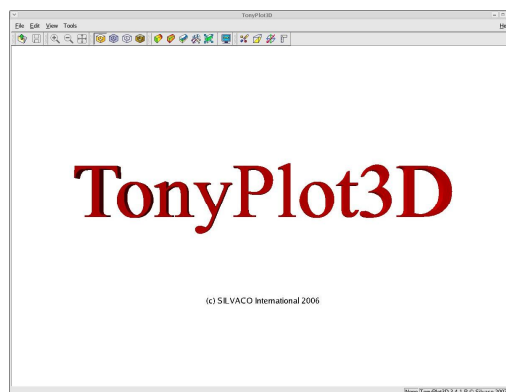


Figure A.4: Tonyplot3D window.

A.6 SIMULATION SOURCE CODE

Next, an example of simulation source code is given. The simple diode structure is simulated to show the operation of pn junction under the reverse bias. First, ATHENA is started for the process simulation. All command lines in the program start with #.

```
# Process simulation - ATHENA
# file: /u/home/tanjap/Simulation/pn_junction.in

go athena
```

The x- and y-dimensions of the structure are given with the space of grid.

```
#
# Mesh definition
#
line x loc=0.0 spac=5
line x loc=5.0 spac=3
line x loc=10.0 spac=1
line x loc=15.0 spac=2
line x loc=35.0 spac=1
line x loc=40.0 spac=3
line x loc=45.0 spac=5
line x loc=50.0 spac=5
#
line y loc=0.0 spac=0.5
line y loc=1.0 spac=1
line y loc=3.0 spac=1
line y loc=5.0 spac=2
line y loc=10.0 spac=3
line y loc=20.0 spac=5
line y loc=30.0 spac=5
line y loc=40.0 spac=5
line y loc=50.0 spac=5
```

The doping of silicon is given.

```
#
# Initial silicon structure
#
# n (1E13 cm-3)
init silicon c.phosphorus=1e13 orientation=111
```

The first processing step is to deposit oxide and aluminum on top of the structure and then etch them for the p-type pad implantation.

```
# ===== Oxide Cut for Boron implant =====
# ===== (p+) =====
# ===== Implantation Mask for Boron =====
#
deposit oxide thick=0.50 divisions=10
#
etch oxide start x=10 y=-0.5
etch cont x=10 y=0
etch cont x=40 y=0
etch done x=40 y=-0.5

deposit alumin thick=1.0 divisions=10

etch alumin start x=10 y=-1.5
etch cont x=10 y=0
etch cont x=40 y=0
etch done x=40 y=-1.5
```

Processing of the p-type pad is carried out by implanting boron. Then contacts are made by depositing aluminum both on the front side and backside.

```
# ===== Implantation =====
# ===== implanting p+ with energy 25keV and dose 1e15cm-2 =====

#
implant boron dose=1e15 energy=25 pearson tilt=7 rotation=0 crystal
#

# Etch aluminum (implantation mask)
etch aluminum all
```

```

# ===== Aluminum Contact =====
# ===== Front side =====
#
deposit alumin thick=1.0 divisions=25

etch alumin start x=0 y=-2
etch cont x=0 y=-0
etch cont x=10 y=-0
etch done x=10 y=-2

etch alumin start x=40 y=-2
etch cont x=40 y=-0
etch cont x=50 y=-0
etch done x=50 y=-2

# ===== Aluminum Contact =====
# ===== Backside =====
#
struct flip.y

deposit aluminum thick=0.30

struct flip.y
# =====

```

Electrodes are named and the structure created is saved for device simulation.

```

# Name and the place of the electrode
electrode name=anode x=25 y=-0.1
electrode name=cathode x=25 y=50.1

# Saving the created structure
struct outfile=/u/home/tanjap/Simulation/pn_junction.str

# Plotting the structure
tonyplot

```

The device simulation starts by using ATLAS. First, necessary parameters are given and simulation models and methods are defined.

```

# Device simulation - ATLAS

go atlas

# Load mesh file created during process simulation
mesh inf=/u/home/tanjap/Simulation/pn_junction.str

# Adding work function to the electrodes
#
# SiO2 - Si surface charge
interface qf=4e11

# Simulation models
models bipolar numcarr=2
impact selb

# Simulation methods
method newton trap ilimit=20 maxtraps=10

```

Solving the device with a variety of bias voltages starts.

```

# Solving the initial solution
solve init

# Saving the voltages and currents
log outf=pn_junction.log

# Defining output type
output e.field
output flowlines
#
#####
#### Bias voltages applied ####
# anode = -0.5V...-30V (1) electrode #

```

```
#####
#
solve vstep=-0.1 nsteps=5 elec=1
save outf=/u/home/tanjap/Simulation/pn_junction-p(-0.5V).std master

load inf=/u/home/tanjap/Simulation/pn_junction-p(-0.5V).std master
solve vstep=-.1 nsteps=5 elec=1
save outf=/u/home/tanjap/Simulation/pn_junction-p(-1.0V).std master

load inf=/u/home/tanjap/Simulation/pn_junction-p(-1.0V).std master
solve vstep=-.1 nsteps=5 elec=1
save outf=/u/home/tanjap/Simulation/pn_junction-p(-1.5V).std master

load inf=/u/home/tanjap/Simulation/pn_junction-p(-1.5V).std master
solve vstep=-.1 nsteps=5 elec=1
save outf=/u/home/tanjap/Simulation/pn_junction-p(-2.0V).std master

load inf=/u/home/tanjap/Simulation/pn_junction-p(-2.0V).std master
solve vstep=-.1 nsteps=30 elec=1
save outf=/u/home/tanjap/Simulation/pn_junction-p(-5.0V).std master

load inf=/u/home/tanjap/Simulation/pn_junction-p(-5.0V).std master
solve vstep=-.1 nsteps=50 elec=1
save outf=/u/home/tanjap/Simulation/pn_junction-p(-10.0V).std master

load inf=/u/home/tanjap/Simulation/pn_junction-p(-10.0V).std master
solve vstep=-.1 nsteps=100 elec=1
save outf=/u/home/tanjap/Simulation/pn_junction-p(-20.0V).std master

load inf=/u/home/tanjap/Simulation/pn_junction-p(-20.0V).std master
solve vstep=-.1 nsteps=50 elec=1
save outf=/u/home/tanjap/Simulation/pn_junction-p(-25.0V).std master

load inf=/u/home/tanjap/Simulation/pn_junction-p(-25.0V).std master
solve vstep=-.1 nsteps=50 elec=1
save outf=/u/home/tanjap/Simulation/pn_junction-p(-30.0V).std master
```

Finally, the simulation results are plotted. The results of this simulation run are presented in Figure 2.3 in Chapter 2. After the plotting, simulation stops.

```
tonyplot
tonyplot pn_junction.log -set diode.set
quit
```

Appendix B

Measurement setups

B.1 CV/IV measurement setup

Capacitance-voltage (CV) measurements yield the depletion voltage and the effective doping concentration. Also, the semiconductor behavior studied by the CV measurements will give information of the behavior of the resistivity, that is, the required depletion voltage as a function of the radiation dose. LUT has measuring equipment for CV measurements, and measurements can be made to high voltages (up to 1100 V). The characterization of the detectors is performed with the CV measurement equipment consisting of a probe station, semiconductor parameter analyzer, LCR meter and separate voltage sources (Fig. B.1).

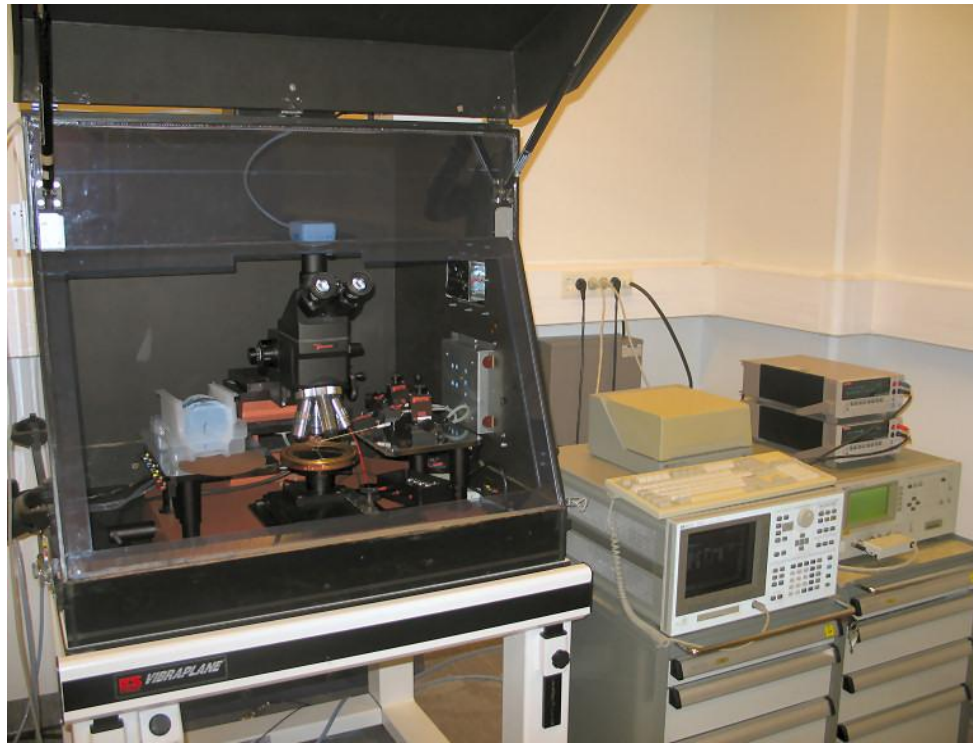


Figure B.1: CV measurement station. On the left, there is the probe station; in the middle, the HP 4155A semiconductor parameter analyzer, and on the right, the HP 4284A LCR meter and the Keithley 2410 voltage sources.

For measuring the capacitance of the detector as a function of voltage, an HP 4284A LCR meter is applied. The voltage range of the LCR meter is 40 volts at maximum. Should a higher voltage be needed, a separate voltage source has to be used. The Keithley 2410 voltage sources can produce high voltages up to 1100 volts. Measuring the current of the detector as a function of voltage, an HP 4155A semiconductor parameter analyzer can be used up to 100 volts. The Keithley 2410 voltage source also includes a current meter, and thus, when higher voltages are required, the current measurements can also be made with the Keithley 2410.

The voltage source and the LCR meter are connected to the probe station and the probe needles by a self-made electronic circuit (Fig. B.2). This electronic circuit is used to isolate the LCR meter from the high voltage by a transformer.

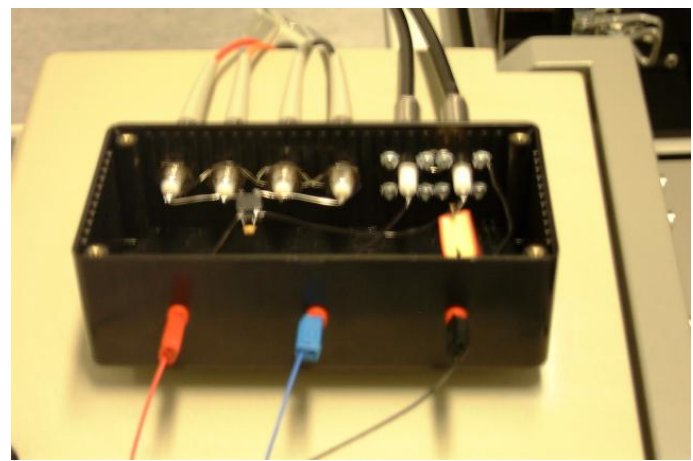
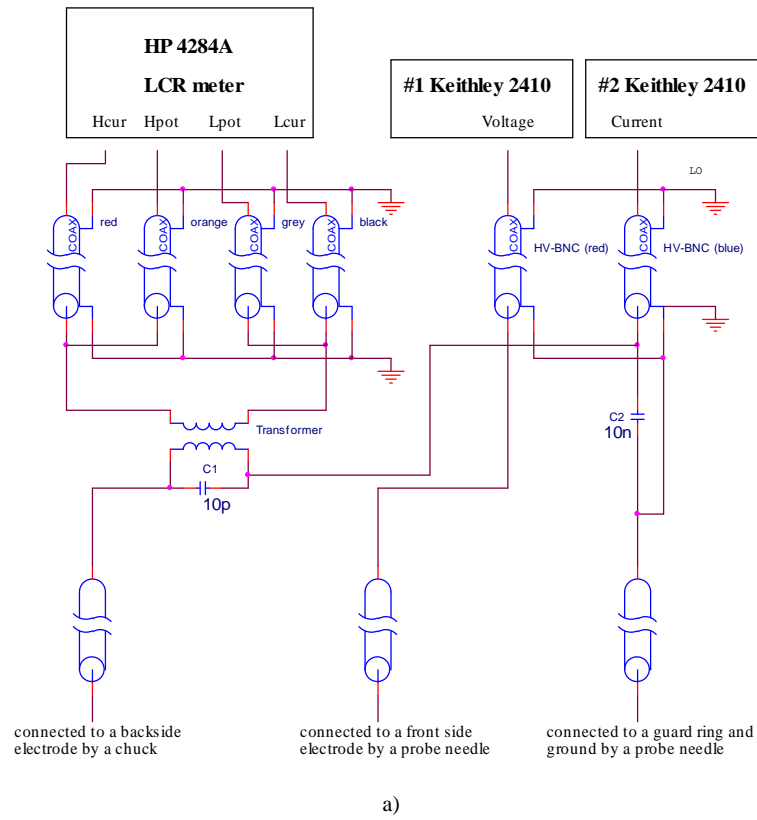


Figure B.2: a) Circuit diagram of the connector between voltage sources, the LCR meter and the probe needles and b) the photo. With this electronic circuit, both IV and CV curves can be measured simultaneously. Keithley no. 1 is used as a voltage source, Keithley no. 2 measures the current and the LCR meter measures the capacitance.

B.2 SEM measurement setup

The type inversion and the double-junction effect have been investigated with several indirect methods: capacitance-voltage (CV) measurements, transient current technique (TCT), optical beam induced current (OBIC), and by measuring the surface potential with a mechanical probe from a cleaved sample (Leinonen 2006). The CV measurements reveal the full depletion voltage, where the effective doping concentration can be calculated. The TCT method is based on the electric field transformation caused by trapping of laser injected carriers. The TCT gives information about the position of the electric field maximum inside the detector through observing the shape and the delay of a current pulse after generating carriers near one surface of the detector with a short laser pulse (Eremin 1994, Eremin 1996). The OBIC technique induces the creation of electron-hole pairs in the sample through the laser signal injection.

Similarly as CV or TCT methods, the above are macroscopic and secondary by nature. The voltage-contrast effect in the scanning electron microscope (SEM) provides a more direct way to measure the desired quantities, that is, the potential distribution and electric field inside the detector structure. This is done by cleaving the detector; now, the examined surface is the cross-section of detector. This way, the potential distribution and the electric field can be measured more directly from the inside of the detector sample. The SEM method provides an accurate microscopic means of imaging and measuring the desired quantities more directly from the sample as a function of position. A drawback is that the device must be split before examination.

The SEM method is based on the voltage-contrast phenomenon. The contrast is converted mathematically to voltage. The simple mathematical equations used in the conversion are explained in detail in Leinonen (2005b). With this SEM measurement method, after splitting the detector, the potential distribution and the electric fields can be imaged and measured straight from the sample. These kinds of measurements are the benefit of the SEM. A drawback of this method is that with this measurement setup the voltage contrast starts to saturate at relatively small voltages. With this method, it is therefore impossible to characterize heavily irradiated detectors under full depletion conditions. With 40-60 V bias, however, a clear, non-saturated voltage-contrast can be seen. This is sufficient to see from which side of the detector the electric field starts to extend (Tuovinen 2006).

The SEM, JEOL JSM-25S III scanning electron microscope was used in this research. This SEM setup is shown in Fig. B.3. A detector is placed in the vacuum chamber of the SEM. The bias voltage is fed over the detector from the Agilent semiconductor parameter analyzer 4155C.

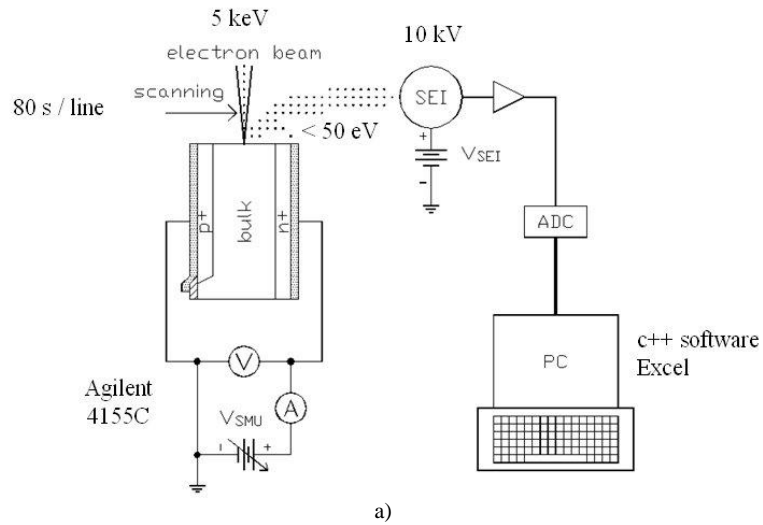


Figure B.3: a) Principal construction of the SEM measurement setup (Leinonen 2005b) and b) the physical layout. 1: Scanning electron microscope. 2: Vacuum chamber. 3: Agilent semiconductor parameter analyzer 4155C. 4: PC used for reading signals from SEM.

One source measure unit (SMU) is constituted by V_{SMU} and its associated voltage and current meters in the semiconductor parameter analyzer. The bias voltage from the analyzer is connected through the sample holder, placed inside the vacuum chamber, to the detector (Fig. B.4).

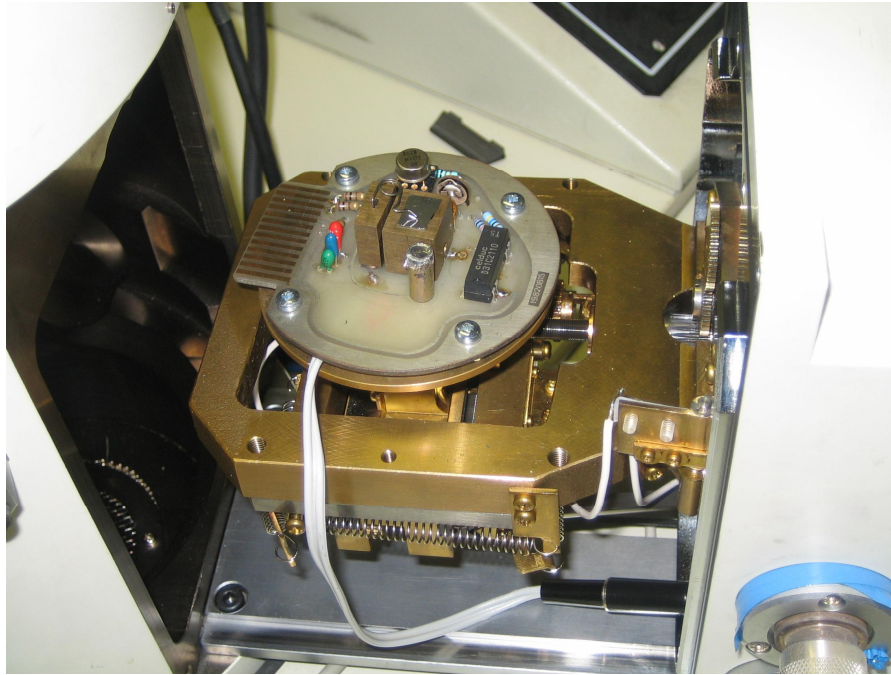


Figure B.4: Sampler holder inside the vacuum chamber.

In the vacuum chamber, a 5 keV electron beam is scanned over the examined surface of the biased detector at a speed of 2-5 $\mu\text{m/s}$ (Leinonen 2005b). The primary 5 keV electron beam generates secondary electrons at most a few nanometers below the examined surface. These electrons are pulled to a secondary electron detector (SEI=Secondary Electron Image), placed on the inside wall of the vacuum chamber, by a positive voltage V_{SEI} around this detector. The value of V_{SEI} is fixed to 10 kV in this microscope. The secondary electron detector works as a scintillator. It absorbs the electrons, which the primary beam has generated to the examined surface. These secondary electrons form the signal. The energy of secondary electrons is small, less than 50 eV, and thus even a small positive voltage on the sample can decrease the number of electrons arriving to the secondary electron detector and thereby cause a phenomenon called voltage-contrast (Leinonen 2005b). Then in the setup, the secondary electron signal is amplified and converted from analog to digital mode. This signal plus the horizontal and vertical timing signals of the SEM are read to a PC. The PC is used to display the images and waveforms, and to calculate potential distributions and electric fields.

References

- (Ahmed 2001) M. Ahmed, S. J. Watts, J. Matheson, A. Holmes-Siedle, *Deep-level transient spectroscopy studies of silicon detectors after 24 GeV proton irradiation and 1 MeV neutron irradiation*, Nuclear Instruments and Methods in Physics Research A 457 (2001), pp. 588–594.
- (ATLAS 2007) *ATLAS User's Manual – Device Simulation Software*, 2007, Silvaco International, www.silvaco.com.
- (Bleichner 1996) H. Bleichner, P. Jonsson, N. Keskitalo, E. Nordlander, *Temperature and injection dependence of the Shockley-Read-Hall lifetime in irradiated n-type silicon*, Journal of Applied Physics, vol. 79, no. 12, (1996), pp. 9142–9148.
- (Bruzzi 2006) M. Bruzzi et al., *Thermal donor generation in Czochralski silicon particle detectors*, Nuclear Instruments and Methods in Physics Research A 568 (2006), pp. 56–60.
- (Casse 2002) G. Casse et al., *First results on the charge collection properties of segmented detectors made with p-type bulk silicon*, Nuclear Instruments and Methods in Physics Research A 487 (2002), pp. 465–470.
- (Cavalleri 1971) G. Cavalleri et al., *Extension of Ramo's theorem as applied to induced charge in semiconductor detectors*, Nuclear Instruments and Methods 92 (1971), pp. 137–140.
- (CERN website) Available at www.cern.ch, About CERN, Particle Physics Today: The Standard Model, How does an accelerator work?, referred February, 2007.
- (Cottingham 2001) W.N. Cottingham, D.A. Greenwood, *An Introduction to Nuclear Physics*, Cambridge University Press, 2nd Edition, 2001, ISBN 0-521-65733-4.
- (Coughlan 2006) G.D. Coughlan, J.E. Dodd, B.M. Gripaios, *The Ideas of Particle Physics - An Introduction for Scientists*, Cambridge University Press, 3rd Edition, 2006, ISBN 0-521-67775-0.
- (Da Via 2003a) C. Da Via, S.J. Watts, *Can silicon operate beyond 10^{15} neutrons cm^{-2} ?*, Nuclear Instruments and Methods in Physics Research A 501 (2003), pp. 138–145.
- (Da Via 2003b) C. Da Via et al., *Advances in silicon detectors for particle tracking in extreme radiation environments*, Nuclear Instruments and Methods in Physics Research A 509 (2003), pp. 86–91.
- (Da Via 2006) C. Da Via, *3D active edge silicon sensor test results*, presented at the Sixth International “Hiroshima” Symposium on the Development and Application of Semiconductor Tracking Detectors, Carmel, California, September 11-15, 2006.
- (Eremin 1994) V. Eremin et al., *Determination of the Fermi level position for neutron irradiated high resistivity silicon detectors and materials using the transient charge technique (TChT)*, IEEE Transactions on Nuclear Science, vol. 41, (1994), pp. 1907–1912.

- (Eremin 1996) V. Eremin et al., *Development of transient current and charge techniques for the measurement of effective net concentration of ionized charges (N_{eff}) in the space charge region of p-n junction detectors*, Nuclear Instruments and Methods in Physics Research A 372 (1996), pp. 388–398.
- (Eremin 2002a) V. Eremin et al. *Effect of radiation induced deep level traps on Si detector performance*, Nuclear Instruments and Methods in Physics Research A 476 (2002), pp. 537–549.
- (Eremin 2002b) V. Eremin et al., *The origin of double peak electric field distribution in heavily irradiated silicon detectors*, Nuclear Instruments and Methods in Physics Research A 476 (2002), pp. 556–564.
- (Eränen 2004) S. Eränen, T. Virolainen, I. Luusua, J. Kalliopuska, K. Kurvinen, M. Eräluoto, J. Härkönen, K. Leinonen, T. Palviainen, M. Koski, *Silicon Semi 3D Radiation Detectors*, Nuclear Science Symposium Conference Record 2004, IEEE, Volume 2, 16–22 Oct. 2004, pp. 1231–1235.
- (Fleta 2007) C. Fleta et al., *Simulation and test of 3D silicon radiation detectors*, Nuclear Instruments and Methods in Physics Research A 579 (2007), pp. 642–647.
- (Fretwurst 2005) E. Fretwurst et al., *Recent advancements in the development of radiation hard semiconductor detectors for S-LHC*, Nuclear Instruments and Methods in Physics Research A 552 (2005), pp. 7–19.
- (Hall 1952) R.N. Hall, *Electron Hole Recombination in Germanium*, Physical Review 87 (1952), p. 387.
- (Hallen 1996) A. Hallen, N. Keskitalo, F. Masszi, V. Nagl, *Lifetime in proton irradiated silicon*, Journal of Applied Physics, vol. 79, no. 8, (1996), pp. 3906–3914.
- (Kenney 1999) C.J. Kenney, S. Parker, J. Segal, C. Storment, *Silicon Detectors with 3-D Electrode Arrays: Fabrication and Initial Test Results*, IEEE Transactions on Nuclear Science, vol. 46, no. 4, (1999), pp. 1224–1236.
- (Kenney 2001) C.J. Kenney, S. Parker, E. Walckiers, *Results from 3-D Silicon Sensors with Wall Electrodes: Near-Cell-Edge Sensitivity Measurements as a Preview of Active-Edge Sensors*, IEEE Transactions on Nuclear Science, vol. 48, no. 6, (2001), pp. 2405–2410.
- (Kenney 2006) C.J. Kenney et al., *Active-edge planar radiation sensors*, Nuclear Instruments and Methods in Physics Research A 565 (2006), pp. 272–277.
- (Knoll 2000) G.F. Knoll, *Radiation Detection and Measurement*, John Wiley & Sons, Inc., 3rd edition, 2000, ISBN 0-471-07338-5.
- (Kok 2006) A. Kok et al., *3D detectors – state of the art*, Nuclear Instruments and Methods in Physics Research A 560 (2006), pp. 127–130.

- (Leinonen 2005a) K. Leinonen, T. Palviainen, T. Tuuva, E. Tuovinen, J. Härkönen and P. Luukka, *Investigation of type inversion of n-bulk in 10 MeV proton-irradiated FZ silicon detectors using a scanning electron microscope*, Nuclear Instruments and Methods in Physics Research A 552 (2005), pp. 357–363.
- (Leinonen 2005b) K. Leinonen, *Investigation of voltages and electric fields in silicon radiation detectors using a scanning electron microscope*, Nuclear Instruments and Methods in Physics Research A 555 (2005), pp. 411–419.
- (Leinonen 2006) K. Leinonen, *Fabrication and characterization of silicon position sensitive particle detectors*, Diss., 2006, Acta Universitatis Lappeenrantaensis 235, Lappeenranta University of Technology.
- (LHC Design Report) LHC Design Report, Vol.1. Online document, referred February 14, 2007, available at https://edms.cern.ch/file/445831/5/Vol_1_Chapter_3.pdf.
- (Li 2002) Z. Li, *Novel prototype Si detector development and processing at BNL*, Nuclear Instruments and Methods in Physics Research A 478 (2002), pp. 303–310.
- (Li 2004) Z. Li et al., *Radiation Hardness of High Resistivity Magnetic Czochralski Silicon Detectors After Gamma, Neutron, and Proton Radiations*, IEEE Transactions on Nuclear Science, vol. 51, no. 4, (2004), pp. 1901–1908.
- (Li 2007) Z. Li et al., *Development, simulation and processing of new 3D Si detectors*, Nuclear Instruments and Methods in Physics Research A 583 (2007), pp. 139–148.
- (Lutz 1999) G. Lutz, *Semiconductor Radiation Detectors – Device Physics*, Springer-Verlag Berlin Heidelberg 1999, ISBN 3-540-64859-3.
- (Moll 1999) M. Moll, *Radiation Damage in Silicon Particle Detectors*, Ph. D. Thesis, University of Hamburg, Germany, 1999.
- (Moll 2005) M. Moll et al., *Development of radiation tolerant semiconductor detectors for the Super-LHC*, Nuclear Instruments and Methods in Physics Research A 546 (2005), pp. 99–107.
- (Noschis 2006) E. Noschis et al., *Final size planar edgeless silicon detectors for the TOTEM experiment*, Nuclear Instruments and Methods in Physics Research A 563 (2006), pp. 41–44.
- (Parker 1997) S.I. Parker, C.J. Kenney, J. Segal, *3D – A proposed new architecture for solid-state radiation detectors*, Nuclear Instruments and Methods in Physics Research A 395 (1997), pp. 328–343.
- (Passeri 2001) D. Passeri, P. Ciampolini, G. M. Bilei, F. Moscatelli, *Comprehensive Modeling of Bulk-Damage Effects in Silicon Radiation detectors*, IEEE Transactions on Nuclear Science, vol. 48, no. 5, (2001), pp. 1688–1693.
- (Pellegrini 2006) G. Pellegrini et al., *Edgeless detectors fabricated by dry etching process*, Nuclear Instruments and Methods in Physics Research A 563 (2006), pp. 70–73.

- (Pennicard 2007) D. Pennicard et al., *Simulation results from double-sided and standard 3D detectors*, presented at 10th RD50 workshop, 2007, Vilnius, Lithuania. Available at <http://rd50.web.cern.ch/rd50/>.
- (Perea Solano 2006) B. Perea Solano et al., *Edgeless silicon pad detectors*, Nuclear Instruments and Methods in Physics Research A 560 (2006), pp. 135–138.
- (Petasecca 2005a) M. Petasecca, F. Moscatelli, D. Passeri, G. U. Pignatelli, C. Scarpello, G. Caprai, *A Comprehensive Numerical Simulation of Heavily Irradiated p-type and n-type Silicon Detectors*, Nuclear Science Symposium Conference Record 2005, IEEE, 23–29 Oct. 2005, pp. 1490–1493.
- (Petasecca 2005b) M. Petasecca, F. Moscatelli, G. U. Pignatelli, *Analysis and simulation of charge collection efficiency in silicon thin detectors*, Nuclear Instruments and Methods in Physics Research A 546 (2005), pp. 291–295.
- (Petasecca 2006) M. Petasecca, F. Moscatelli, D. Passeri, G. U. Pignatelli, C. Scarpello, *Numerical simulation of radiation damage effects in p-type silicon detectors*, Nuclear Instruments and Methods in Physics Research A 563 (2006), pp. 192–195.
- (Piemonte 2005) C. Piemonte et al., *Development of 3D detectors featuring columnar electrodes of the same doping type*, Nuclear Instruments and Methods in Physics Research A 541 (2005), pp. 441–448.
- (Plummer 2000) J.D. Plummer, M.D. Deal, P.B. Griffin, *Silicon VLSI Technology. Fundamentals, Practice and Modeling*, Prentice Hall, 2000, ISBN 0-13-085037-3.
- (Ramo 1939) S. Ramo, *Currents Induced by Electron Motion*, Proceedings of the Institute of Radio Engineers, vol. 27, (1939), pp. 584–585.
- (Ranjan 2004) K. Ranjan et al., *High-voltage planar Si detectors for high-energy physics experiments: comparison between metal-overhang and field-limiting ring techniques*, Solid-State Electronics 48 (2004), pp. 1587–1595.
- (R&D Prop. 2002) R&D Proposal: *Development of radiation hard semiconductor devices for very high luminosity colliders*, LHCC 2002-003 / P6, February 2002.
- (RD50 2003) RD50 Status Report 2002/2003, CERN-LHCC-2003-058.
- (RD50 2004) RD50 Status Report 2004, CERN-LHCC-2004-031.
- (Ruggiero 2005) G. Ruggiero et al., *Planar Edgeless Silicon Detectors for the TOTEM Experiment*, IEEE Transactions on Nuclear Science, vol. 52, no. 5, (2005), pp. 1899-1902.
- (Shockley 1938) W. Shockley, *Currents to Conductors Induced by a Moving Point Charge*, Journal of Applied Physics, vol. 9, (1938), pp. 635-636.
- (Shockley 1952) W. Shockley, W.T. Read, *Statistics of the Recombination of Holes and Electrons*, Physical Review 87 (1952), pp. 835-842.

- (Sinkkonen 1996) J. Sinkkonen, *Puolijohdeteknologian perusteet*, Reports in Electron Physics 1996/11, Helsinki University of Technology, ISBN 951-22-3242-1.
- (Sze 1981) S.M. Sze, *Physics of Semiconductor Devices*, 2nd edition, John Wiley & Sons, Inc., 1981, ISBN 0-471-05661-8.
- (Tuovinen 2006) E. Tuovinen et al., *Czochralski silicon detectors irradiated with 24 GeV/c and 10 MeV protons*, Nuclear Instruments and Methods in Physics Research A 568 (2006), pp. 83–88.
- (Verbitskaya 2007) E. Verbitskaya, V. Eremin, Z. Li, J. Härkönen, M. Bruzzi, *Concept of Double Peak electric field distribution in the development of radiation hard silicon detectors*, Nuclear Instruments and Methods in Physics Research A 583 (2007), pp. 77-86.
- (Wunstorf 1997) R. Wunstorf, *Radiation Hardness of Silicon Detectors: Current Status*, IEEE Transactions on Nuclear Science, vol. 44, no. 3, (1997), pp. 806–814.
- (Wunstorf 1992) R. Wunstorf, *Systematische Untersuchungen zur Strahlenresistenz von Silizium Detektoren für die Verwendung in Hochenergiephysik Experimenten*, Ph. D. thesis, University of Hamburg, Hamburg, Germany (1992).

Publication I

S. Eränen, T. Virolainen, I. Luusua, J. Kalliopuska, K. Kurvinen, M. Eräluoto, J. Härkönen, K. Leinonen, T. Palviainen, M. Koski

“Silicon Semi 3D Radiation Detectors”

© [2004] IEEE. Reprinted, with permission, from Nuclear Science Symposium Conference Record 2004, Volume 2, 16–22 Oct. 2004, pp. 1231–1235 (CD-ROM).

Silicon Semi 3D Radiation Detectors

S. Eränen, T. Virolainen, I. Luusua, J. Kalliopuska, K. Kurvinen, M. Eräluoto, J. Härkönen,
K. Leinonen, M. Palviainen and M. Koski

Abstract—The paper describes the first results on the behavior of semi three dimensional (3D) silicon radiation detectors. As compared to the normal 3D detectors with the n- and p-type vertical doping profiles, the present structure employs the p-type profiles, only. The report covers the proposed new structure, fabrication sequence, the electrical characteristics like the capacitance, leakage current, breakdown voltage, x-ray response for the Am-source. These results are reported for the high resistivity Cz and FZ starting material. The measured electrical characteristics are compared with the 3D simulation results obtained with the ISE TCAD software. In addition, the 3D mixed mode transient simulations are employed in order to learn about the signal charge collection capabilities of the new structure.

I. INTRODUCTION

SINCE the pioneering work of J. Kemmer at the beginning of eighties the planar silicon detectors have become real work horses in the field of the radiation detecting devices [1]. These devices have a wide range of applications including e.g. the instrumentation using devices, that are sensitive to light and/or soft x-rays, high energy physics, radiation and other safety aspects, non-destructive testing and inspection, space applications and imaging, where the various medical applications are currently becoming very important. The success of the planar silicon detector technology is not very surprising, since it has been able to take the benefit of some parts the enormous growth and development of the silicon integrated circuit technology. This development is roadmapped in the ITRS [2] and it is believed to continue at least until the year 2018. In particular, several innovations for the rapidly growing digital market have been directly utilised

for the silicon detector business, as well. This is especially true for the process equipment, chemical and process purity, material and process development and wafer handling systems. In addition, the silicon radiation detector community has been able to overcome the inherent weaknesses of the basic silicon material like the insensitivity to the gammas and hard x-rays. This has been accomplished with the ingenious radiation conversion methods like e.g. the scintillator technology.

In the mid nineties new architectures of silicon radiation detectors employing three dimensional (3D) arrays of electrodes, that penetrate into the detector bulk, were proposed [3,4]. The fabrication of these silicon structures heavily employ the methods of the silicon micromechanics. From the user point of view the interest in the 3D detectors comes from several facts: the devices can be fully depleted at low bias voltages, speed of charge collection is high, good spatial resolution can be obtained, the devices exhibit high radiation tolerance, the technology permits also the fabrication of detectors with narrow edge dead regions and, finally, the detectors can be fabricated on the large area CZ-silicon substrates.

This paper describes the fabrication and the first results on the semi 3D radiation detector structure fabricated on silicon. Usually, the 3D detectors have vertical p- and n-type vertical doping profiles or pillars through the wafer resulting in the vertical depletion of the structure. In the present case the vertical p-type doping pillars are employed, only, and the vertical depth of the doping profiles is left as a variable. The backside or the n-type contact of the structure is a blank implantation, similar to the normal planar strip or pixel silicon detectors. The electrical results include the leakage currents, breakdown voltages, reverse biased capacitance values and radiation measurement results with the Am-source. In addition, the comparison with the FZ and CZ wafer materials and the radiation hardness results will be presented. We also present the comparison between the measured leakage current and capacitance values with the true 3D simulation values, that were obtained using the ISE TCAD simulation tool. Finally, the same simulation program is employed in the transient mode including the external bias circuit (voltage source and resistor)

Manuscript received October 20, 2004.

S. Eränen, T. Virolainen and I. Luusua are with VTT Information Technology / Microelectronics, PO Box 1208, FIN-02044 VTT, Finland. (e-mail: simo.eranen@vtt.fi)

J. Kalliopuska, K. Kurvinen and M. Eräluoto are with Helsinki Institute of Physics, PO Box 64, FIN-00014 Helsinki University, Finland

J. Härkönen is with Helsinki Institute of Physics, CERN/EP, 1211 Geneva, Switzerland

K. Leinonen, M. Palviainen, M. Koski are with Lappeenranta University of Technology, PO Box 20, FIN-53851 Lappeenranta, Finland

in order to predict signal charge collection performance of the proposed detector structure.

II. STRUCTURE AND FABRICATION

Fig.1 describes the basic structure of the proposed semi 3D structure. The structure has the p-type vertical doping profiles, the diameter of which is ten or twenty microns. In the fabricated detectors the depth of the p-type is dependent on the diameter. For the twenty micron diameter the depth is 200 μm and for the ten microns diameter the corresponding value is 150 μm . The n-type electrode of the detector is a uniform n-type doping on the backside of the device. The pitch between the p-type electrode is a variable. In the current structure we had 100 and 200 μm . The present devices were not optimized for any particular application, but the work merely presents a technology demonstration. In addition to the p-type doping pillar the front side of the detector has a p-type implantation around the pillar in order to tune the electric field inside the device. For the 100 μm pitch the widths of these square implants were 40 and 90 μm , while for the 200 μm pitch the widths are 100 and 190 μm . Finally, each pixel of the detector had a square contact window with the width of 30 μm .

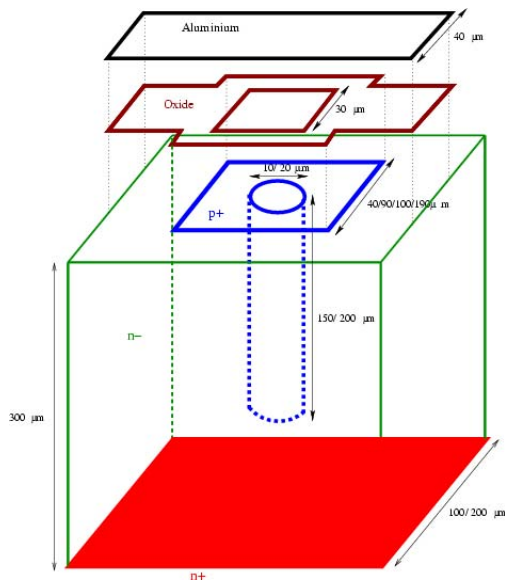


Fig. 1. Basic structure of the semi 3D detector

For the electrical testing the pixels were connected as strips with the Al-lines. The fabricated test structures covered 5x5, 10x10 and 100x100 pixel detectors. For the 200 microns pitch this means, that the largest test device had the size of 2x2 cm^2 .

The semi 3D detectors were fabricated on the n-type high resistivity FZ-silicon wafers with the resistivity above 6 $\text{k}\Omega\text{cm}$. The wafer thickness is 300 microns and the crystal orientation $\langle 111 \rangle$. For comparison a few CZ-silicon wafers with the resistivity of 1 $\text{k}\Omega\text{cm}$ and $\langle 100 \rangle$ orientation were included in the process.

The fabrication starts with the growth of the field oxide for the passivation of the surface. This is followed by the first mask, that defines the hole positions of the vertical p-type doping pillars. The holes are first opened into the field oxide and then the deep ICP silicon etching is employed in order to define the vertical electrodes. In our case the silicon etching depth varied between 150 and 200 microns depending on the hole diameter. In the next step the holes were filled using the in-situ doped p-type LPCVD poly silicon. In order to fill the hole with the diameter of 20 microns the layer thickness of at least ten microns is required. After the hole filling the extra layer of polysilicon on the wafer surface must be removed either by etching or by the CMP planarization. The same technique of deep etching and filling can also be used for the formation of the so-called active edge structures. Further the oxide is opened for the p-type surface implant, the meaning of which is to reduce the effect of the oxide charge on the surface and ease the depletion of the total detector volume. The rest of process contains standard steps for the backside, contact windows and metal patterns.

III. RESULTS

A. Electrical results

Fig. 2a and Fig. 2b show the measured dark, reverse leakage currents for the selected structures from the zero bias up to 100 V at 25 $^{\circ}\text{C}$ on the FZ silicon wafers. The title on the figure denotes the selection of the layout parameters of the measured structure. Thus, in Fig. 2a the diameter of the vertical doping pillar is 20 μm , the pitch between the adjacent pixels 200 μm and the width of the surface implant 100 μm . Correspondingly, in Fig. 2b the diameter is 10 μm , the pitch 100 μm and the width of the surface implant 40 μm .

As mentioned above, the individual pixels are connected as strips for the electrical testing. Thus each curve in Figs.2 represents the parallel connection of a number of pixels. The legend on the right explains the type of the test structure. For Fig. 2a 1M5 is a 100x100 matrix and 1M1 is a 10x10 matrix. Thus, the upper curve is the result of one hundred pixels in parallel and the lower curve is the result of ten pixels in parallel. In the same fashion in Fig. 2b M16 and M12 are 100x100 matrixes and thus the two upper curves display the result of one hundred pixels in parallel. M21 is a 10x10 matrix.

As a general behavior the 100 pixels strips seem give currents, that are about ten times larger than those of the ten pixels strips. At 100 V the leakage current per pixel is about a few pico amperes. There are variations from one layout structure to another, but variations also exist between similar structures. So

further work is needed in order to make decisions about the recommended layout parameters.

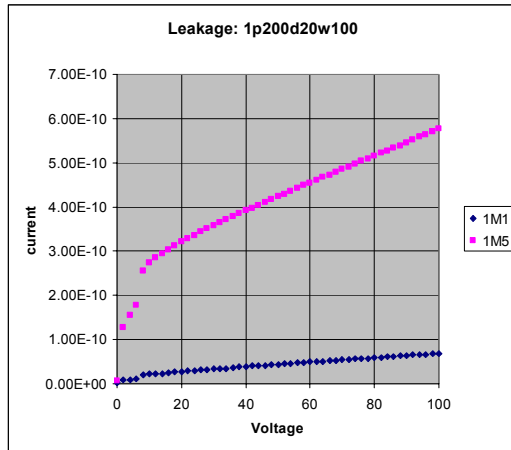


Fig. 2a. Leakage current of a selected pixel strip on FZ Si (see text)

wafers are shown, it is clear, that the leakage current on the FZ silicon is about seven times smaller than on the CZ silicon.

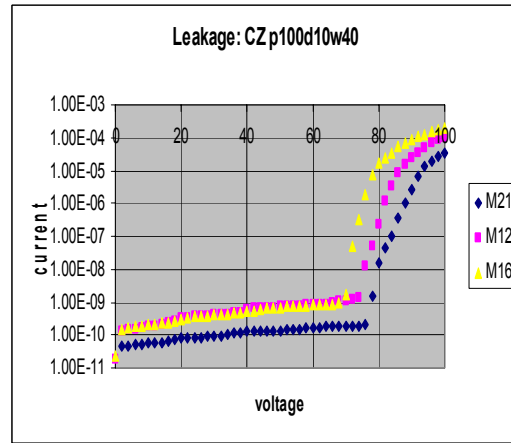


Fig. 3. Leakage current of a selected pixel strip on CZ Si (see text)

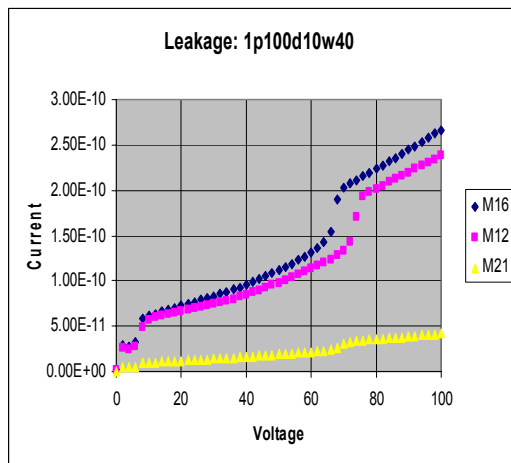


Fig. 2b. Leakage current of a selected pixel strip on FZ Si (see text)

In Fig. 2b. the curves display repeatable kinks at certain reverse voltages. The reasons for these are not understood at present (see simulations).

As to the CZ wafers one example of the leakage curves is shown in Fig. 3. Here M16 and M12 are the 100x100 matrixes and M21 is again the 10x10 matrix. At fixed voltages the leakage currents on the CZ wafers are larger than the currents on the FZ wafers. If we compare e.g. Figs. 2b and 3, where the results measured for the equivalent structures on the FZ and CZ

The other prominent feature in Fig.3. is the the clear avalanche breakdown, that takes place between 60 and 80 volts. On the FZ wafers the breakdown in general occurs above 140 V for the pixel strips. In some cases this value can even exceed 200 V, which was the test limit in these experiments. Further, on these wafers the the breakdown of the circular diodes (surface implant) occurs above 200 V without an exception. On the other hand for the CZ pixel strips the breakdown is always between 64 and 90 V, whereas the circular CZ diodes display the breakdown characteristics between 120 and 140 volts.

The reverse biased capacitance curves as a function of the bias voltage were measured on the 100 pixel strips using a 10 kHz probe signal with the amplitude of 50 mV. Some results are shown in Fig.4. for various structures with the pixel pitch of 100 micrometers on the FZ silicon. Here the level of the capacitance is dependent on the choice of the layout parameters, but the most prominent feature of Fig.4. is the saturation of the capacitance values for each curve above 30 V. This gives a hint, that the structures with the pixel pitch of 100 micrometers become fully depleted already at 30 volts. The same behavior is not seen with the pixel pitch of 200 micrometers on the FZ material or with any structure on the CZ silicon below 34 V, which was the bias test limit of the capacitance measurements. At the saturation the capacitance per pixel seems to vary between 40 and 90 fF/pixel. However, this value greatly overestimates the actual pixel capacitance, since the measured value also includes the parallel (over depleted) MOS capacitance, that is caused by the aluminum line, which connects the individual pixels within one strip. Separate measurement were done on the MOS test structures in

order to ascertain, that the MOS capacitances also remain flat with the chosen probe parameters in the voltage region, where saturation of the total strip capacitance is observed.

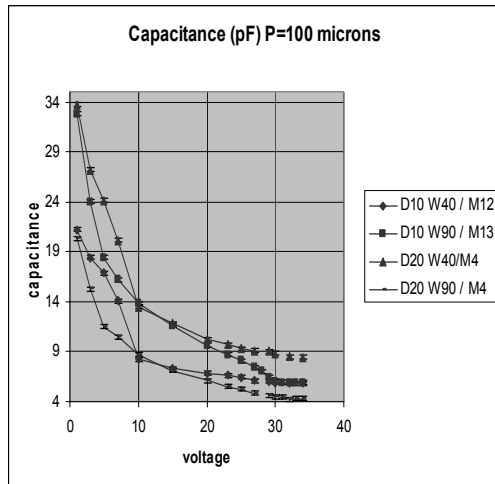


Fig. 4. Capacitance curves for selected structures with pixel pitch of 100 micrometers on FZ silicon (see text)

The x-ray response of the present structure was tested with an Am-source. The test were done on a 4 cm² detector with the pixel pitch of 200 μm, surface implant width of 100 μm and the electrode diameter of 20 μm. For the test a few strips at the centre of the device were biased and strip connected with the amplifier. The structure was irradiated from the front the front surface and the bias was 24 V. So the detector was fully depleted. The result is shown in Fig.5. The FWHM of the main peak is about 7.7 %.

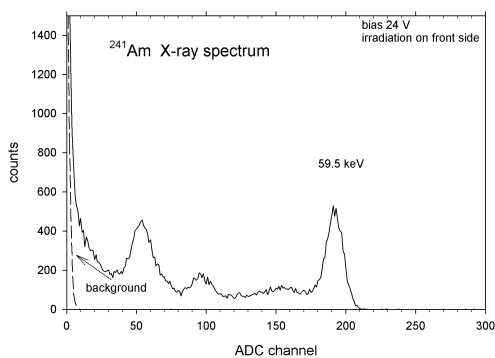


Fig. 5. Am-spectrum of 4 sqcm detector on FZ Si (see text)

For the radiation hardness testing four CZ and four FZ samples were prepared. Each sample had the area of 1 cm² and the layout parameters were pitch 100 μm, surface implant width 40 μm and hole diameter 10 μm. The samples were irradiated at Cern using 24 GeV/c protons at the fluences of 1.4e15, 4.0e15, 6.0e15 and 1.0e16 cm⁻². There was no cooling or bias during the irradiation.

TABLE I
DEPLETION OF CZ SILICON WITH INCREASING PROTON DOSES

Dose	CZ	
	Depl. Voltage V _d (V)	Current @ V _d
0		
1.4e15	60	26
4.0e15	87	29
6.0e15	95	75
1.0e16	NA	NA

TABLE II
DEPLETION OF FZ SILICON WITH INCREASING PROTON DOSES

Dose	FZ	
	Depl. Voltage V _d (V)	Current @ V _d
0	30	0.0005
1.4e15	82	24
4.0e15	86	30
6.0e15	90	70
1.0e16	NA	NA

TABLE I and II summarize the depletion voltages and the leakage currents at the depletion voltages for the test samples as a function of the proton dose on the CZ and FZ material. Here the measurement setup was different from the one, that was used for the leakage currents and capacitances reported earlier. The depletion voltages of the samples were not determined before the irradiation and the zero dose values of the FZ material have been taken from the different setup and samples. After the dose of 1e16 cm⁻² the samples were heavily damaged and no reliable data could be obtained. The essential point here is, that there is no essential difference between the FZ and CZ material. The depletion voltage of the detectors remain below 100 V even at the dose of 6e15 cm⁻². The leakage currents at the depletion voltage increase with the proton dose – but not linearly.

B. Simulations

The performance of the new semi 3D structure was simulated using a true 3D tool ISE TCAD. First of all the leakage current of one pixel was compared with measured data

for a chosen layout. The simulations can very well predict the magnitude of the leakage current, but cannot reproduce the kinks in Fig. 2b. This leads to the conclusion, that the kinks could be caused by the measurement setup, where one strip is biased, only.

The capacitance simulations give the result, that the pixel capacitance saturates already at very low voltages and the saturation capacitance per pixel is around 10 fF. This shows, that the measured values in Fig.4. are dominated by the MOS contribution.

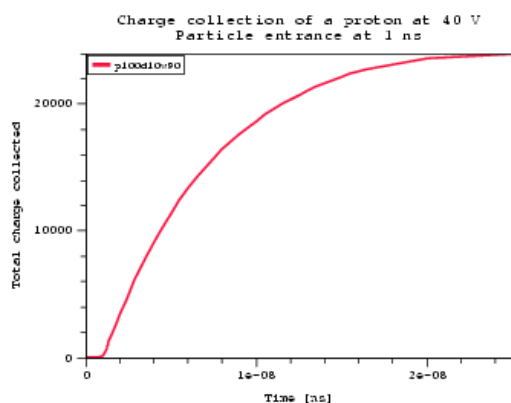


Fig. 6. Integral of signal caused by proton (see text)

The charge collection behavior of the semi 3D structures were studied using the transient mixed mode option of ISE TCAD. We studied the case, where a proton hits the center of a square cell formed by four p-type doping pillars with the pitch of 100 micrometers. Fig.6. shows the integral of the signal current caused by the proton. In the time scale the hit takes place at 1 ns and the voltage source in the detector circuit has the output voltage of 40 V. In addition the circuit has a series resistor of 100 ohms. The center of the square cell is an area of low electrical fields and thus the simulation represents the

worst case scenario for the proposed structure. The result in Fig.6. shows, that the signal charge will be collected in less than 20 ns. It is well known, that the dependence of the charge collection time on the hit location in the 3D detector cell and on the bias voltage are general properties of the 3D structures. The charge collection at high bias and high field points can be very fast i.e. in the order of a few nanoseconds. On the other hand every 3D structure exhibit low field regions, where the charge collection time becomes much slower. The present simulation result indicate, that the charge collection capability of the semi 3D structure is comparable to the other 3D detectors.

IV. CONCLUSION

A new 3D detector structure was proposed. The current structure employs one type (p-type) of vertical doping profiles, only. This feature makes the fabrication scheme of these devices much simpler than the corresponding process flows of the conventional 3D detectors. This simplification has led to an easy demonstration of large area pixel detectors. Moreover, the semi 3D detectors should be well compatible with the current packaging processes like the flip chip bonding.

The fabricated demonstrators were not optimized for any applications. However, these test structures indicate, that the semi 3D pixel structures have low leakage currents, low pixel capacitances and good radiation hardness. Moreover, these structures can also be fabricated on the CZ silicon as well as on the traditional FZ detector starting material.

The true 3D simulations can give a good insight into the detector physics resulting in e.g. the true pixel capacitance values. In addition, the transient simulation indicate, that the proposed semi 3D devices have charge collection properties, that are comparable to other 3D detector structures.

V. REFERENCES

- [1] J. Kemmer et al, NIM 169, 1980, p. 499
- [2] International Technology Roadmap for Semiconductors 2003, <http://itrs.public.net>
- [3] S. I. Parker et al, NIM A395 .
- [4] C. Kenney et al, IEEE Trans. Nuc, Sci Vol. 46, no. 1, p.1, Jan. 1999

Publication II

T. Palviainen, K. Leinonen, T. Tuuva, S. Eränen, J. Härkönen, P. Luukka, E. Tuovinen

“Investigation of voltages and electric fields in silicon semi 3D radiation detectors using Silvaco / ATLAS simulation tool and a scanning electron microscope”

© [2005] IEEE. Reprinted, with permission, from Nuclear Science Symposium Conference Record 2005, 23–29 Oct. 2005, pp. 1379–1382, (CD-ROM).

Investigation of Voltages and Electric Fields in Silicon Semi 3D Radiation Detectors Using Silvaco / ATLAS Simulation Tool and a Scanning Electron Microscope

Tanja Palviainen, Kari Leinonen, Tuure Tuuva, Simo Eränen, Jaakko Härkönen, Panja Luukka, and Esa Tuovinen

Abstract—The structure of silicon semi three-dimensional radiation detector is simulated on purpose to find out its electrical characteristics such as the depletion voltage and electric field. Two-dimensional simulation results are compared to voltage and electric field measurements done by a scanning electron microscope.

I. INTRODUCTION

THE new architecture for solid-state radiation detectors using a three-dimensional array of electrodes that penetrate into the detector bulk were proposed by S.I. Parker, C.J. Kenney and J. Segal in the mid 90's [1]. 3D detectors have many advantages: the devices can be fully depleted at low bias voltages, the speed of the charge collection is high, and the collection distances are about one order of magnitude less than those of planar technology strip and pixel detectors with electrodes limited to the detector surface. Also the 3D detector devices exhibit high radiation tolerance, so the ability of the silicon detectors to operate after irradiation is increased.

Silicon semi 3D detectors have vertical p-type doping profiles. The vertical depth of the doping profiles is left as a variable [2]. The objective of this article is to present simulation results of silicon semi 3D radiation detector structure done by Silvaco ATLAS device simulation software [3] and show electric field measurement results done by a scanning electron microscope (SEM).

II. SILICON SEMI 3D RADIATION DETECTORS

A. Structure

The basic semi 3D detector structure is shown in Fig. 1 [2]. The structure has the p-type vertical doping profile. The depth of the p-type pillar is dependent on the diameter of the pillar.

Simulations are done using following dimensions: the diameter of the p-type pillar is $10\mu\text{m}$, the depth of the doping profile is $150\mu\text{m}$ and the pitch between the p-type electrodes is $100\mu\text{m}$. In addition to the p-type doping pillar, the front side of the detector has a p-type implantation around the pillar. The dimensions of this implantation used in simulations are $40\mu\text{m}$ and $90\mu\text{m}$. There is also a square contact window in each pixel of the detector and the pixels are connected as strips with the aluminum lines. The backside of the structure is a uniform implantation similar to the planar detectors. The backside of the device is the n-type electrode. The top of the layout is shown in Fig. 2.

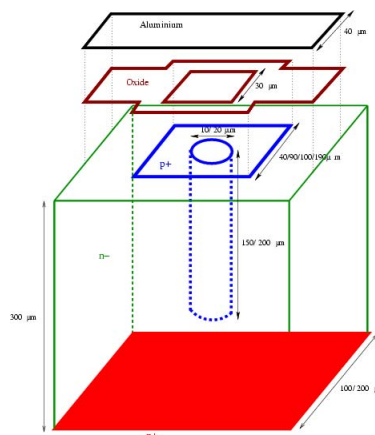


Fig. 1. The basic structure of the semi 3D detector [1].

The top of the layout and the cross-section of the semi 3D detector structure are shown in Fig. 2-3. Figures are taken using SEM. The p-type pillars can be seen in Fig. 3.

Manuscript received November 11, 2005.

Tanja Palviainen, Kari Leinonen and Tuure Tuuva are with the Department of Electrical Engineering, Lappeenranta University of Technology, P.O. Box 20, FIN-53851 Lappeenranta, Finland (e-mail: tanja.palviainen@lut.fi).

Simo Eränen is with the VTT Information Technology / Microelectronics, P.O. Box 1208, FIN-02044 VTT, Finland (e-mail: simo.eranen@vtt.fi).

Jaakko Härkönen, Panja Luukka and Esa Tuovinen are with the Helsinki Institute of Physics, P.O. Box 64, FIN-00014 Helsinki University, Finland (e-mail: jaakko.haerkoenen@cern.ch).

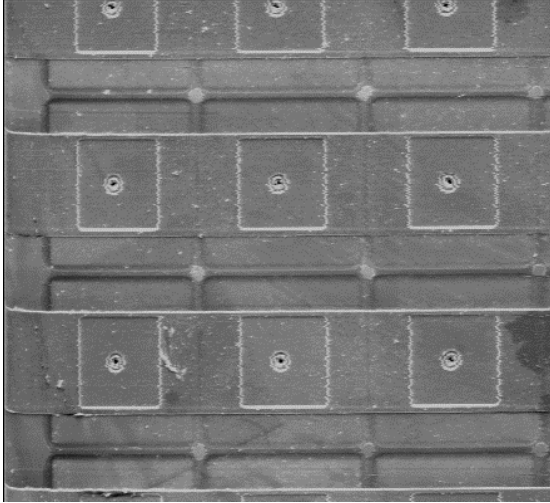


Fig. 2. The top view of the semi 3D detector using SEM.

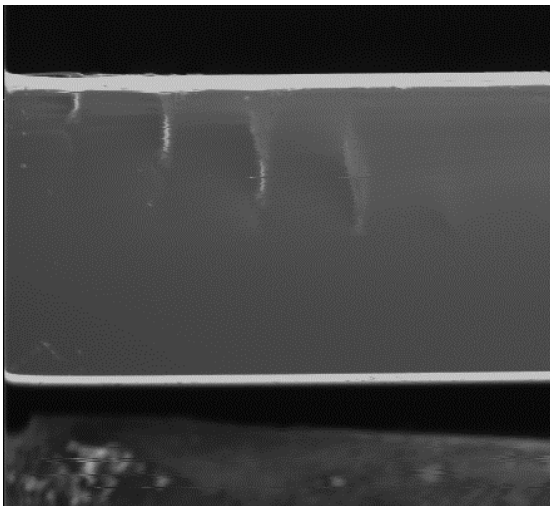


Fig. 3. The cross-section of the semi 3D detector structure using SEM.

B. Simulation Results

Simulations and SEM measurements are done using 0 V, -10 V, -40 V and -80 V. The potential figures with varied voltages of the silicon semi 3D radiation detector structure are shown in simulation results (Fig. 4-7). In the simulated figures there are shown three p-type pillars penetrating to the detector bulk. P-type pillars are anodes and the cathode is placed on the backside of the detector. The negative bias voltages are applied to the anode while the cathode remains at zero. The colour scheme describes the potential distribution inside the

detector structure. The color scheme in simulation figures and SEM measurements is continuous rainbow spectrum where the most positive voltage is red and the most negative voltage is bright magenta.

C. SEM Measurements

Scanning electron microscope is used to investigate the properties of the silicon semi 3D radiation detectors. Usually the main methods used for this are: capacitance-voltage (CV) measurements and transient current technique (TCT). Both of these methods are macroscopic and secondary. Instead, scanning electron microscope provides an accurate microscopic means of imaging and measuring the desired quantities more directly from the sample as a function of position. The scanning electron microscope method is probably the only way to measure and view the potential distribution inside a semiconductor device directly [4].

Fig. 8 shows the SEM measurement when there is no voltage connected. The potential differences are only seen between p-type pillars in the structure. When there is 10 V connected in Fig. 9, the potential differences begin to show between the end of the pillars and the backside of the structure. The potential spreads downwards.

When 40 V is connected also the potential of the front side starts to spread between p-type pillars (Fig. 10). And in the Fig. 11 where is 80 V applied, the space between pillars is almost in the same potential. The simulation results show the same phenomenon.

When SEM measurements are compared to simulation results it can be seen that there is a correspondence. Both results show the properties of semi 3D detector: the semi 3D detector structure is fully depleted at low voltages, and with the high bias the electric field is mainly formed between the end of the pillars and the backside.

There are also facts, which may cause differences between simulation results and SEM measurements. First of all, the simulation results are ideal and in simulations there has not taken into account oxide charge or surface states, which affect to the depleted area. Second, the SEM photographs differ from simulation results because the relation between contrast and voltage is not linear all the time. With small voltages (under -20 V) the relation between contrast and voltage is close to linear but with bigger voltages the change of the potential does not affect to the change of the contrast linearly [4].

The SEM photographs of the silicon semi 3D radiation detector structure are shown in Fig. 8.-11.

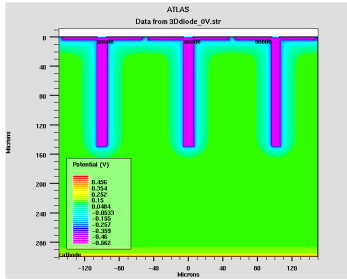


Fig. 4. Potential of semi 3D detector structure at 0V of bias.

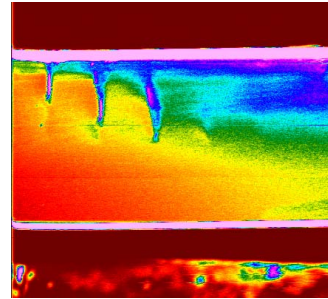


Fig. 8. SEM measurement of the semi 3D structure using 0V.

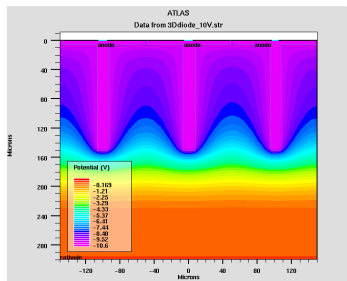


Fig. 5. Potential of semi 3D detector structure at -10V of bias.

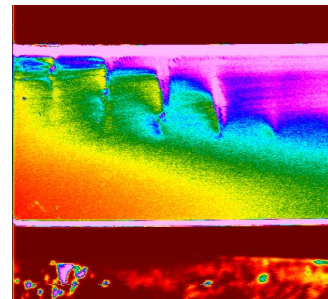


Fig. 9. SEM measurement of the semi 3D structure using -10V.

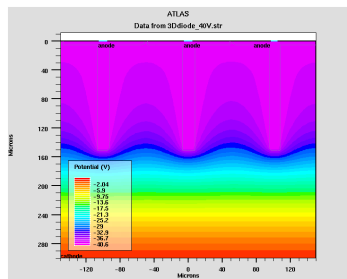


Fig. 6. Potential of semi 3D detector structure at -40V of bias.

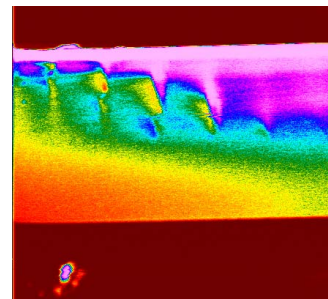


Fig. 10. SEM measurement of the semi 3D structure using -40V.

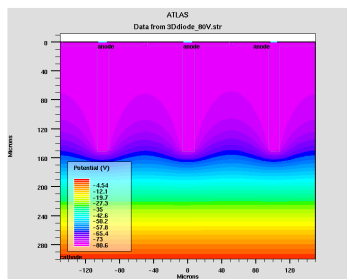


Fig. 7. Potential of semi 3D detector structure at -80V of bias.

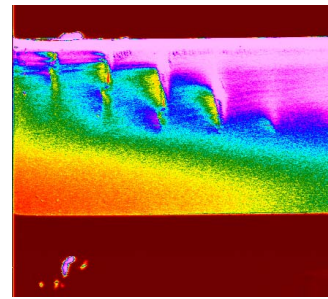


Fig. 11. SEM measurement of the semi 3D structure using -80V.

III. CONCLUSION

Bias voltage used in simulations varied between 0 V and -80 V. Potential figures show that the semi 3D detector structure is fully depleted at low voltages (between -10 V and -40 V in these simulations). Because of the structure of the semi 3D detector, the charge-collecting field is only below the pillars where the electric field has formed.

SEM measurements verify the simulation results. However, simulation results are ideal, for instance no oxide charge or surface states were included, which affects the spreading of the depletion layer.

REFERENCES

- [1] S.I. Parker et al., Nuclear Instruments and Methods in Physics Research A 395 (1997) 328-343
- [2] S. Eränen, T. Virolainen, I. Luusua, J. Kalliopuska, K. Kurvinen, M. Eräluoto, J. Härkönen, K. Leinonen, T. Palviainen and M.Koski, Silicon Semi 3D Radiation Detectors, IEEE Nuclear Science Symposium (NSS), Rome, October 16-24, 2004.
- [3] Silvaco International, ATLAS (vol I & II) User's Manual, (<http://www.silvaco.com/>)
- [4] K. Leinonen, Investigation of Voltages and Electric Fields in Silicon Radiation Detectors using a Scanning Electron Microscope, submitted to NIM A, February 2005.

Publication III

K. Leinonen, T. Palviainen, T. Tuuva, E. Tuovinen, J. Härkönen and P. Luukka

“Investigation of type inversion of n-bulk in 10 MeV proton-irradiated FZ silicon detectors using a scanning electron microscope”

Reprinted from Nuclear Instruments and Methods in Physics Research A 552, pp. 357–363, Copyright (2005), with permission from Elsevier.



ELSEVIER

Available online at www.sciencedirect.com

SCIENCE @ DIRECT®

Nuclear Instruments and Methods in Physics Research A 552 (2005) 357–363

NUCLEAR
INSTRUMENTS
& METHODS
IN PHYSICS
RESEARCH
Section A

www.elsevier.com/locate/nima

Investigation of type inversion of n-bulk in 10 MeV proton-irradiated FZ silicon detectors using a scanning electron microscope

Kari Leinonen^{a,*}, Tanja Palviainen^a, Tuure Tuuva^a, Esa Tuovinen^b,
Jaakko Härkönen^b, Panja Luukka^b

^aLappeenranta University of Technology, P.O. Box 20, Lappeenranta, FIN-53851, Finland

^bHelsinki Institute of Physics, P.O. Box 64, Helsinki University, FIN-00014, Finland

Received 28 April 2005; accepted 5 July 2005

Available online 26 July 2005

Abstract

Based on the results of capacitance–voltage measurements and transient current technique, it was earlier deduced that the n-type bulk of float zone silicon radiation detectors changes type in heavy irradiation. This paper describes the results of measuring the voltages and electric fields with a scanning electron microscope using the voltage–contrast effect, inside radiation detectors that were irradiated with 10 MeV protons with several fluences. The results confirm the earlier observations and give more accuracy to the electric field measurements.

© 2005 Elsevier B.V. All rights reserved.

PACS: 29.40; 29.40.W; 61.16.B; 84.37

Keywords: Radiation detector; Silicon; Radiation tolerance; Type inversion; Voltage; Electric field

1. Introduction

Silicon detectors used in high-energy physics experiments are exposed to a very hostile radiation environment. An upgrade of the CERN LHC (Large Hadron Collider) luminosity up to $10^{35} \text{ cm}^{-2} \text{ s}^{-1}$ (Super-LHC) has been proposed.

This would raise the fluences of fast hadrons up to 10^{16} cm^{-2} , well beyond the operational limits of present silicon detectors [1]. Particle radiation causes irreversible crystallographic defects in the silicon material. Defects generated by radiation cause, e.g., variation of the effective doping concentration N_{eff} and consequently of the full-depletion voltage V_{dep} . The microscopic mechanisms related to the N_{eff} variation in n-type float zone (FZ) silicon are the donor removal and

*Corresponding author.

E-mail address: Kari.Leinonen@lut.fi (K. Leinonen).

generation and the deep acceptor generation. By increasing the fluence, N_{eff} decreases up to semiconductor-type inversion, i.e. the density of the radiation-induced deep acceptors causes N_{eff} to become negative [2].

Type inversion has been investigated with a few methods: capacitance–voltage (CV) measurements which yield the depletion voltage and the effective doping concentration, transient current technique (TCT) which gives information about the position of the electric field maximum inside the detector through observing the shape and the delay of a current pulse after generating carriers near one surface of the detector with a short laser pulse [3,4], optical beam-induced current (OBIC) [5] and measuring the surface potential with a mechanical probe from a cleaved sample [5]. The electric field profile has also been calculated based on the material data got from various macroscopic measurements [6].

The voltage–contrast phenomenon of the scanning electron microscope can be used to measure electric potentials and fields in a biased radiation detector with an accurate non-touching microscopic probe [7]. In this paper, this method is applied to irradiated pad detectors to get more accurate information about semiconductor-type inversion.

2. Sample preparation

One hundred millimeter diameter n-type 300 μm thick (100)-oriented FZ silicon wafers with a nominal resistivity of 1200 Ωcm , manufactured by Wacker, were used in this study. Using a very simple five-mask-level process, $\text{p}^+/\text{n}^-/\text{n}^+$ diodes were processed at the Microelectronics Center of Helsinki University of Technology. The p^+ -implanted area of the diodes is 5 mm \times 5 mm. One 100 μm wide guard ring surrounds the active area (the pad). This wide guard ring is surrounded by a multi-guard ring structure of 16 rings, each with a width of 16 μm . The detailed device structure is presented in Ref. [1]. The processing is described more in detail in Ref. [8]. The full-depletion voltage, extracted from capacitance–voltage measurements, is about

260 V. The leakage current at full-depletion was less than 5 nA for all diodes. Randomly selected diodes were measured above the full-depletion voltage, up to 1000 V, without observing breakdown [9].

The samples were irradiated with 10 MeV protons at the Jyväskylä University Accelerator Laboratory. Diodes were first glued with photoresist on ceramic supports so that four diodes were always placed on one support. Samples were placed inside a vacuum chamber at the end of RADiation Effects Facility (RADEF) beam line [10]. The intensity of the proton beam was typically 2 nA/cm². Samples were kept at -10°C during the irradiation.

After the irradiations with 10 MeV protons, the samples were kept refrigerated below room temperature. Full-depletion voltages (V_{dep}) and effective doping concentrations (N_{eff}) were resolved by capacitance–voltage (CV) measurements at 10 kHz in parallel mode. The results are presented in Fig. 1. V_{dep} values have been normalized to 300 μm thickness.

Three samples were selected for scanning electron microscope tests: radiation fluences 0 (no irradiation) and 2.53E13 and 1.50E14 p/cm². The latter two correspond to 1 MeV equivalent neutron fluence of 1.09E14 and 6.45E14 cm⁻². In the first detector, we expect to find a normal pn-junction near the front side (p^+ -side) of the detector. The third detector is supposed to have

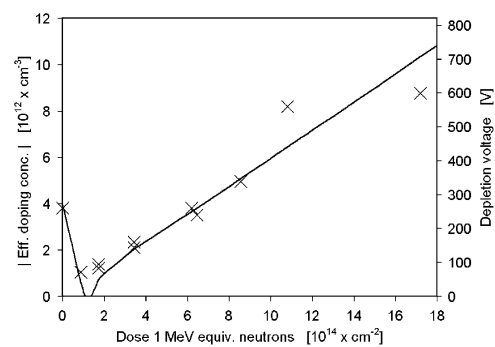


Fig. 1. Evolution of N_{eff} in FZ-Si pad detectors irradiated with 10 MeV protons.

its pn-junction near the back side (n^+ -side) because the fluence is clearly above the kink of the solid curve in Fig. 1. It is assumed that at the kink the n-type bulk is fully compensated, i.e. intrinsic, and after that deep acceptor generation turns the bulk p-type. The second detector is a very interesting case because it is very near to the kink in Fig. 1.

For cross-section measurements, the sample chips were cut into two halves with an ordinary diamond pen and bending method: pressing half of the chip with a line ruler on paper towels and making a short scribe at the edge of the chip which makes the chip break along the $\langle 110 \rangle$ crystal plane. The chip breaks naturally along the $\langle 110 \rangle$ plane producing a clean surface that is exactly perpendicular to the wafer surface. The electric field will not bend near this perpendicular surface, which is essential for the correctness of the electric field measurement.

After cutting, the samples were usually placed into the SEM vacuum chamber within 10 min. A few hours in atmosphere did not influence the measurement, but a prolonged storage (weeks or months) in atmosphere at room temperature (and a thicker native oxide) can make the measurement impossible.

3. Electron microscopy

During voltage–contrast measurements in the SEM, the front side (p^+) was at zero potential, and a positive voltage was applied to the back side (n^+). The measurement system is explained in Ref. [7]. In this study, we spent 80 s to make one line scan of about $400 \mu\text{m}$, which makes the scanning speed to be $5 \mu\text{m s}^{-1}$. The contrast C is converted to voltage V according to the equation

$$V = -M \ln(1 + C/K) \quad (1)$$

where the contrast scaling factor K and the voltage constant M are found by the procedure described in Ref. [7].

In heavily irradiated detectors, we expect most of the change in potential to take place near the back side of the detector. This could distort the voltage contrast in areas where the potential is

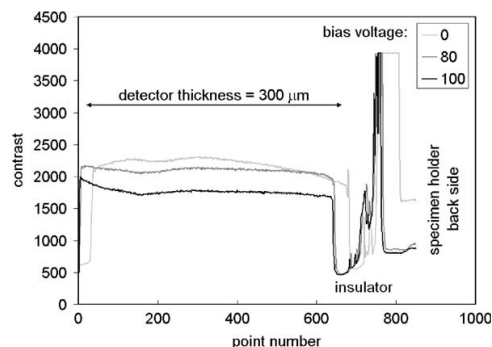


Fig. 2. Proximity test results. An insulator was put between the detector back side and the specimen holder, and the bias voltage was fed to the specimen holder back side.

near zero. In Ref. [7] we did not take such a proximity effect into account, but instead supposed that a high positive bias only lowers the contrast uniformly. This assumption was now tested by placing a thin insulator between the back side of the detector and the specimen holder and applying a positive voltage to the specimen holder back side while the specimen holder front side and the specimen itself (discarding built-in potentials) were at zero potential. The result is shown in Fig. 2 for zero bias and two high-bias voltages. The only proximity effect is seen surprisingly at zero bias. This is because the insulator was charged during image watching before the first line scan. After 25 min when making the scans with higher voltages, the insulator was discharged and no proximity effect is seen in detector thickness scale, and we can still use pure Eq. (1) to convert the contrast to voltage.

All SEM measurements were made at room temperature. The detector current was measured in situ during each voltage–contrast line scan.

4. Results

4.1. Non-irradiated sample

Fig. 3 displays the measured voltage as a function of distance from the front surface (p) in the non-irradiated sample at eight bias voltages.

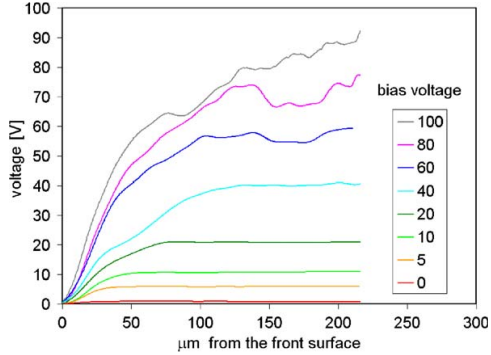


Fig. 3. Voltage as a function of distance from the front surface in the non-irradiated sample. Curves are in the same order from bottom to top as in the legend.

The result is very near to the theoretical one except for the noise above 40 V. Assuming no voltage drop in the undepleted bulk, the bias voltages is across the depletion layer. Thus, we can see the spreading of the depletion layer as a function of bias voltage. Also, it is worth noting that the lowest curve, with zero bias, deviates from zero. This is not surprising, because with this method the built-in potential can also be seen.

The first derivative of the voltage yields the electric field

$$E = -dV/dx. \quad (2)$$

Differentiating the voltage data of Fig. 3 point-by-point produces the electric field as a function of position as displayed in Fig. 4. The electric field is negative according to standard axis definition: positive x -axis points to right, where the positive bias voltage is applied. The point-by-point differentiation again increases the noise above 40 V bias.

In theory, the negative peaks of the field curves should show the pn-junction depth and be at the same distance at every bias voltage. The processed junction depth is assumed to be 3 μm . The set of curves in Fig. 4 clearly overestimates this, specially at higher bias voltages. The reason for this is that the depth of the pn-junction is only a very small portion of the total inspected distance, the number of measurement points before the junction being less than 10 out of a total 800 points. The inevitable noise reduction by averaging also

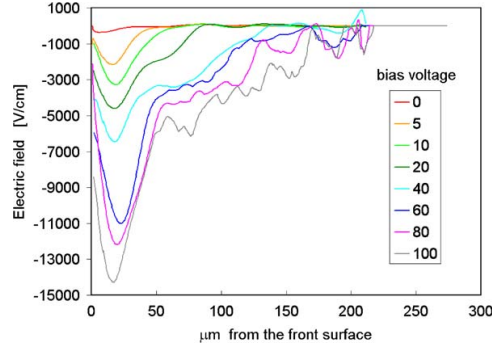


Fig. 4. Electric field in the non-irradiated sample. Curves are in the same order from top to bottom as in the legend.

distorts the original signal near the surface. For this purpose it will do, and we have not increased the resolution, although it would be technically possible.

4.2. Highest fluence

In the sample irradiated with $6.45E14 \text{ n}_{\text{eq}}/\text{cm}^2$, we expect that the situation is almost reversed compared with the non-irradiated case. The n-type bulk is expected to be inverted to p-type, and the pn-junction is expected to reside near the back side of the detector.

Fig. 5 presents the results of measuring the potential distribution inside the detector irradiated with the highest fluence. Clearly, the detector starts to deplete from the back when increasing the bias voltage, which indicates that the pn-junction really has moved to the back side of the detector and the bulk has reversed its type from n to p.

After differentiating the voltage data of Fig. 5 we get the electric field curves as shown in Fig. 6.

Specially at higher bias voltages, the curves in Figs. 5 and 6 have non-ideal features. The largest electric field appears near the back side at a distance of 15–20 μm from the back surface, which is the electrical pn-junction depth. There is, however, a smaller peak of the electric field near the front surface. The field curves indicate that the bulk is not yet fully depleted at the highest measurement voltage 100 V. These two imply that

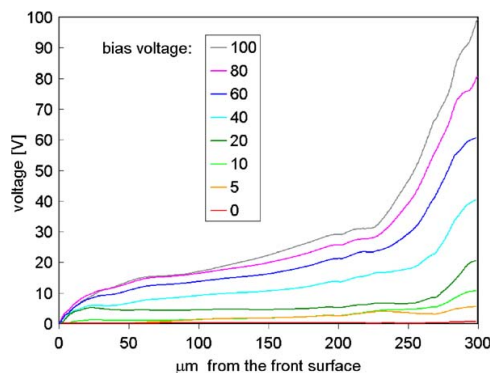


Fig. 5. Voltage as a function of distance from the front surface at eight bias voltages in the sample irradiated with 1 MeV neutron equivalent fluence of $6.45E14\text{ cm}^{-2}$.

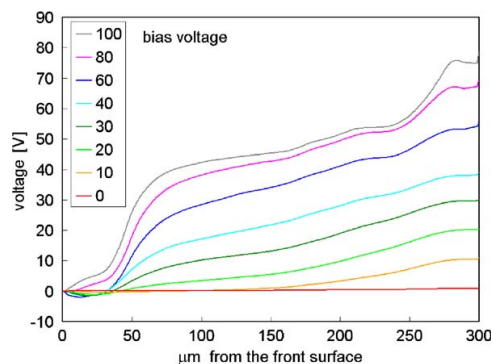


Fig. 7. Voltage as a function of distance from the front surface at eight bias voltages from 0 to 100 V in the sample irradiated with 1 MeV neutron equivalent fluence of $1.09E14\text{ cm}^{-2}$.

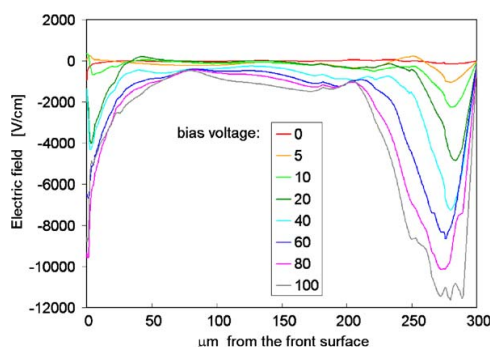


Fig. 6. Electric field in the sample irradiated with 1 MeV neutron equivalent fluence of $6.45E14\text{ cm}^{-2}$.

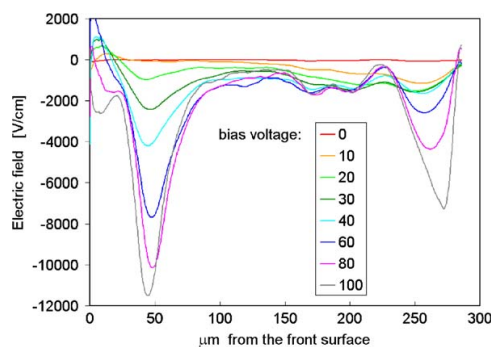


Fig. 8. Electric field in the sample irradiated with 1 MeV neutron equivalent fluence of $1.09E14\text{ cm}^{-2}$.

there is a pn-junction also near the front surface. A small electric field exists throughout the bulk. The leakage current in the irradiated detectors is very high, maximum $50\text{ }\mu\text{A}$, during this measurement. Using the resistivity of intrinsic silicon, $235\text{ k}\Omega\text{ cm}$, bare leakage current is calculated to form a voltage difference of 3 V in the examined piece of silicon, which is not enough to explain all the bulk field.

4.3. Intermediate fluence

Fig. 7 displays the voltage as a function of distance from the front surface at eight bias

voltages for the sample irradiated with $1.09E14\text{ n}_{\text{eq}}/\text{cm}^2$. The depletion starts from the back indicating a junction there. At higher bias voltages the spreading of the depletion layer stops at $45\text{ }\mu\text{m}$, but continues when increasing the bias voltage above 60 V . This together with the field curves shown in Fig. 8 indicate a pn-junction at this depth.

5. Discussion

From TCT measurements, the form of the electric field can be approximated. The overall

intensity of the field is very much determined by the applied bias voltage and detector thickness. The SEM measurements presented here provide a similar magnitude but a different shape. When studying an irradiated FZ detector, a simulation model used with TCT measurements yields a stepwise linearly changing electric field with two peaks located at the front and back contacts [11]. These SEM measurements show the same two peaks, but at some meaningful distance from the contacts. At the contacts, the electric field should be zero.

The calculation of the electric fields in Ref. [6] gives the same magnitude more accurately but a different shape compared with these SEM results. For irradiated detectors two peaks are present there, but they are located at the contacts just as in the TCT results.

OBIC measurements [5] result in very similar shapes of the electric field as found in this examination, the peaks being at some distance from the front and back contacts.

According to these SEM measurements, already a fluence of $1.09E14 n_{eq}/cm^2$ inverts the lightly doped n-bulk to p-type at least partly, so that the detector starts to deplete from the back side with small bias voltages. When increasing the bias voltage, a separate electric field starts to form also near the front side of the detector. In lightly irradiated detectors, this front side pn-junction is finally found to be the principal one. In heavily irradiated detectors, the back side junction is the most important.

In principle, the number of pn-junctions should be odd in a structure like this. A third pn-junction between these two observed junctions is forward-biased and very gently graded in an almost intrinsic area and thus difficult to locate. It must be emphasized that small peaks of the electric field in the data of this examination are due to noise caused by point-by-point numerical differentiation and not due to a third junction.

6. Conclusion

In the cross-section of a non-irradiated silicon radiation detector, the voltage–contrast measure-

ment with a scanning electron microscope yielded exactly the same electric potential and field curves which were predicted in theory.

In a heavily irradiated detector (1 MeV neutron equivalent fluence of $6.45E14 cm^{-2}$), the principal pn-junction and electric field were found near the back side. A secondary pn-junction existed very near the front side, probably at the site of the original manufactured junction.

In a sample irradiated with an intermediate fluence of 1 MeV neutron equivalent fluence of $1.09E14 cm^{-2}$ the depletion started from the pn-junction located at 25–40 μm from the back side. At larger bias voltages, the principal pn-junction was found at 45 μm from the front side and a smaller part of the total electric field lay near the back side of the detector.

Already small irradiation fluences compared to the requirements of the proposed Super-LHC fluence of fast hadrons up to $10^{16} cm^{-2}$ change the electrical behaviour of FZ silicon radiation detectors dramatically.

The claim that the original p⁺/n-junction is always preserved even after heavy irradiation [12] is also found to be true in this investigation.

Acknowledgements

This work has been performed in the framework of CERN RD50 Collaboration.

References

- [1] RD50 Status Report, CERN/LHCC-2003-058 (2003), p. 30.
- [2] R. Wunstorff, M. Benkert, N. Claussen, N. Croitoru, E. Fretwurst, G. Lindström, T. Schulz, Nucl. Instr. and Meth. A 315 (1992) 149.
- [3] V. Eremin, Z. Li, IEEE Trans. Nucl. Sci. NS-41 (6) (1994) 1907.
- [4] V. Eremin, N. Strokan, E. Verbitskaya, Z. Li, Nucl. Instr. and Meth. A 372 (1996) 388.
- [5] A. Castaldini, A. Cavallini, L. Polenta, F. Nava, C. Canali, Nucl. Instr. and Meth. A 476 (2002) 550.
- [6] V. Eremin, Z. Li, S. Roe, G. Ruggiero, E. Verbitskaya, Nucl. Instr. and Meth. A 535 (2004) 622.
- [7] K. Leinonen, ref. no. CERN 05-042, Nucl. Instr. and Meth. A, 2005, submitted for publication.

- [8] J. Härkönen, et al., Nucl. Instr. and Meth. A 514 (2003) 173.
- [9] E. Tuovinen, Processing of Cz-Si pad detectors with different thermal treatments, in: Proceedings of the Third RD50 Workshop on Radiation Hard Semiconductor Devices for very High Luminosity Colliders, 3–5 November 2003, CERN.
- [10] A. Virtanen, J. Hyvönen, K. Ranttila, I. Rekikoski, J. Tuppurainen, Nucl. Instr. and Meth. A 426 (1999) 68.
- [11] RD50 Status Report, CERN-LHCC-2004-031, 2004.
- [12] Z. Li, H.W. Kraner, IEEE Trans. Nucl. Sci. NS-39 (1992) 577.

Publication IV

T. Palviainen, T. Tuuva, K. Leinonen

“Minimizing guard ring dead space in the Si detector with n-guard ring at the edge of the detector”

Reprinted from Nuclear Instruments and Methods in Physics Research A 573, pp. 277–279,
Copyright (2007), with permission from Elsevier.



Minimizing guard ring dead space in silicon detectors with an n-type guard ring at the edge of the detector

Tanja Palviainen*, Tuure Tuuva, Kari Leinonen

Lappeenranta University of Technology, P.O. Box 20, FIN-53851 Lappeenranta, Finland

Available online 28 November 2006

Abstract

Detectors with n-type silicon with an n⁺-type guard ring were investigated. In the present work, a new p⁺/n/n⁺ detector structure with an n⁺ guard ring is described. The guard ring is placed at the edge of the detector. The detector depletion region extends also sideways, allowing for signal collection very close to the n-guard ring. In this kind of detector structure, the dead space of the detector is minimized to be only below the guard ring. This is proved by simulations done using Silvaco/ATLAS software.

© 2006 Elsevier B.V. All rights reserved.

PACS: 29.40.G

Keywords: Silicon-based detector; Simulation of detector; Detector characterization; Guard ring; Dead space

1. Introduction

Silicon detectors in high-energy physics experiments require a reliable performance under irradiation. Minimizing dead space is an additional advantage as it enhances the efficiency of a detector [1]. The guard ring technique has evolved to minimize dead space at the edge of detectors. Also the guard ring structure is used to improve the breakdown performance of silicon detectors.

Detectors collect charge from the depletion region. It is, therefore, important to minimize dead space, from where it is not possible to collect charge. Usually depletion forms vertically from anode to cathode, but in this application, where there is an n-type guard ring at the edge of the detector the depletion region also extends sideways. This phenomenon is due to the cathode and the guard ring being of the same doping type. The remaining dead space is only directly under the guard ring.

2. Structure

Fig. 1 describes the structure of the proposed new p⁺/n/n⁺ detector structure with the n⁺ guard ring. The guard

ring is placed at the edge of the detector and the distance from the p⁺ anode to the guard ring is 200 μm. The depth of the pn-junction and the n-type guard ring is 3 μm. The width of the guard ring is 3 μm as well.

3. Simulation results

Simulations were done using Silvaco Virtual Wafer Fab (VWF) software, which is a simulation tool for electronic design. It includes different kinds of tools for device and process simulation [2]. ATLAS [2] software is meant for use in the design and development of all types of semiconductor devices. Silvaco is a physics-based simulator, which predicts electrical characteristics associated with specific physical structures and conditions [2].

Simulation results of the p⁺/n/n⁺ detector structure with n⁺ guard ring are presented below. The simulations were done using high resistivity silicon (ρ is $\approx 4 \text{ k}\Omega \text{ cm}$). The voltage required for the full depletion of the device has been calculated to be -70 V . In these simulations, -70 V is applied to the p-type anode (A in Fig. 2). The cathode (K in Fig. 2) covers the full backside of the detector. A bias voltage is applied to the anode and the cathode is connected to zero potential. The guard ring (g in Fig. 2) is connected to the cathode.

*Corresponding author.

E-mail address: tanja.palviainen@lut.fi (T. Palviainen).

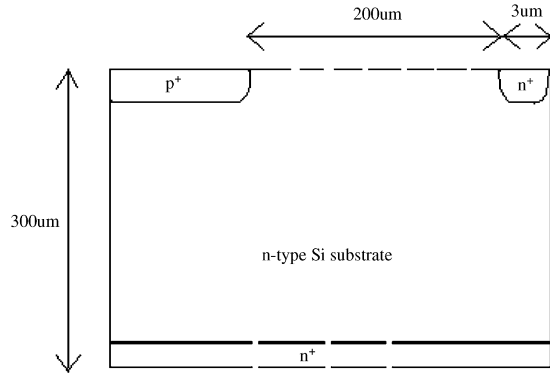


Fig. 1. The cross-section (not to scale) of the detector structure. The n^+ -type guard ring is placed at the edge of the detector to minimize dead space.

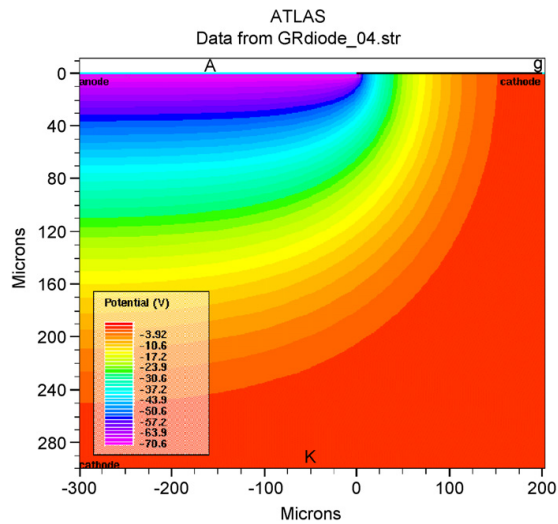


Fig. 2. The simulated potential of the detector.

3.1. Potential

Fig. 2 shows the simulated potential of the detector. A voltage of -70 V is applied to the anode. With that potential, the device is fully depleted.

3.2. Leakage current

Fig. 3 shows the simulated leakage current of the detector as a function of the anode bias up to -70 V. The leakage current curve flattens towards -70 V indicating full depletion of the structure.

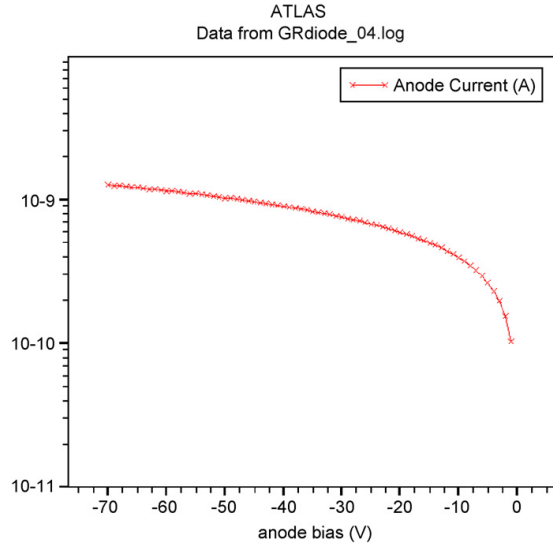


Fig. 3. The simulated leakage current of the detector.

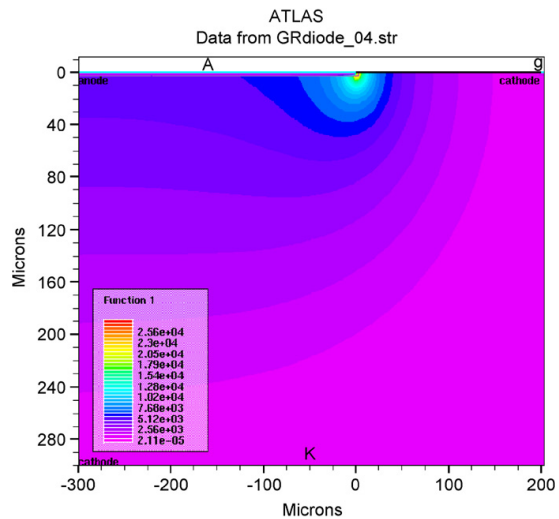


Fig. 4. The simulated electric field of the detector.

3.3. Electric field

Fig. 4 shows the simulated electric field inside the detector. A strong electric field is formed at the end of the p-type anode.

4. Conclusions and future developments

In the detector structure described in this paper, the charge collection area is extended sideways towards the

n-type guard ring, hence minimizing the total dead space at the detector edge. We expect that by adding an extra electrode ring at the edge on the cathode side of the detector, we can further extend the charge collection area. Although this would require double-sided processing of the wafers, the lithographical requirements for the backside are less stringent than for the frontside of the detector. There is also a possibility to have n^{2+} -doping along the full edge of

the detector to achieve full depletion up to the edge of the detector but this would require special processing.

References

- [1] K. Ranjan, et al., *Solid-State Electron.* 48 (2004) 1587.
- [2] Silvaco International, *ATLAS User's Manual*, vols. I and II, <<http://www.silvaco.com/>>.

Publication V

T. Grönlund, Z. Li, G. Carini, M. Li

“Full 3D simulations of BNL one-sided silicon 3D detectors and comparisons with other types of 3D detectors”

Reprinted from Nuclear Instruments and Methods in Physics Research A, available at doi:10.1016/j.nima.2007.12.005. Copyright (2007), with permission from Elsevier.

1 **Full 3D simulations of BNL one-sided silicon 3D detectors and comparisons with other**
2 **types of 3D detectors**

3
4 Tanja Grönlund^{a,b*}, Zheng Li^a, Gabriella Carini^a, and Michael Li^{a**}

5 ^a*Brookhaven National Laboratory, Upton, NY, USA*

6 ^b*Lappeenranta University of Technology, Lappeenranta, Finland*

7
8 **Abstract**

9
10 Full 3D simulations have been carried out on the BNL one-sided single-type column and
11 dual-type column 3D Si detectors (p-type substrate). Due to the facts that columns are not etched
12 all the way through, all electrodes are on the front side, and the backside was not supported nor
13 processed at all, the BNL one-sided 3D detectors are true one-sided detectors. Simulations show
14 that the volume under the columns where it is supposed to be dead space (about 10%) can be
15 depleted at high biases with some modest electric field, leading to the possibility of recovering
16 some sensitivity from this region. This region can also provide some sensitivity to particle tracks
17 directly through the columns. The dual-type column detectors are the best in radiation hardness
18 due to their low depletion voltages and short drift distances. Single-type column detectors are
19 more radiation hard than the planar detectors due to their lower depletion voltages. Single-type
20 column detectors are easier to process than dual-type column detectors, but have a more
21 complicated, non-uniform electric field profile. The BNL one-sided 3D detectors were compared
22 to various 3D detector structures developed by other institutes. The field profiles for all types of
23 dual-type column 3D detectors are similar with just some minor differences on both surfaces

1 (front and back). The BNL single-type column one-sided 3D detectors have some major
2 difference from the Trento ones: 1) the high electric field is on the sensing electrode side (pixel or
3 strip); and 2) it can develop some high electric field along the junction column as bias voltage
4 increases.

5

6 PACS: 29.40

7

8 Keywords: silicon detectors, 3D sensors, 3D detectors, device simulation, electric field

9

10 *Corresponding author: Lappeenranta University of Technology, P.O. Box 20, FIN-53851
11 Lappeenranta, Finland, tel.: +358-5-6216764, fax: +358-5-6216799, email: tanja.gronlund@lut.fi.

12 **Permanent address: 30 Hancock Ct., S. Setauket, NY, 11973, USA

13

14 **1. Introduction**

15

16 To achieve some of the prime goals of high energy physic experiments – for example the
17 discovery and possible study of Higgs-particles – silicon detectors have to operate in extremely
18 harsh radiation environments. In the proposed upgrade of LHC (Super-LHC, SLHC), the increase
19 of the maximal fluence and the beam luminosity up to 10^{16} neq/cm² and 10^{35} cm⁻²s⁻¹, respectively,
20 will require detectors with dramatic improvement in radiation hardness. Therefore, the main
21 goals of detector development for the SLHC are concentrated on the technologies that minimize
22 the radiation degradation and/or maximize the detector radiation tolerance. The interest for the
23 3D silicon detectors is continuously growing because of their many advantages as compared to

1 conventional planar detectors: the devices can be fully depleted at low bias voltages, the speed of
2 the charge collection is high, and the collection distances are about one order of magnitude less
3 than those of planar technology strip and pixel detectors with electrodes limited to the detector
4 surface. Also the 3D detectors exhibit high radiation tolerance, so the ability of the silicon
5 detectors to operate after irradiation is increased.

6 The architecture for solid-state radiation detectors using a three-dimensional array of
7 electrodes that penetrate into the detector bulk were proposed by S.I. Parker, C.J. Kenney and J.
8 Segal in the mid 90's [1]. This standard design of 3D detectors present columnar electrodes of
9 both doping types arranged in adjacent cell and penetrated through the silicon substrate.
10 However, the fabrication process of standard 3D detectors is rather difficult. The difficulty in
11 processing for standard 3D Si detector we referred here is mainly the need for wafer bonding
12 (supporting wafer) for mechanical strength, especially for edge-sensitivity in standard 3D Si
13 detector, and possible double-sided processing. We have made the first prototype of single-type
14 column 3D Si detectors, where the n^+ columns were etched by CNM using the well calibrated,
15 uniform etching rate to get 270 μm deep columns with a few percent in variations, which will
16 result in some difference in the depth of the volume under the columns [2]. However as we will
17 show late in simulations, since the volume under the columns may be largely depleted at high
18 enough biases, the variation in the dead volume under the column may be minimum. Better
19 control in etching rate can reduced this variation even more, which is one of the areas we are
20 trying to improve in the technology.

21 In this paper, we will present simulations for two single-sided 3D detector designs [2],
22 one with the single type (n-type) of the columns and the other one with dual type of the columns
23 (n and p-type) on the p-type substrates. With full 3D simulations of different detector types, we

1 will demonstrate that one can achieve similar electric field profile between BNL dual column 3D
2 detector and other dual column 3D detectors developed by other institutes with benefit of the true
3 one-sided process. In the case of the BNL single type column detector we will show that the high
4 electric field is on the pixel side, which is the sensing area.

5

6 **2. Full 3D simulations and device description**

7

8 Full 3D simulations on 3D Si detectors were performed using the DEVICE3D package of
9 ATLAS Silvaco [3]. The numerical simulations were aimed to investigate the electric field
10 profiles in various 3D detectors. The strength of the electric field with the applied voltage when
11 the full depletion is reached, expresses the high and low field areas in the detector and its
12 sensitivity for particles. A sketch of the BNL one-sided single-type column detector is shown in
13 Fig. 1. The columnar electrodes are all of the same type (n-type here), which are of the type
14 opposite to the substrate one (p-type here) and they extend to 270 μm into the 300 μm deep bulk.
15 The ohmic contacts are achieved by placing two ion-implanted electrodes (p-type here) on the
16 front surface, in the other two corners in a simulation cell as shown in Fig. 1b, where a minimum
17 cell for simulation and a unit cell for the detector are also shown. The backside is covered by a
18 uniform silicon oxide layer and is never processed, so the process is a true one-sided. The n^+
19 electrodes (columns) and p^+ electrodes (implants) are covered with aluminum layers on the
20 detector surface. Other areas of the detector front side are covered with silicon oxide. One unit
21 cell is simulated with two n-type columns on the opposite corners and two p-implants (0.5 μm
22 deep) in the other corners. In our simulation here, n^+ columns are surrounded by p-stops as
23 marked in Fig. 1b. Note here that p-spray technology may not be used here since this will short

- 1 all the p^+ electrodes together, and place them in contact with the n^+ electrodes, which can easily
 2 cause breakdown along the surface.
 3

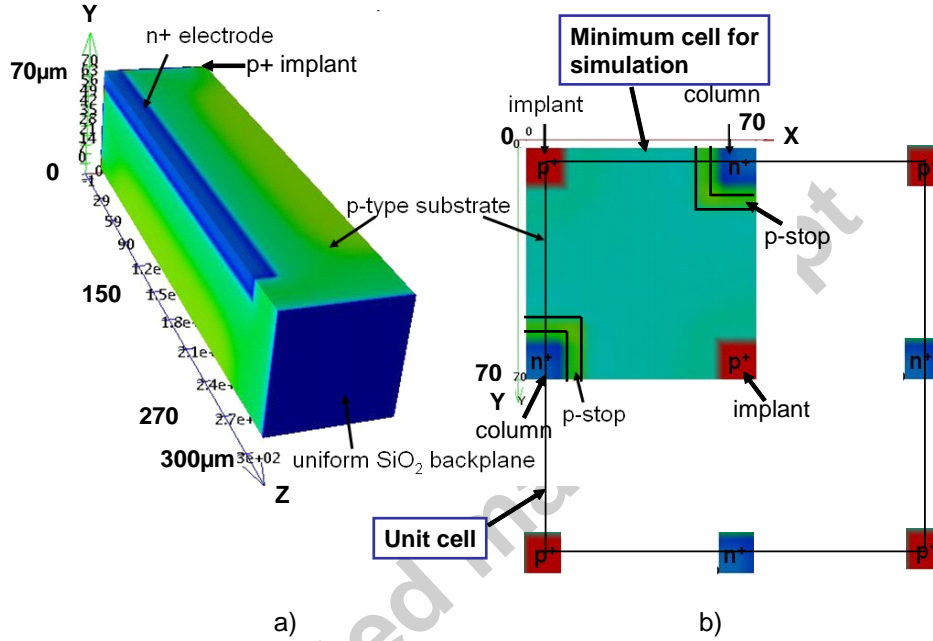
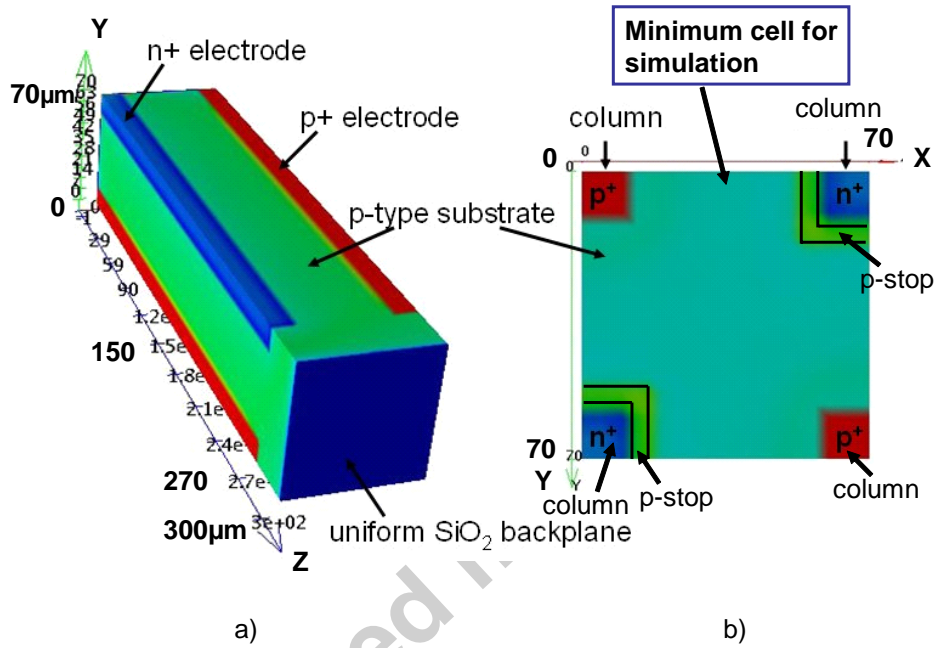


Fig. 1. Sketch of a BNL one-sided single-type column 3D detector, a) a 3D cell in the simulation and b) top view of a minimum cell for simulation and a unit cell for the detector.

A sketch of the BNL dual-type column detector is shown in Fig. 2. In this structure there are two n-type and two p-type doped columns on p-type substrate. Same types of doped columns are placed to the opposite corners in the simulation cell. All the columns are placed on the front side of the detector and they extend 270 μm into the 300 μm thick p-type bulk. N-type columns

1 are surrounded by p-stops again similar to the previous case. The backside is covered by a
 2 uniform silicon oxide layer and is never processed, so the process is again true single-sided.
 3



4
 5
 6 Fig. 2. Sketch of a one-sided dual-type column 3D detector, a) a 3D cell in the simulation and b)
 7 top view of a minimum cell for simulation. The unit cell for the detector is similar as one shown
 8 in Fig. 1b.

9
 10 In the simulations the p-type substrate doping concentration was $1 \times 10^{12} \text{ cm}^{-3}$ in all cases.
 11 The edge of the cell is $70 \mu\text{m}$, while the edge of the electrode is $10 \mu\text{m}$. Then the distance
 12 between the electrodes is $50 \mu\text{m}$.

13 For a planar detector, the depletion voltage V_{fd} needed to fully deplete the detector varies
 14 with doping concentration and substrate thickness by [4]:

1

$$V_{fd} = \frac{|N_{eff}|d^2q}{2\epsilon\epsilon_0} - V_{bi} \quad (1)$$

3

4 Very often the built-in voltage V_{bi} is neglected since the depletion voltage is in most cases more
5 than one order of magnitude higher.

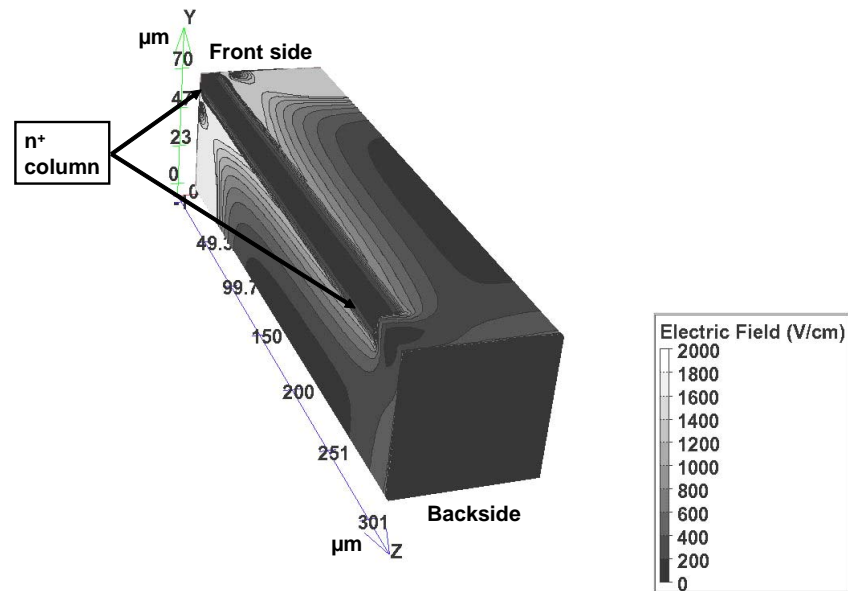
6 In 3D detectors, the depletion grows laterally from the electrodes as the bias voltage is
7 increased. For dual-type column 3D detectors, the substrate is fully depleted when the depletion
8 region extends fully from the n-type column to the adjacent p-type column. For single-type
9 column 3D detectors, the depletion region may have depth dependence (in thickness direction),
10 but nevertheless, the full depletion can be reached when the depletion zones of two adjacent n-
11 type columns (in our case) are joined near the bottom of the columns. We can estimate the full
12 depletion voltage for a dual-column 3D detector as shown in Fig. 2 with $N_{eff} = 1 \times 10^{12} \text{ cm}^{-3}$ and
13 column spacing of $t = 50 \text{ }\mu\text{m}$: it is approximately 5 volts. It is clear that one of the main
14 advantages for 3D detectors is its low full depletion voltage due to the dense placement of the
15 electrodes; the depletion distance t is independent of detector thickness d , and can be made much
16 shorter than d . For example, the full depletion voltage of a $300 \text{ }\mu\text{m}$ thick 3D detector with
17 electrode placement distance of $50 \text{ }\mu\text{m}$ is about 5 volts, as compared to 68 volts for the equivalent
18 planar $300 \text{ }\mu\text{m}$ thick 2D device. However, the actual simulated full depletion voltage, obtained
19 from our 3D simulation, for a 3D detector can be slightly higher (about a factor of 1.4 higher)
20 than that estimated using Eq. (1), due mainly to the small electrode effect.

21

22 3. Electric field simulation

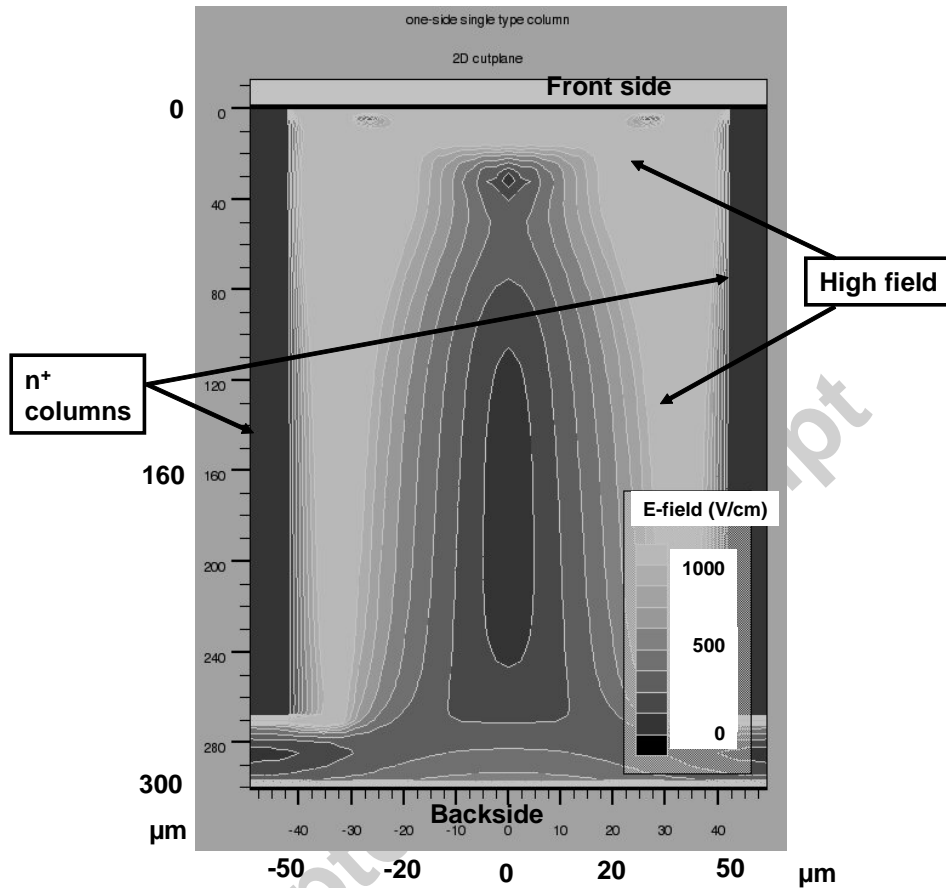
23

1 The sensitive region of a detector can be seen from the simulated electric field profile in
 2 the detector. BNL one-sided single-type column detectors have the high electric field region on
 3 pixel side (front side) of the detector and along the n-type columns, as shown in Fig. 3 for a
 4 simulation cell shown in Fig. 1. The bias voltage here is 100 volts on the n-type electrodes with
 5 respect to 0 volts on the p-type electrodes. It is clear that the electric field is highly non-uniform,
 6 and is the lowest in the volume directly under the p-type electrodes which are only implants on
 7 the front surface.



8
 9 Fig. 3. Simulated 3D electric field profile in a BNL one-sided single-type column 3D detector at
 10 100 V bias.

11
 12



1

2

3 Fig. 4. A 2D cut plane of the simulated electric field in a BNL one-side single-type column 3D
 4 detector at 100 V bias.

5

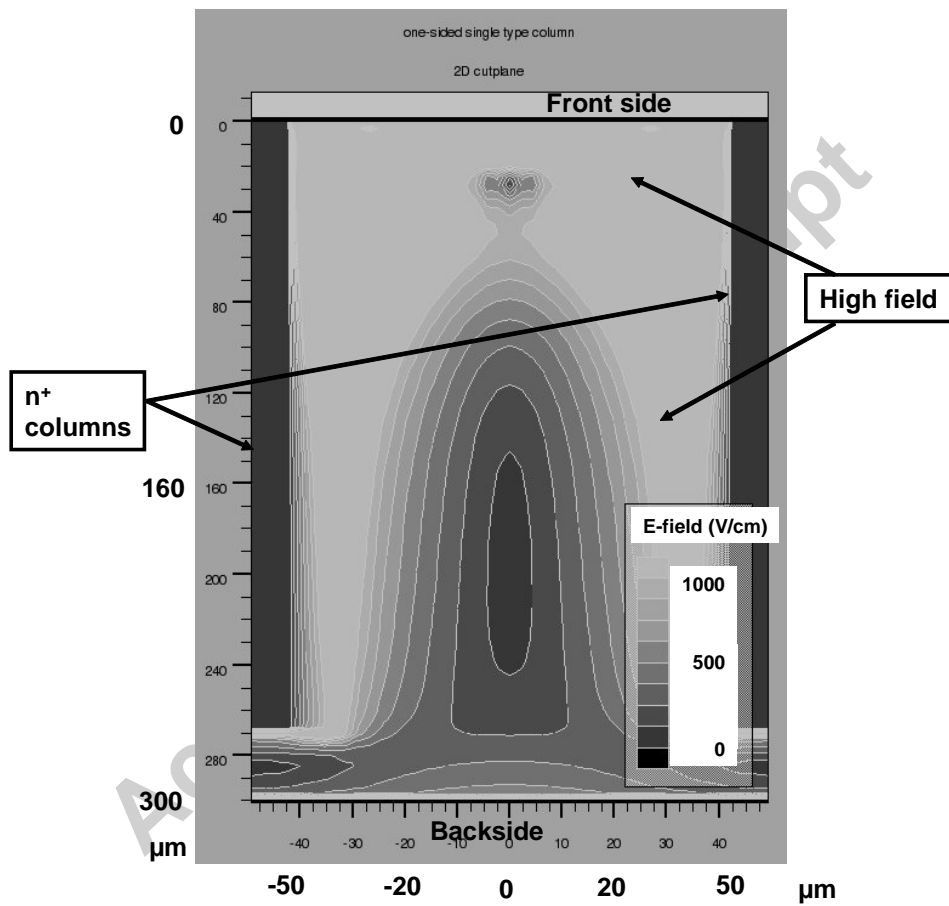
6 To see the electric field inside the detector in more details, we plot a 2D cut plane along
 7 the two n-type columns in Fig. 4. From the figure, we can observe that, for BNL one-sided
 8 single-type column 3D detectors biased at 100 volts: 1) the front side (or pixel side) is with the
 9 highest field, and it extends about 30 μm into the detector; 2) there are high field along the n^+

1 columns all the way through the detector with a volume of about 2/5 of that between the n^+
2 columns; 3) the medium field between the n^+ columns also occupies about 2/5 of the volume; 4)
3 the lowest field is near the middle of the two n^+ columns, which occupies about 1/5 of the
4 volume; and 5) there are some medium to low fields (on average of about 300-400 V/cm²) in the
5 volume under the n^+ columns (30 μm depth). So the volume under the columns may be depleted
6 to a degree that can make this volume with some sensitivity to particles as well. In this volume,
7 the largest drift distance for electrons is larger number of the depth of this region (30 μm) and the
8 electrode spacing (50 μm), that is 50 μm in our case. It will take about 9 ns for electrons to drift
9 to an n electrode column, which can be done even with the 25 ns shaping time for SLHC. So in
10 this sense, the volume under the column may not be entirely dead. Point 5) also raised the
11 possibility that the volumes directly under the n^+ columns may serve as way to recover some
12 sensitivities from the supposed dead volumes of the n^+ columns themselves. It is interesting to
13 note here that the simulated full depletion voltage for the BNL one-side single-type column 3D
14 detectors shown in Fig. 1 is much smaller (5-10 volts) than that of planar detectors (80 volts) with
15 the same thickness and resistivity. In this aspect, this type of 3D Si detector may be more
16 radiation tolerant than the 2D planar Si detectors, especially after modest fluence ($>1 \times 10^{14}$
17 $n_{\text{eq}}/\text{cm}^2$) when the N_{eff} becomes higher and electric field becomes better. This latte point was first
18 systematically simulated by Trento for their single-type column 3D Si detector [5], where
19 detectors built on lower initial resistivity initial material have shown better electric field profiles.
20 However, higher voltage than the full depletion voltage should be used to get some high field
21 near the back of the detector. Also, the longest drift length for a particle-generated free carrier
22 (holes here) is still the whole detector thickness that can be much larger than the column spacing,

1 one may lose the contribution to CCE of one type of carrier (holes here) at very high radiation
 2 fluences ($>2 \times 10^{15} \text{ n}_{\text{eq}}/\text{cm}^2$).

3

4



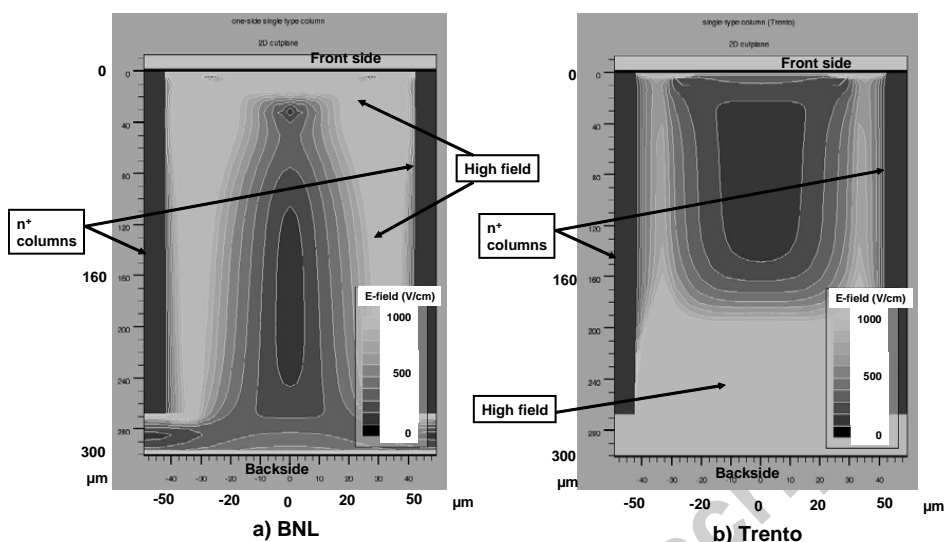
5

6 Fig. 5. A 2D cut plane of the simulated electric field in a BNL one-sided single-type column 3D
 7 detector at 200 V bias.

8

1 To see the bias voltage effect on this type of 3D detectors, we plot a 2D cut plane for the
2 same detector as shown in Fig. 3 and 4, this time the bias is increased to 200 volts. As it can be
3 seen, the main change here is in the Point 1) as listed above: the high field region near the front
4 surface is extended to about 80 μm into the detector bulk as compared to 30 μm in the case of
5 100 volts. Points 2-5 are almost the same as those for the 100 volts case.

6 It is interesting to compare the field profiles between the BNL one-sided single-type
7 column 3D detector and the Trento single-type column 3D detector proposed early by ITC-IRST
8 (Trento) [5-6]. In a Trento single-type column 3D detector, n-type columns are placed in every
9 corner in one cell: i.e. n^+ columns in places where p^+ implants are located (Fig. 1) for the BNL
10 one-sided single-type column 3D detector. The p^+ ohmic contact is a uniform p^+ ion implant on
11 the backside. Fig. 6 shows the 2D electric field profiles of the two types of 3D detectors at 100
12 volts along a cut plane between the two n^+ columns. Field profile differences are clearly shown:
13 1) instead of high field on the pixel side (BNL), the high field in a Trento detector is near the
14 backside; 2) instead of some high field developed along the n^+ columns all through the column
15 length (BNL), half of the n^+ columns length near the pixel side is with low field in a Trento
16 detector; and 3) in fact, most volume under the pixel (about 40% of the detector volume) is with
17 low field in a Trento detector. BNL one-sided single-type column 3D detector provides better
18 field distribution, and may therefore give better charge collection performance.



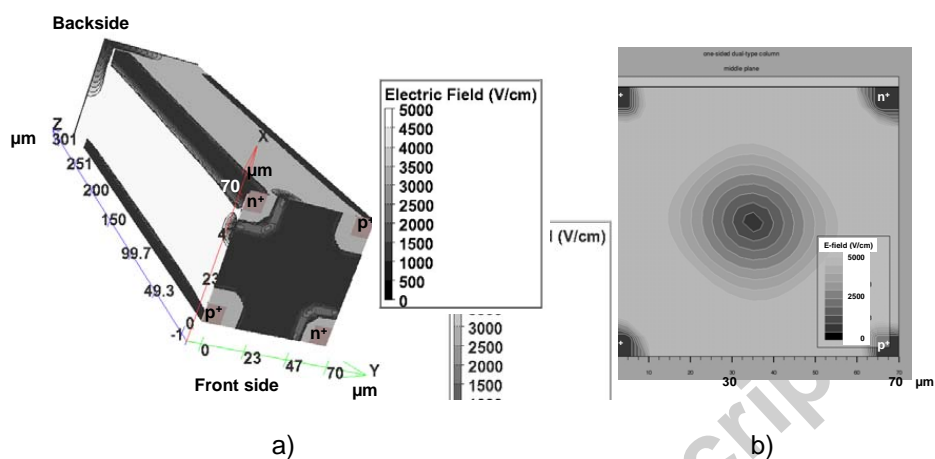
1

2 Fig. 6. Comparison of electric field profiles between two types of single-type column 3D
 3 detectors operated at 100 V bias. The 2D cut plane is along the two n^+ columns.

4

5 The 3D electric field profile of a BNL one-sided dual-type column 3D detector (Fig. 2)
 6 operated at 40 volts is shown in Fig. 7. It is clear that high field is distributed all along the n^+ and
 7 p^+ columns, and throughout the detector. Again, similar to the BNL one-sided single-type column
 8 3D detector, there are some fields developed under the columns near the backside, which could
 9 provide extra sensitive regions for the detector. However, the field profile is still highly non-
 10 uniform as shown in a 2D cut plane in the middle of the detector (at half of the detector thickness,
 11 150 μm). The low field is near the center between the four electrode columns in a cell, and the
 12 field is zero right at the center point (saddle point). This low field region is common for all dual
 13 column 3D detectors, which is due to the symmetry in the detector cell. This is similar to the 2D
 14 multi-electrode, planar sensors where there exists a zero field line (point) parallel to the top
 15 surface midway between signal electrodes, also due to symmetry.

1



2

3

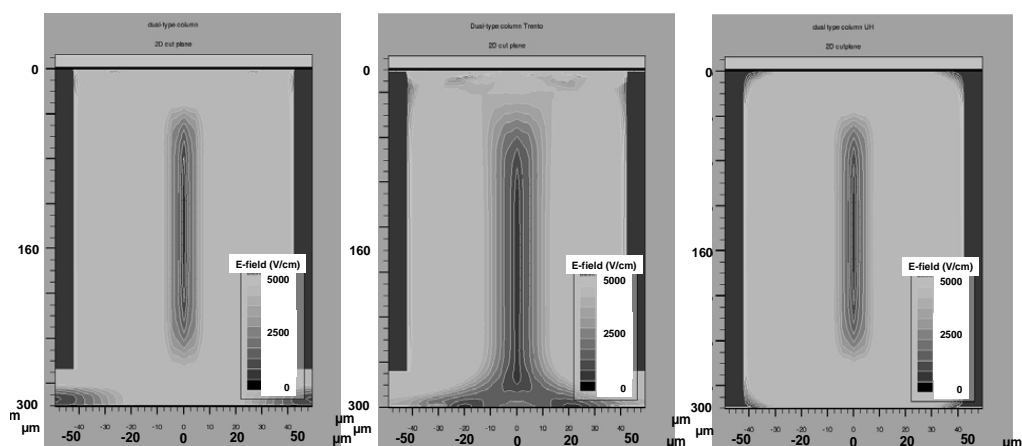
4

5 Fig. 7. Electric field profiles of a BNL one-sided dual-type column 3D detector operated at 40 V
 6 bias: a) 3D profile; b) 2D profile in a cut plane in the middle ($Z = 150 \mu\text{m}$).

7

8 The electric field profile in a dual-type column 3D Si detector is more uniform than that
 9 in a single-type column 3D Si detector: the non uniformity is minimum along the detector
 10 thickness, especially 20-30 μm away from either surfaces. The dual-type column 3D Si detector
 11 is easier to deplete at lower bias voltages than single-type column 3D detector. Comparing
 12 different dual-type column 3D detector structures: the standard one developed by Parker [1], the
 13 BNL one-sided one, and the double-sided one developed by CNM (Barcelona), where p-type and
 14 n-type columns are placed on the opposite surfaces [6], the electric field profiles are extremely
 15 similar in the vast bulk of the detectors, only minor differences are found on the surface of the
 16 detector at 100 V bias, as shown in Fig. 8.

17



a) BNL

b) CNM

c) UH

Fig. 8. Comparison of electric field profiles between three types of dual-type column 3D detectors operated at 100 V bias. The 2D cut plane is along the two n^+ columns.

In fact, one of the main differences among various types of dual-type column 3D detectors is the processing. BNL one-sided dual-type column 3D detector is true one-sided process: meaning both in terms of detector processing and detector access. It is clear that one-sided processing is much simpler and cheaper than double-sided one. Need to only access one side (front side in BNL case) for operation can also be simpler than that to access both sides, but in some cases, double-sided access may be desirable due to the fact that different type of voltages may be separated by the entire thickness of the detector. In the case of one-sided processing, the electrodes do not go all the way through the wafer, which makes the processing easier than the than standard 3D detectors – no support wafer and therefore wafer bonding are necessary. However a support wafer may be needed for the processing of an edgeless 3D detector (with edge sensitivity) to prevent detector chips from falling off in the deep reactive ion etcher.

1 The main advantages for dual-type column 3D Si detectors as compared to 2D planar
2 detectors are: 1) much smaller full depletion bias (depletion between the columns, which can be
3 made in the order of $<70 \mu\text{m}$, and is independent of detector thickness); 2) the drift distance is
4 also much reduced in this way, which results in a fast signal, and much improved radiation
5 hardness in terms of CCE if the column spacing is made in the same order of magnitude of that of
6 the trapping distance d_{tr} (or in a different term, charge collection distance d_{CCE} , at SLHC fluence,
7 d_{tr} can be in the order of 10^2 's of μm). These are in fact the main reasons that 3D Si detector is one
8 of the detector options for the SLHC. The main disadvantages for dual-type column 3D detectors
9 as compared to 2D planar ones are the field non-uniformity in the bulk (due to small electrodes in
10 3D detectors (10-20 μm diameter columns): the field is non-uniform in 2 dimensions (exclude the
11 surfaces in standard 3D or the surface and the end of columns region in non-penetrating column
12 3D detectors) as compared to 1 dimension in 2D planar detectors; low or zero field region (the
13 saddle point in the middle of the cell due to symmetry); and complexity in detector processing
14 and possible lower yield. We note here that the field non-uniformity is even more, in 3
15 dimensions, in single-type column 3D detectors.

16

17 **4. Weighting field simulation**

18

19 The induction of signals in the electrodes of detectors is generally based on the Shockley-
20 Ramo theorem [7-9]. The theorem states that the instantaneous current induced on a given
21 electrode is equal to the products of the charge of the carrier, its drift velocity (which is
22 proportional to the electric field as simulated before) and the weighting field E_0 [10]:

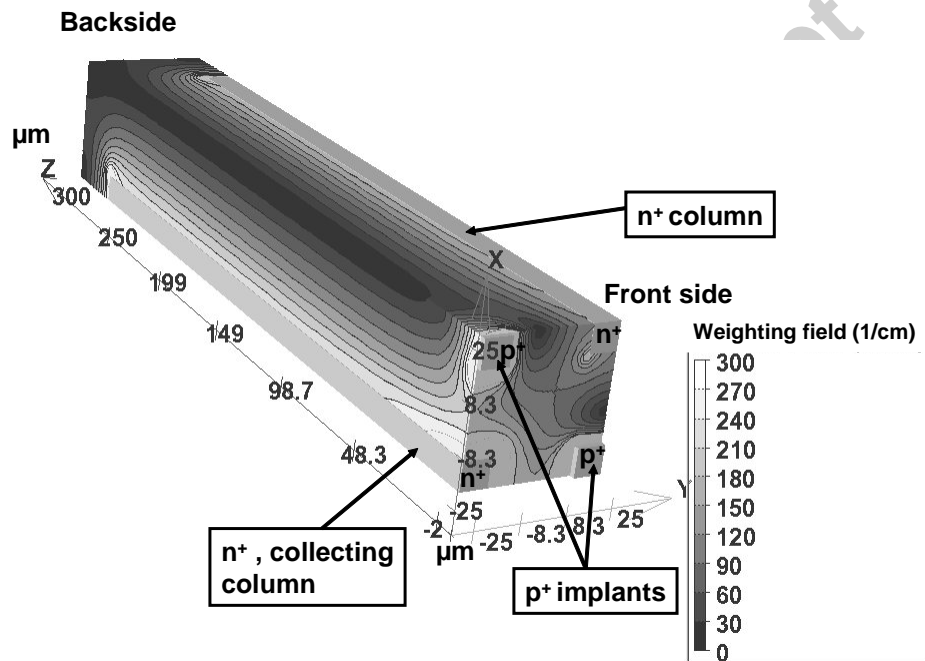
23

$$i = q\vec{v} \cdot \vec{E}_0 \quad (2)$$

2

3 The weighting field can be simulated. Shown in Fig. 9 is the simulated weighting field for BNL
 4 one-sided single-type column detector and in Figure 10 are the weighting fields for BNL one-
 5 sided dual-type column detector and the double-sided dual-type column detector by CNM.

6



7

8 Fig. 9. The weighting field of BNL one-sided single-type column detector.

9

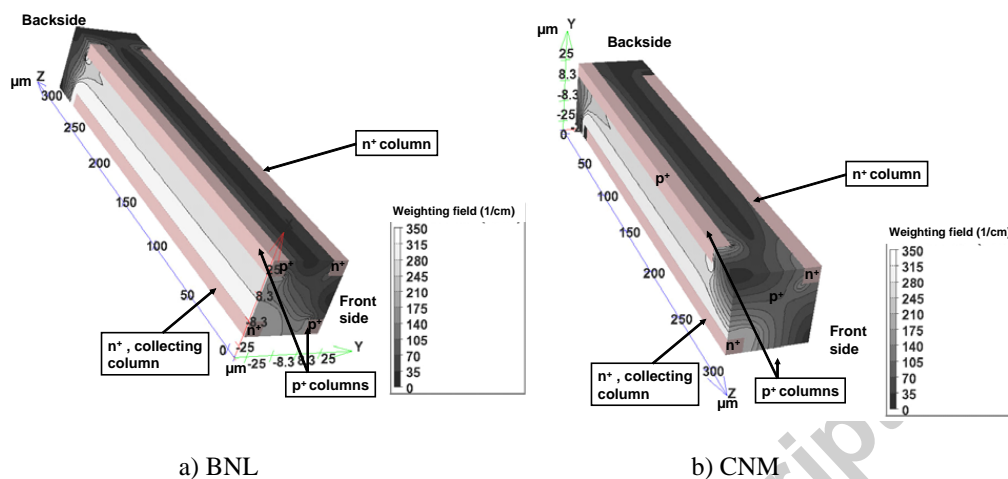


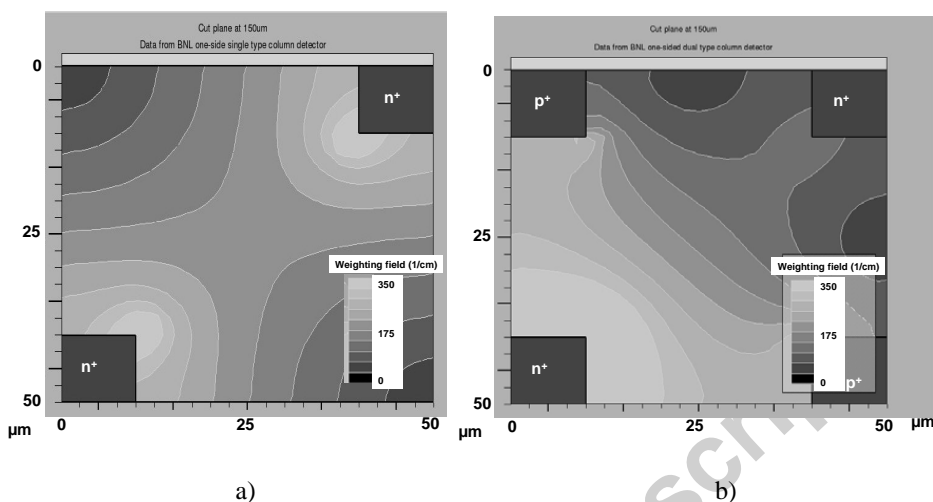
Fig. 10. The weighting fields of dual-type column detectors a) the BNL one-sided dual-type column detector and b) the double-sided dual-type column detector developed by CNM.

It is clear that the high weighting field region is mainly concentrated along the collecting column (n^+ column here on the low left corner), extending all across the cell in the simulation.

Details of the weighting field distribution can be seen more clearly from the 2D cut plane of the detector. In Figure 11 the BNL one-sided single and dual-type column detectors have been cut at $150\ \mu\text{m}$ in the middle of the detector thickness. As shown in Fig. 11 b) for a BNL one-sided dual-type column 3D Si detector, the high weighting field exists within $30\ \mu\text{m}$ from the collecting column, which is more than 60% of the cell length. Two low weighting field regions are present between the opposite n^+ column and the p^+ columns. This weighting field profile is similar for other types of dual-type column 3D Si detectors except near the surfaces.

As for the BNL one-sided single-type column 3D Si detector, the high weighting fields are concentrated near the two n^+ columns, extending $25\ \mu\text{m}$ away from the columns. Two low weighting field regions exist directly under the p^+ implants.

1



2

3

4 Fig. 11. Weighting field cuts at 150 μm for a) BNL one-sided single-type column detector and b)
 5 BNL one-sided dual-type column detector.

6

7 For future studies and simulation, we plan to integrate the electric field and weighting
 8 field simulations such that one can calculate the actual induced current for various 3D Si
 9 detectors under various radiation fluences.

10

11 5. Conclusion

12

13 BNL one-sided single and dual-type column 3D Si detectors have been simulated in detail
 14 and compared to various other 3D detector structures. Dual-type column detectors are best in the
 15 radiation-hard, but single-type column detectors are easier to process since only one type of
 16 columns needs to be etched. Disadvantage of these single-type column detectors is the non-
 17 uniform electric field. In BNL one-sided single-type column 3D detectors, some high field can be

1 developed along the junction column. The advantages and disadvantages for various detector
2 structures are concluded in Table 1.

3 In this paper we also reported on 3D simulations of weighting field profiles for different
4 3D detector structures. High weighting field has been found existing in more than half of the
5 volume in a cell, which should be a good advantage for 3D detectors.

6

7 **Acknowledgements**

8

9 This research was supported by the U.S. Department of Energy: Contract No. DE-AC02-
10 98CH10886.

11

12 **References**

13

- 14 [1] S.I. Parker et al., NIM A 395 (1997) 328-343.
15 [2] Z. Li et al., NIM A (2007), doi:10.1016/j.nima.2007.08.207.
16 [3] Atlas User's Manual – Device simulation software, Silvaco International.
17 [4] Sze S.M., Physics of semiconductor devices, 2nd edition, 1981, John Wiley & Sons, Inc.
18 [5] C. Piemonte et al., NIM A 541 (2005) 441-448.
19 [6] C. Fleta et al., NIM A 579 (2007) 642-647.
20 [7] W. Shockley, Jour. of Appl. Physics 9, 635, 1938.
21 [8] S. Ramo, Proc. of the I. R. E. 27, 584, 1939.
22 [9] G. Cavalleri et al., NIM 92 (1971) 137-140.

- 1 [10] G. F. Knoll, Radiation Detection and Measurement, 3rd edition, 2000, John Wiley & Sons,
2 Inc, p.790.
- 3 [11] C. Da Via et al., presented at the Sixth International "Hiroshima" Symposium on the
4 Development and Application of Semiconductor Tracking Detectors Carmel Mission Inn,
5 California, September 11-15, 2006
6

Accepted manuscript

1 **Table 1**

2 Summarizing comparison of the properties of different 3D detector structures.

3

Structure	E-field profile	Rad-hardness	Mechanical integrity	Processing	Sides needed to access for operation	Sensitivity under the column
Std 3d (UH)	Good	Super Possible high field regions on both surfaces	Good with supporting wafer	Wafer bonding needed	Front side	Some reported [11]
BNL dual-C	Good Added non-uniformity near the column tips	Super Possible high field regions on front surface and near the column tips	Good	True one-sided (backside not processed at all)	Front side	Some, the volume under the columns may be depleted
CNM dual-C	Good Added non-uniformity near the column tips	Super Possible high field regions on both surfaces and near the column tips	Good	Double-sided	Front side and backside	Some, the volume under the columns may be depleted
BNL single-C	Low field on the back side Higher degree of non-uniformity	Good Possible high field regions on front surface and near the column tips	Good	True one-sided (backside not processed at all)	Front side	Some, the volume under the columns may be depleted
Trento single-C	Low field on the front and center Higher degree of non-uniformity	Good Possible high field regions on front surface and near the column tips	Good	One-sided (backside uniform ion implant and metallization)	Front side and backside	Some, the volume under the columns may be depleted

4

5

1 **Figure captions**

2

3 Fig. 1. Sketch of a BNL 3D detector featuring columnar electrodes of one doping type, a)
4 detector unit cell and b) top view.

5

6 Fig. 2. Sketch of a BNL 3D detector featuring columnar electrodes of n- and p- doping type, a)
7 detector unit cell and b) top view.

8

9 Fig. 3. Simulated 3D electric field profile in a BNL single type of column 3D detector at 100 V
10 bias.

11

12 Fig. 4. A 2D cut plane of the simulated electric field in a BNL single type of column 3D detector
13 at 100 V bias.

14

15 Fig. 5. A 2D cut plane of the simulated electric field in a BNL single type of column 3D detector
16 at 200 V bias.

17

18 Fig. 6. Comparison of electric field profiles between two types of single column 3D detectors
19 operated at 100 V bias. The 2D cut plane is along the two n^+ columns.

20

21 Fig. 7. Electric field profiles of a BNL dual column 3D detector operated at 40 V bias: a) 3D
22 profile; b) 2D profile in a cut plane in the middle.

23

1 Fig. 8. Comparison of electric field profiles between three types of dual column 3D detectors
2 operated at 100 V bias. The 2D cut plane is along the two n^+ columns.

3

4 Fig. 9. The weighting field of BNL single column detector.

5

6 Fig. 10. The weighting fields of dual column detectors a) the BNL dual column detector and b)
7 the dual column detector developed by CNM.

8

9 Fig. 11. Weighting field cuts at 150 μm for a) BNL single column detector and b) BNL dual
10 column detector.

11

Publication VI

Z. Li, T. Grönlund

“3D Simulation Studies of Irradiated BNL One-Sided Dual-column 3D Silicon Detector up to $1E16$ n_{eq}/cm^2 ”

3D Simulation Studies of Irradiated BNL One-Sided Dual-column 3D Silicon Detector up to $1E16 \text{ neq/cm}^2$

Zheng Li¹ and Tanja Grönlund^{1,2}

¹Brookhaven National Laboratory

²Lappeenranta University of Technology

Abstract

Full 3D simulations have been carried out on the BNL one-sided 2-column 3D Si detector (p-type substrate) at various irradiation levels up to $1E16 \text{ neq/cm}^2$. The n+ and p+ columns are not etched all the way through the wafer, leaving about 10% volume under the columns. The backside of the wafer is completed un-processed with a layer of SiO_2 , and it is left floating during operation (true one-sided 3D detector). It has been shown that 1) simulated full depletion voltage V_{fd} for a dual-column 3D detector is about 1.4 time higher than that of a 2D (planar) pad detector with a thickness d the same as the column spacing L_p in the 3D detector; 2) the highest E-field is near the n+ column, and high E-field mainly distributes between the n+ and p+ columns; 3) low E-field is between the two p+ columns, and the lowest E-field is in the center of the unit cell with two p+ columns and two n+ columns; 4) in order to fully deplete a dual-column 3D detector at $1E16 \text{ neq/cm}^2$ with a reasonable bias ($\leq 200 \text{ V}$), the column spacing L_p should be reduced to $30 \mu\text{m}$; and 5) the volume under the columns (10% of the total volume) can be depleted with a modest bias ($\leq 200 \text{ V}$), and this volume under the columns are not dead volume. In addition, this depletion volume can provide some detection sensitivity directly under the columns, which may reduce the effective dead volume in a 3D Si detector.

PACS:

Keywords: silicon detectors, 3D detectors, device simulation, irradiation, electric field, column spacing

Corresponding author: tel.: , fax.: , email: zhengl@bnl.gov.

1. Introduction

To achieve some of the high energy physic experiments prime goals – for example the discovery and possible study of Higgs-particles – the silicon detectors has to operate in extreme harsh radiation environment. In the proposed upgrade of LHC (Super-LHC, SLHC), the increase of the maximal fluence and the beam luminosity up to 10^{16} neq/cm^2 and $10^{35} \text{ cm}^{-2}\text{s}^{-1}$ will require detectors with dramatic improvement in radiation hardness. Therefore, the main goals of detector development for the SLHC are concentrated on the technologies that minimize the radiation degradation. The interest for the 3D silicon detectors is continuously growing because of their many advantages against planar detectors: the devices can be fully depleted at low bias voltages, the speed of the charge collection is high, and the collection distances are about one order of magnitude less than those of planar technology strip and pixel detectors with electrodes limited to the detector surface. Also the 3D detectors exhibit high radiation tolerance, so the ability of the silicon detectors to operate after irradiation is increased.

The architecture for solid-state radiation detectors using a three-dimensional array of electrodes that penetrate into the detector bulk were proposed by S.I. Parker, C.J. Kenney and J. Segal in the mid 90's [1]. This standard design of 3D detectors present columnar electrodes of both doping types arranged in adjacent cell and penetrated through the silicon substrate. In this paper, we present 3D detector design with dual type of the columns on the p-type substrates. The n+ and p+ columns are not etched all the way through the wafer, leaving about 10% volume under the columns. The backside of the wafer is completed un-processed with a layer of SiO₂, and it is left floating during operation so the process is true one-sided. With full 3D simulations, we present the dual column 3D detector properties under the irradiation and we show how to improve 3D detectors to face future high-energy physics demand of the beam luminosity up to 10¹⁶ n_{eq}/cm². First, we compare the full depletion voltage between a planar 2D detector and a dual column 3D detector with a thickness *d* the same as the column spacing *L_p* in the 3D detector. As a result simulated full depletion voltage *V_{fd}* for a dual-column 3D detector is about 1.4 time higher than that of a planar pad detector. Second, the electric field in the structure is studied. The highest electric field (E-field) is near the n+ column, and high E-field mainly distributes between the n+ and p+ columns. The low E-field is between the two p+ columns, and the lowest E-field is in the center of the unit cell with two p+ columns and two n+ columns as shown in simulations. For future development, achieve a fully depletion in a dual-column 3D detector at 1E16 neq/cm² with a reasonable bias (≤ 200 V), the column spacing *L_p* should be reduced to 30 μm. Also, the volume under the columns (10% of the total volume) can be depleted with a modest bias (≤ 200 V), and this volume under the columns are not dead volume.

2. Full 3D simulations and device description

3D simulations were performed with ATLAS by Silvaco [2] and the DEVICE3D package of ATLAS was used to simulate 3D detectors. The numerical simulations were aimed to investigate the affect of the radiation introduced to the dual column 3D detector. A sketch of the BNL dual column detector is shown in Figure 1 [3-4]. In this structure there are two n-type and two p-type doped columns on p-type substrate. Same types of doped columns are placed to the opposite corners in the unit cell. All the columns are placed on the front side of the detector and they extend to 270 μm into the 300 μm deep p-type bulk. The ohmic contact is achieved by a uniform implant at the back surface of the wafer; the process is then single-sided.

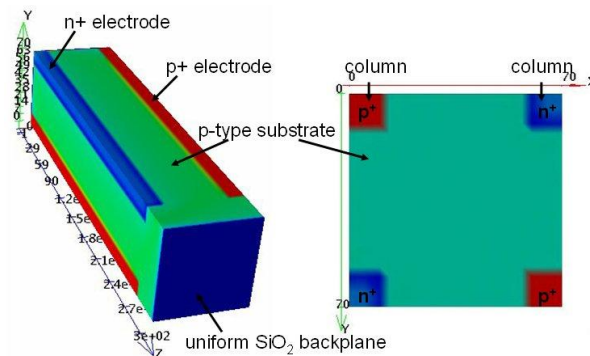


Fig. 1. Sketch of a BNL 3D detector featuring columnar electrodes of n- and p- doping type.

A lot of studies have been done in the past to generate an empirical model for the evolution of the effective doping concentration N_{eff} . Change in the depletion voltage with respect to the absolute effective doping concentration as measured immediately after irradiation is described in Ref. [5]. Detectors made to p-type substrate are not type inverted. Then, the depletion voltage increases because the effective doping concentration N_{eff} is increasing after irradiation. For not type inverted detectors N_{eff} is positive and becoming more positive and usually this behavior is attributed to an annealing of acceptors. That's why N_{eff} can be divided in components with one component N_A as a short term annealing component. Because only the longest decay time constant is relevant for the operation of silicon detectors in high-energy physics experiments, the fluence dependence of N_A can be represented by [6]:

$$N_A = g_a \phi_{eq} \quad (1)$$

And the average introduction rate g_a is given by $g_a = (1.81 \pm 0.14) \times 10^{-2} \text{ cm}^{-1}$ [6]. The doping concentration can be expressed as a function of fluence. In simulations the doping concentration varies and the affect of the radiation can be simulated.

3. Depletion voltage

Simulations for dual column 3D detectors were done with variety of fluences. The simulated full depletion voltage V_{fd} for a dual-column 3D detector show to be about 1.4 time higher than that of for calculated full depletion voltage of a 2D pad detector with a thickness d the same as the column spacing L_p in the 3D detector. The results are shown in Table 1.

Table 1. Full depletion voltage, calculated for a 2D detector and simulated for the 3D detector with a thickness d the same as the column spacing L_p in the 3D detector.

Fluence	<i>2d pad detector (d=50μm)</i>	<i>Dual columns 3D detectors (L_p=50μm)</i>
	Calculated V_{fd}	Simulated V_{fd}
5.00E+14	19	30
1.00E+15	38	60
2.00E+15	76	110
3.00E+15	114	160
4.00E+15	152	210
5.00E+15	190	250
6.00E+15	228	300
7.00E+15	266	350
8.00E+15	304	400
9.00E+15	342	450
1.00E+16	380	500

Comparing to thin planar detectors, 3D detectors need higher full depletion voltage. Usually the planar detectors used in high-energy physics experiments are 300 μm thick. In that case the 3D detectors full depletion voltage is lower (with 50 μm column spacing) and it is an advantage against planar detectors.

4. Electric field

Simulations show that the highest E-field is near the n+ column in Fig. 2.

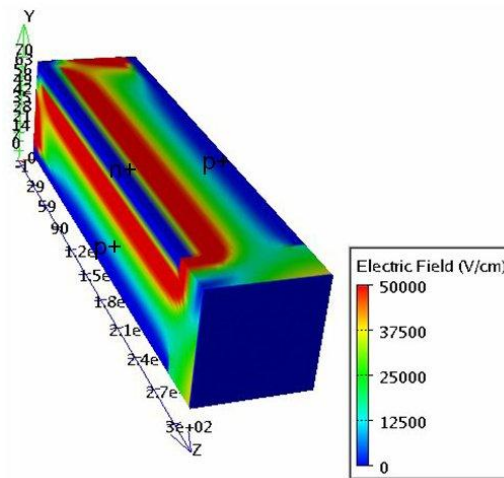


Fig.2. Electric field, $\phi_{eq} = 4 \times 10^{15} \text{ n}_{eq} / \text{cm}^2$, $V = 200 \text{ V}$.

High E-field mainly distributes between the n+ and p+ columns. The low E-field is between the two p+ columns (Fig. 3a), and the lowest E-field is in the center of the unit cell with two p+ columns and two n+ columns (Fig. 3b).

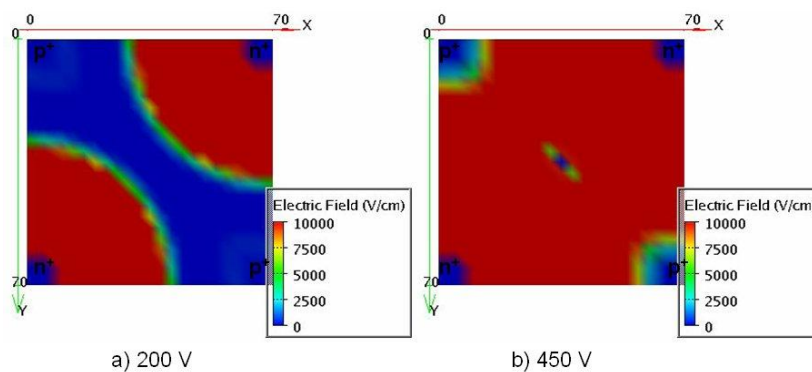


Fig. 3. Electric field. Fluence $\phi_{eq} = 9 \times 10^{15} \text{ n}_{eq} / \text{cm}^2$ and the applied voltage is a) $V = 200 \text{ V}$ and b) 450 V .

From Figure 3a can be seen that when detector is under the full depletion voltage (200 V), the low electric field area is between p-type electrodes. When reaching full depletion in Figure 3b almost the all detector space has high electric field, only in the middle of the structure is a spot of low electric field area.

5. Radiation and column spacing

In the future high-energy physics experiments require really high fluences up to $1E16 \text{ neq/cm}^2$. In order to fully deplete a dual-column 3D detector at $1E16 \text{ neq/cm}^2$ with a reasonable bias ($\leq 200 \text{ V}$), the column spacing L_p should be reduced to $30 \mu\text{m}$ (Fig. 4).

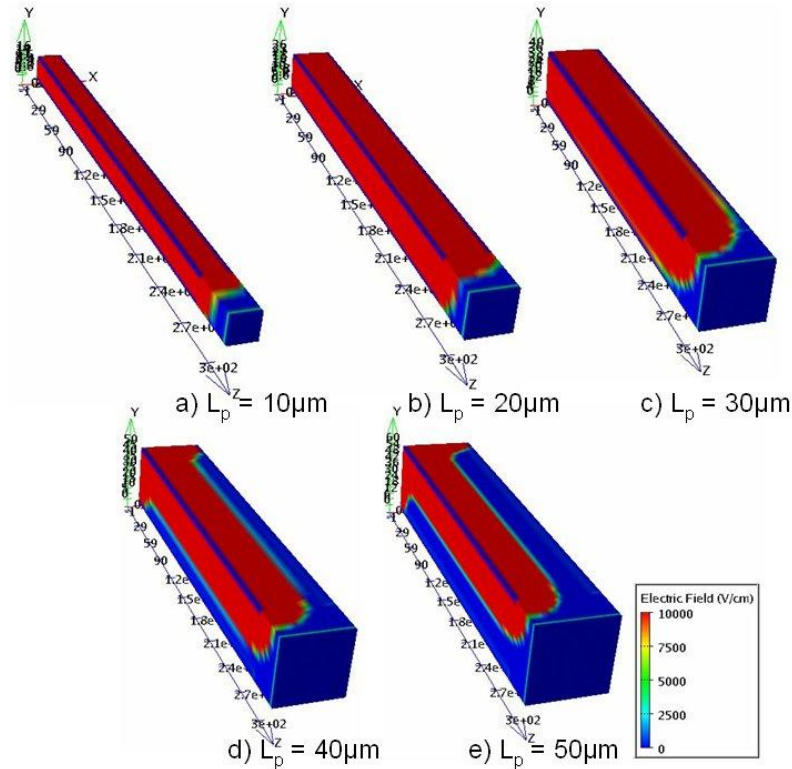


Fig. 4. Electric field, $\phi_{eq} = 1 \times 10^{16} \text{ neq} / \text{cm}^2$, $V = 200 \text{ V}$, L_p varies from $10 \mu\text{m}$ to $50 \mu\text{m}$.

The volume under the columns (10% of the total volume) can be depleted with a modest bias ($\leq 200 \text{ V}$), and this volume under the columns are not dead volume (Fig.5).

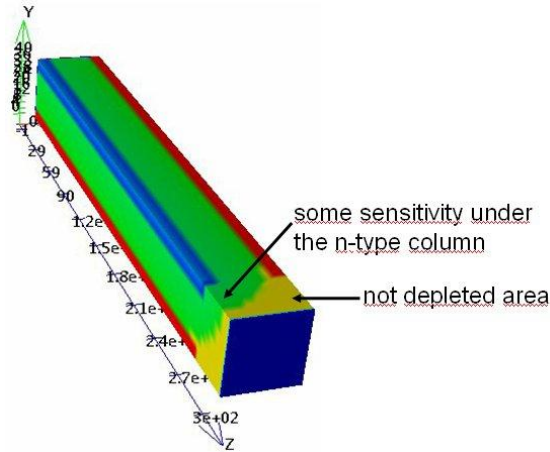


Fig. 5. The depletion in 3D detector with $L_p = 30 \mu\text{m}$ at 200 V and $\phi_{eq} = 1 \times 10^{16} \text{ n}_{eq} / \text{cm}^2$.

In the Figure 5 the depletion volume can provide some detection sensitivity directly under the columns, which may reduce the effective dead volume in 3D detectors.

6. Conclusion

In this paper we reported on TCAD simulations that have been performed to study the affect of the irradiation to the dual column 3D Si detectors. BNL dual column 3D detectors have been simulated in detail with variety of fluences. The simulated full depletion voltage V_{fd} for a dual-column 3D detector show to be about 1.4 time higher than that of for calculated full depletion voltage of a 2D pad detector with a thickness d the same as the column spacing L_p in the 3D detector. Simulations show that in this kind of detector structure the high electric field is near n-type electrode and the low electric field area is between the p-type electrodes. After reaching the full depletion there is still a low electric field spot in the middle of the structure. The future high-energy physics experiments demand the ability to face really high fluences up to $1\text{E}16 \text{ n}_{eq}/\text{cm}^2$. In order to fully deplete a dual-column 3D detector at $1\text{E}16 \text{ n}_{eq}/\text{cm}^2$ with a reasonable bias, the column spacing should be reduced.

Acknowledgements

This research was supported by the U.S. Department of Energy: Contract No. DE-AC02-98CH10886.

References

- [1] S.I. Parker et al., NIM A 395 (1997) 328-343.
- [2] Atlas User's Manual – Device simulation software, Silvaco International.
- [3] Z. Li et al., NIM A 583 (2007) 139-148.

- [4] T. Grönlund, Z. Li, G. Carini, M. Li, *Full 3D simulations of BNL one-sided silicon 3D detectors and comparisons with other types of 3D detectors*, accepted for publication: Nuclear Instruments and Methods in Physics Research A (2007).
- [5] R. Wunstorf, "*Systematische Untersuchungen zur Strahlenresistenz von Silizium-Detektoren für die Verwendung in Hochenergiephysik-Experimenten*", Ph.D. Thesis, University of Hamburg, Germany, 1992.
- [6] M. Moll, "*Radiation Damage in Silicon Particle Detectors*", Ph. D. Thesis, University of Hamburg, Germany, 1999.

ACTA UNIVERSITATIS LAPPEENRANTAENSIS

254. VEHVILÄINEN, JUHA. Procurement in project implementation. 2006. Diss.
255. MIROLA, TUULI. Impacts of the European integration and the European Union membership on Finnish export industries – Perceptions of export business managers. 2006. Diss.
256. RAUMA, KIMMO. FPGA-based control design for power electronic applications. 2006. Diss.
257. HIRVONEN, MARKUS. On the analysis and control of a linear synchronous servomotor with a flexible load. 2006. Diss.
258. LIU, JUNHONG. On the differential evolution algorithm and its application to training radial basis function networks. 2006. Diss.
259. LAITINEN, RISTO. Development of LC-MS and extraction methods for the analyses of AKD, ASA, and rosin sizes in paper products. 2006. Diss.
260. KUISMA, PETRI. Seinärakenteen infrapunakontrastin pienentäminen käyttäen ilmajäähdytystä ja säteily suojausta. 2007. Diss.
261. ELLONEN, HANNA-KAISA. Exploring the strategic impact of technological change – studies on the role of Internet in magazine publishing. 2007. Diss.
262. SOININEN, AURA. Patents in the information and communications technology sector – development trends, problem areas and pressures for change. 2007. Diss.
263. MATTILA, MERITA. Value processing in organizations – individual perceptions in three case companies. 2007. Diss.
264. VARTIAINEN, JARKKO. Measuring irregularities and surface defects from printed patterns. 2007. Diss.
265. VIRKKI-HATAKKA, TERHI. Novel tools for changing chemical engineering practice. 2007. Diss.
266. SEKKI, ANTTI. Successful new venturing process implemented by the founding entrepreneur: A case of Finnish sawmill industry. 2007. Diss.
267. TURKAMA, PETRA. Maximizing benefits in information technology outsourcing. 2007. Diss.
268. BUTYLINA, SVETLANA. Effect of physico-chemical conditions and operating parameters on flux and retention of different components in ultrafiltration and nanofiltration fractionation of sweet whey. 2007. Diss.
269. YOUSEFI, HASSAN. On modelling, system identification and control of servo-systems with a flexible load. 2007. Diss.
270. QU, HAIYAN. Towards desired crystalline product properties: In-situ monitoring of batch crystallization. 2007. Diss.
271. JUSSILA, IIRO. Omistajuus asiakasomisteisissa osuuskunnissa. 2007. Diss.
272. 5th Workshop on Applications of Wireless Communications. Edited by Jouni Ikonen, Matti Juutilainen and Jari Porras. 2007.
273. 11th NOLAMP Conference in Laser Processing of Materials Lappeenranta, August 20-22, 2007. Ed. by Veli Kujanpää and Antti Salminen. 2007.
274. 3rd JOIN Conference Lappeenranta, August 21-24, 2007. International Conference on Total Welding Management in Industrial Applications. Ed. by Jukka Martikainen. 2007.

275. SOUKKA, RISTO. Applying the principles of life cycle assessment and costing in process modeling to examine profit-making capability. 2007. Diss.
276. TAIPALE, OSSSI. Observations on software testing practice. 2007. Diss.
277. SAKSA, JUHA-MATTI. Organisaatiokenttä vai paikallisyhteisö: OP-ryhmän strategiat institutionaalisten ja kilpailullisten paineiden ristitulessa. 2007. Diss.
278. NEDEOGLO, NATALIA. Investigation of interaction between native and impurity defects in ZnSe. 2007. Diss.
279. KÄRKKÄINEN, ANTTI. Dynamic simulations of rotors during drop on retainer bearings. 2007. Diss.
280. KARPOVA, TATJANA. Aqueous photocatalytic oxidation of steroid estrogens. 2007. Diss.
281. SHIPILOVA, OLGA. Particle transport method for convection-diffusion-reaction problems. 2007. Diss.
282. ILONEN, JARMO. Supervised local image feature detection. 2007. Diss.
283. BOTAR-JID, CLAUDIU CRISTIAN. Selective catalytic reduction of nitrogen oxides with ammonia in forced unsteady state reactors. Case based and mathematical model simulation reasoning. 2007. Diss.
284. KINNUNEN, JANNE. Direct-on-line axial flux permanent magnet synchronous generator static and dynamic performance. 2007. Diss.
285. VALTONEN, MIKKO. Performance characteristics of an axial-flux solid-rotor-core induction motor. 2007. Diss.
286. PUNNONEN, PEKKA. Impingement jet cooling of end windings in a high-speed electric machine. 2007. Diss.
287. KÄRRI, TIMO. Timing of capacity change: Models for capital intensive industry. 2007. Diss.
288. TUPPURA, ANNI. Market entry order and competitive advantage of the firm. 2007. Diss.
289. TARKIAINEN, ANSSI. Field sales management control: Towards a multi-level theory. 2007. Diss.
290. HUANG, JUN. Analysis of industrial granular flow applications by using advanced collision models. 2007. Diss.
291. SJÖMAN, ELINA. Purification and fractionation by nanofiltration in dairy and sugar and sweetener industry applications. 2007. Diss.
292. AHO, TUOMO. Electromagnetic design of a solid steel rotor motor for demanding operation environments. 2007. Diss.
293. PURHONEN, HEIKKI. Experimental thermal hydraulic studies on the enhancement of safety of LWRs. 2007. Diss.
294. KENGPOL, ATHAKORN. An evaluation of ICTs investment using decision support systems: Case applications from distributor's and end user's perspective group decision. 2007. Diss.
295. LASHKUL, ALEXANDER. Quantum transport phenomena and shallow impurity states in CdSb. 2007. Diss.
296. JASTRZEBSKI, RAFAL. Design and implementation of FPGA-based LQ control of active magnetic bearings. 2007. Diss.

